

# **Numerical Simulation of microstructure of the GeSi alloy**

Von der Fakultät für Mathematik, Naturwissenschaften  
und Informatik  
der Brandenburgischen Technischen Universität  
Cottbus

zur Erlangung des akademischen Grades  
Doktor der Naturwissenschaften  
(Dr. rer. nat.)

genehmigte Dissertation

vorgelegt von

Diplom-Physiker

**Igor Rasin**

geboren am 29.05.1981 in Dniepropetrovsk, Ukraine

Gutachter: Prof. Dr. rer. nat. habil. Michael Bestehorn

Gutachter: Dr.-Ing. Sauro Succi

Gutachter: Dr. rer. nat. Wolfram Miller

Tag der mündlichen Prüfung: 8.09.2006



## **Abstract**

The goal of this work is to investigate pattern formation processes on the solid-liquid interface during the crystal growth of GeSi. GeSi crystals with cellular structure have great potential for applications in  $\gamma$ -ray and neutron optics. The interface patterns induce small quasi-periodic distortions of the microstructure called mosaicity. Existence and properties of this mosaicity are important for the application of the crystals. The properties depend on many factors; this dependence, is currently not known even not qualitatively. A better understanding of the physics near the crystal surface is therefore required, in order to optimise the growth process.

There are three main physical processes in this system: phase-transition, diffusion and melt flow. Every process is described by its own set of equations. Finite difference methods and lattice kinetic methods are taken for solving these governing equations. We have developed a modification of the kinetic methods for the advection-diffusion and extended this method for simulations of non-linear reaction diffusion equations.

The phase-field method was chosen as a tool for describing the phase-transition. There are numerous works applied for different metallic alloys. An attempt to apply the method directly to simulation GeSi crystal growth showed that this method is unstable. This instability has not been observed in previous works due to the much smaller scale of simulations. We introduced a modified phase-field scheme, which enables to simulate pattern formation with the scale observed in experiment. A flow in the melt was taken in to account in the numerical model.

The developed numerical model allows us to investigate pattern

formation in GeSi crystals. Modelling shows that the flow near the crystal surface has impact on the patterns. The obtained patterns reproduce qualitatively and in some cases quantitatively the experimental results.

## **Zusammenfassung:**

Das Ziel dieser Arbeit besteht darin, Mikrostrukturen, die während des Wachstumsprozesses von GeSi-Einkristallen entstehen zu erforschen. GeSi-Kristalle mit zellulärer Struktur haben ein hohes Potential für die Anwendung in der Gamma- und in der Neutronen-Optik. Die sich an der Phasengrenze ausbildende zelluläre Struktur verursacht entsprechende quasi-periodische Abweichungen in der Kristallstruktur, die Mosaizität genannt werden. Die Existenz und die Eigenschaften dieser Mosaizität sind entscheidend für die Anwendung der Kristalle. Die Eigenschaften hängen von vielen Faktoren ab. Gegenwärtig sind diese Abhängigkeiten sogar qualitativ noch nicht bekannt. Deswegen ist es notwendig, ein besseres Verständnis für die Vorgänge an der Phasengrenze zu erhalten.

Dabei sind im wesentlichen drei physikalische Prozesse wichtig: Phasenübergang, Diffusion und Schmelzkonvektion. Jeder Prozess wird durch entsprechende Gleichungen beschrieben. Für die Lösung der Gleichungen wurden Finite-Differenzen-Methoden und die kinetische Methoden angewandt. Wir haben eine Erweiterung der kinetischen Methode für die Advektions-Diffusionsgleichungen und die nichtlinearen Reaktions-Diffusions Gleichungen entwickelt.

Die Phasenfeld-Methode wurde als ein Werkzeug für die Beschreibung des Phasenübergangs gewählt. Es gibt eine Vielzahl von Arbeiten, die diese Methode auf die Erstarrung unterschiedlicher metallischer Legierungen anwenden. Bei der Anwendung der Ansätze dieser Arbeiten auf die Kristallisation der GeSi-Kristalle traten modellbedingte Instabilitäten auf. Diese Stabilitätsprobleme wurden bei anderen Arbeiten nicht beobachtet, da die zu berech-

nenden Strukturen wesentlich kleiner waren. Zur Lösung des Problems entwickelten wir eine modifizierte Phasenfeldgleichung, anhand welcher es möglich ist, die Simulation von entsprechend großen Zellularstrukturen durchzuführen, wie sie im Experiment beobachtet worden sind.

Der Algorithmus zur Lösung der Phasenfeldgleichung wurde mit dem kinetischen Schema zur Lösung der Diffusions-Advektions-Gleichung und dem Algorithmus zur Strömungsberechnung gekoppelt. Das entwickelte Numerische Modell erlaubt uns, die strukturbildenden Prozesse in GeSi-Kristallen zu untersuchen. Die Modellierung zeigte, dass Strömungen in der Nähe der Phasengrenze einen Einfluss auf die Zellularstrukturen ausüben. Die simulierte Struktur reproduziert qualitativ und in manchen Fällen sogar quantitativ die experimentellen Ergebnisse.

For my family

## **Acknowledgments**

First of all I would like to express my gratitude to my supervisor Dr. Wolfram Miller for his patience and help with the first steps of my research as well as for the useful discussions which we had.

I am also grateful to my colleagues Uwe Rehse and Dr. Klaus Böttscher who greatly assisted me during my work at the institute and showed tremendous patience while I was trying to adapt to German society and learn the German language. Many thanks to Dr. Nikolai Abrosimov, the experimentalist, who explained to me in detail the process and problems of growing GeSi crystals. I learned from him how to organize the communication between a theoretician and an experimentalist.

I would like to mention my Berlin friends whose help and support I enjoyed during my stay in Berlin. A very special thanks goes to Marina Litvinskaya, Lena Eyngorn and Sofia Gordon. Their influence and support were a source of great energy for me.

Last but not least, I would like to thank Uliya Kyrychko, Konstantin Blyus, Nadya Kositsina, Andrey Pototsky, Lev Solovev and Lena Zvonenko.



# Contents

<b>1</b>	<b>Introduction</b>	<b>1</b>
1.1	Modelling of solidification micro-structures . . . . .	1
1.1.1	GeSi crystals . . . . .	4
1.2	Modeled system . . . . .	7
1.3	Numerical methods . . . . .	8
1.4	Thesis structure . . . . .	8
<b>2</b>	<b>Lattice kinetic methods</b>	<b>11</b>
2.1	The lattice-Boltzmann and the LBGK methods . . . . .	12
2.1.1	Collision term for incompressible flow . . . . .	13
2.2	LK methods for passive scalar transport . . . . .	14
2.2.1	Single-relaxation LK (SRLK) model . . . . .	16
2.2.2	Multi-relaxation LK (MRLK) model . . . . .	18
2.2.3	Adaptive time step . . . . .	23
2.2.4	Numerical tests . . . . .	25
<b>3</b>	<b>Phase-field models</b>	<b>33</b>
3.1	The classic phase-field model . . . . .	34
3.2	The modified phase-field model . . . . .	38
3.3	Numerical implementation . . . . .	40
3.3.1	Numerical tests . . . . .	42

3.3.2	Equilibrium shape . . . . .	46
<b>4</b>	<b>Phase-field models for binary alloys</b>	<b>48</b>
4.1	Thermodynamics and the sharp interface model . . .	49
4.1.1	Thermodynamics . . . . .	49
4.1.2	Sharp interface model . . . . .	53
4.1.3	1D solutions . . . . .	54
4.2	Phase-field models for binary alloys . . . . .	55
4.2.1	Basic ideas . . . . .	55
4.2.2	The WBM phase-field model . . . . .	56
4.2.3	Evolution equations . . . . .	58
4.2.4	Limitation of the WBM model . . . . .	59
4.3	The KKS phase-field model . . . . .	61
4.3.1	Non-isothermal case . . . . .	63
4.4	Numerical scheme . . . . .	65
4.4.1	Finite difference approach for the concentra- tion equation . . . . .	66
4.4.2	MRLK discretization of the concentration equa- tion . . . . .	68
4.5	Pattern formation for NiCu alloys . . . . .	69
4.5.1	1D simulations . . . . .	71
4.5.2	2D simulation . . . . .	74
4.5.3	Role of anisotropy . . . . .	77
4.5.4	Influence of shear flow . . . . .	78
<b>5</b>	<b>Cellular growth in GeSi crystals</b>	<b>81</b>
5.1	The Czochralski growth . . . . .	83
5.2	Analytical estimations . . . . .	86
5.3	1D simulations . . . . .	87
5.4	Simulation without flow . . . . .	90

5.5	Influence of flow . . . . .	96
5.5.1	Stability of cellular structure . . . . .	97
5.5.2	Growth orientation of cells . . . . .	98
<b>6</b>	<b>Conclusion</b>	<b>104</b>
<b>A</b>	<b>Thermodynamically consistent PF model</b>	<b>108</b>
A.1	Common equations . . . . .	108
A.2	Governing equations . . . . .	110
<b>B</b>	<b>Solution of the diffusion equation for special problem</b>	<b>113</b>
<b>C</b>	<b>Local curvature</b>	<b>114</b>
<b>D</b>	<b>Finite difference schemes</b>	<b>117</b>
D.1	Properties of the lattice vectors . . . . .	117
D.1.1	The 2D case . . . . .	117
D.1.2	The 3D case . . . . .	118
D.2	Differential operators . . . . .	119
D.2.1	The 2D case . . . . .	119
D.2.2	The 3D case . . . . .	120

# Notations

$\vec{a}_i$	Lattice vectors	
$a_s$	Speed of sound in LK methods	
$a_1, a_2$	Proportional coefficients in relation between phase-field and physical parameters	
$c$	Concentration of the component $A$	
$\tilde{c}$	Concentration of the component $B$ , $(1 - c)$	
$c_p$	Heat capacity per volume	$\left[ \frac{\text{J}}{\text{m}^3 \cdot \text{K}} \right]$
$c_{pA}, c_{pB}$	Heat capacity for components $A$ and $B$ , respectively	$\left[ \frac{\text{J}}{\text{m}^3 \cdot \text{K}} \right]$
$c_{pl}, c_{ps}$	Heat capacity for liquid and solid phases	$\left[ \frac{\text{J}}{\text{m}^3 \cdot \text{K}} \right]$
$c_l, c_s$	Concentration in liquid and solid	
$c_l^0, c_s^0$	Liquidus and solidus concentrations	
$c_{l0}$	Boundary value of the concentration on the liquid end of the domain	
$c_{s0}$	Expected concentration in the solid phase	
$d_0$	Capillary length	$[\text{m}]$
$e$	Internal energy density	$\left[ \frac{\text{J}}{\text{m}^3} \right]$
$f$	Free energy density	$\left[ \frac{\text{J}}{\text{m}^3} \right]$
$f_i$	Number of quasi-particles moving in $i^{\text{th}}$ direction, discrete distribution function	

$f_i^{eq}$	Equilibrium distribution function	
$g(\phi)$	Double-well potential	
$h(\phi)$	A function in the phase-field equation	
$\hat{k}_A, \hat{k}_B$	Partition coefficients for substances A and B	
$k_\infty$	Effective distributional coefficient	
$m_e$	Slope of the liquidus	
$n$	Density	
$\vec{n}$	Normal vector to the interface	
$p(\phi)$	Function in the phase-field equation	
$\vec{r}$	Radius vector	
$s$	Entropy density	$\left[ \frac{J}{m^3 K} \right]$
$u_t$	Velocity of tangential flow near the crystal surface	$\frac{m}{s}$
$\vec{v}$	Flow velocity	$\left[ \frac{m}{s} \right]$
$v_{pull}$	Pooling velocity	$\left[ \frac{m}{s} \right]$
$v_{gr}$	Growth velocity	$\left[ \frac{m}{s} \right]$
$w_i$	Weight coefficients	
$w_\phi$	Width of transition region	
$Ca$	Capillary number	
$D$	Diffusion coefficient	$\left[ \frac{m^2}{s} \right]$
$D_{\alpha\beta}$	Diffusion tensor	$\left[ \frac{m^2}{s} \right]$
$D_T$	Thermal diffusivity	$\left[ \frac{m^2}{s} \right]$
$D^*$	Rescaled value of the diffusion coefficient, $D^* = D \frac{\delta_t}{\delta_x^2}$	

$\mathcal{E}$	Internal energy function	[J]
$\mathcal{F}$	Free energy function	[J]
$G_T$	Temperature gradient	$\left[\frac{\text{K}}{\text{m}}\right]$
$I_I$	Solvability integral	
$J_I$	Solvability integral	
$\vec{J}$	Flux	
$\mathbf{J}$	Flux of quasi-particles	
$K_I$	Solvability integral	
$K_l, K_s$	Heat conductivities of liquid and solid phases	$\left[\frac{\text{W}}{\text{m}\cdot\text{K}}\right]$
$L$	Latent heat per volume	$\left[\frac{\text{J}}{\text{m}^3}\right]$
$L^M$	Latent heat per mol, $L^M = LV_M$	$\left[\frac{\text{J}}{\text{mol}}\right]$
$\mathbf{M}_{\alpha\beta\gamma}$	Third order kinetic moment in LK scheme	
$N_a$	The Avogadro constant	$6 \cdot 10^{23} \frac{1}{\text{mol}}$
$\mathbf{P}_{\alpha\beta}$	Second order kinetic moment in LK scheme	
$P_3$	Projector associated with the third eigenvector	
$P$	Pressure	[Pa]
$R$	Gas constant	$8.31 \frac{\text{J}}{\text{mol}\cdot\text{K}}$
$S$	Entropy function	$\left[\frac{\text{J}}{\text{K}}\right]$
$\hat{S}$	Collision operator in LK methods	
$Sc$	Schmidt number	
$St$	Stefan number, dimensionless undercooling	
$T$	Absolute temperature	[K]
$T_{\Delta 0}$	Temperature difference between solidus and liquidus values for a constant $c$	[K]
$T_m$	Melting-point temperature	[K]
$T'$	Temperature difference, $T' \equiv T - T_m$	[K]

$T_A, T_B$	Melting-point temperature for components $A$ and $B$ , respectively	[K]
$T'_A, T'_B$	Temperature difference, $T'_{A,B} \equiv T - T_{A,B}$	[K]
$V_m$	Molar volume	$\left[\frac{\text{m}^3}{\text{mol}}\right]$
$V_i^{(k)}$	Eigenvectors of the relaxation matrix	
$W$	The phase-field parameter “thermodynamically-consistent” notations	in $\left[\frac{\text{J}}{\text{m}^3\text{K}}\right]$
$\alpha_{dt}$	Time step increase coefficient	
$\beta$	Inverse kinetic coefficient	
$\delta_{\alpha\beta}$	Kronekers delta symbol, $\begin{cases} 1, & \alpha = \beta \\ 0, & \alpha \neq \beta \end{cases}$	
$\delta_x$	Space step in a numerical method	
$\delta_t$	Time step in a numerical method	
$\delta_c$	Width of diffusion layer near a solid surface for concentration field	[m]
$\delta_m$	Width of diffusion layer near a solid surface for flow field	[m]
$\gamma$	Surface energy	$\left[\frac{\text{J}}{\text{m}^2}\right]$
$\gamma\xi$	$\frac{\xi_{\perp}}{\xi_{\parallel}}$	
$\kappa$	Local curvature of the interface	$\left[\frac{1}{\text{m}}\right]$
$\lambda$	The phase-field parameter	$[\text{K}^{-1}]$
$\lambda_1$	Eigenvalue of the collision matrix	
$\mu$	Kinetic coefficient	
$\nu$	Kinematic viscosity	$\left[\frac{\text{m}^2}{\text{s}}\right]$
$\nu^*$	Rescaled value of the diffusion coefficient, $\nu^* = \nu \frac{\delta_t}{\delta_x^2}$	

$\omega_{ij}$	Relaxation parameter in the LBGK scheme	
$\omega_J$	Eigenvalue of the relaxation matrix in the MRLK scheme	
$\phi$	The phase-field, order parameter	
$\rho$	Local density of quasi particles $\rho \equiv \sum_i w_i f_i$	
$\sigma$	Surface energy	$\left[ \frac{\text{J}}{\text{m}^2} \right]$
$\tau$	The phase-field parameter	$[\text{s}]$
$\tau_T$	The phase-field parameter in “thermodynamically-consistent” notations	$\left[ \frac{\text{Js}}{\text{m}^3\text{K}} \right]$
$\xi$	The phase-field parameter	$[\text{m}]$
$\xi_S$	The phase-field parameter in “thermodynamically-consistent” notations	$\left[ \sqrt{\frac{\text{J}}{\text{mK}}} \right]$
$\xi_{\perp}$	The parameter of the modified phase-field model	$[\text{m}]$
$\xi_{\parallel}$	The parameter of the modified phase-field model	$[\text{m}]$
$\Lambda_{\alpha\beta}$	Projection of the relaxation matrix on the flux space	
$\Omega$	Relaxation matrix	
$\Theta$	Constitutional undercooling	$\left[ \frac{\text{J}}{\text{m}^3\text{K}} \right]$
$\Upsilon$	Interface boundary	





# Chapter 1

## Introduction

### 1.1 Modelling of solidification micro-structures

Modeling of solidification micro-structures has become an area of intense study in recent years. The properties of large-scale cast products, ranging from automobile engine blocks to aircraft components and other industrial applications, are strongly dependent upon the physics that occurs at the mesoscopic and microscopic length scales during solidification. The main types of solidification micro-structure are dendrites and cells. The dendrite is a snowflake-like pattern of a solid phase, see Fig.(1.1). Cells are regular perturbations of the solid liquid interface, see Fig.(1.2). The microscopic properties of such cast products are determined by the length scales of these patterns. For this reason, understanding of the mechanisms for pattern selection during growth has attracted a great deal of interest from experimental and theoretical communities.

The solidification patterns are usually considered in conjunction with applications of metals. Many articles, therefore, study metals and metallic alloys [37, 34, 42, 32] or deal with model materials such as: SCN, Xe and others [40]. (These materials have properties similar to metals, such as anisotropy). Another application field is “snow research”[27, 72]. Pattern formation during crystal growth of semiconductors is not the usual subject of numerical study<sup>1</sup>, although numerous experimental and theoretical works have been written on the subject [23].

Works in the field of solidification pattern formation can be divided into two groups. The first contains those works which are oriented on model development [19, 20]. This group makes qualitative comparisons of the simulation results with the experimentally observed effects. The second group, in contrast to the first, contains those works which make quantitative comparisons between theory and experiment [26, 17, 46]. The question of comparison with experiments is highly problematic. For instance, in experimental works dealing with Xe crystals, [6] the crucial parameter in comparisons between simulations and experiments is undercooling,  $St$ . The experiment operates with  $St \sim 0.01$ , but this undercooling is hard to achieve in simulations [45]. Similar problems arose during the work on this thesis.

Formation of patterns during growth of semiconductor crystals has been discussed by many authors. Numerous experimental investigations have been collected by Hurlé [23]. The microstructure which appears is considered an undesirable phenomena leading to crystal defects or even destruction of the crystal. In publications,

---

<sup>1</sup>As far as we know currently there are no such works from other groups in this field.

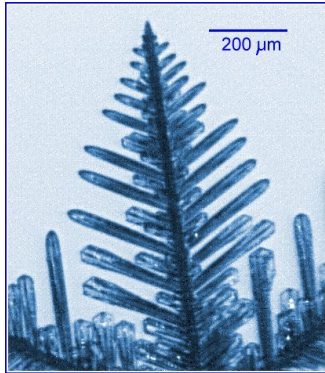


**Figure 1.1:** Photo of a snow crystal. A dendrite with side branches is seen on the photo.

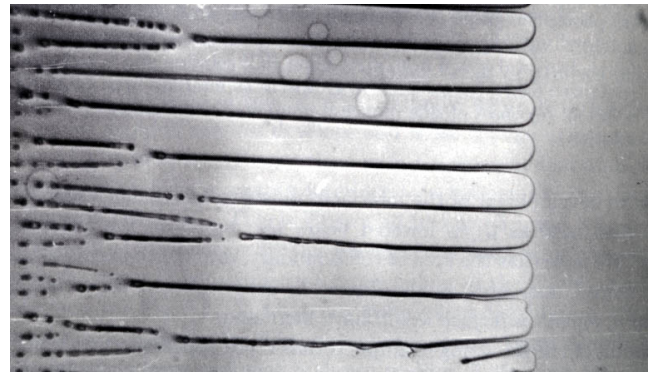


**Figure 1.2:** Cellular interface in a transparent organic  $72 \times \text{Mag}$  (Succinonitrile-5.5 wt% acetone -courtesy of Triverdi [5]).

more attention is generally paid to the study of conditions which lead to such effects, and to the discussion of how to avoid them, than to the study of the crystals properties. Peculiarities of the patterns are not the usual focus of investigation for this community.

The GeSi alloy is a semiconductor material where a cellular structure is desirable in some applications. The patterns, which appear on its interface, induce a mosaic structure of the crystal. Such crystals are used in  $\gamma$ -ray and neutron optics.

In this work, in particular, a great deal of research has been undertaken to understand such issues as morphology, size and cell-stability in Ge-rich GeSi crystals. The simulation of the phase transition process was accomplished by a melt flow. The developed model was verified by simulations of directional solidification in the NiCu alloy.

### 1.1.1 GeSi crystals

Bulk crystals of  $\text{Ge}_{1-x}\text{Si}_x$  solid solutions constitute a promising material for  $\gamma$ -ray and neutron optics. Crystals, grown in IKZ, for example, were used for the development of the first  $\gamma$ -ray lens telescope CLAIRE [65]. One of the main parts of the CLAIRE telescope was the  $\gamma$ -ray lens, consisting of 556 elements. Each element has the form of a quadratic plate with a size of  $10 \times 10 \times 1$  mm. These elements were cut from  $\text{Ge}_{1-x}\text{Si}_x$  crystals grown using the modified Czochralski technique [2]. The used GeSi crystals are "ideally imperfect crystals". Every crystal has a mosaic structure (mosaicity); i.e. the crystal structure has a small periodic distortion and the local lattice orientation has a spatial dependence. For the crystal lens telescope, the optimal mosaicity (distortion of the grid) of diffracting elements was calculated using Darwin's model for mosaic crystals. The obtained mosaicity is about  $30''$  [65, 51]. In the Darwin model, the defective structure of the crystal, which maybe due to dislocations, inhomogeneous strain, etc., is described by an agglomerate of perfect crystal blocks that are slightly angle-shifted against each other. The size of the blocks, taking part in the scattering process, should be mesoscopic or microscopic to reach a higher diffraction efficiency.

The mosaicity of the GeSi crystals was achieved by intentionally disturbing the solid-liquid interface. The relation between the cellular morphology of the interface and the mosaicity is currently not clear. The distortion of the interface directly causes two effects: inhomogeneity of the Si fraction in the crystal and an increase in the dislocation density. It is not known which of these two factors corresponds to the mosaic structure.

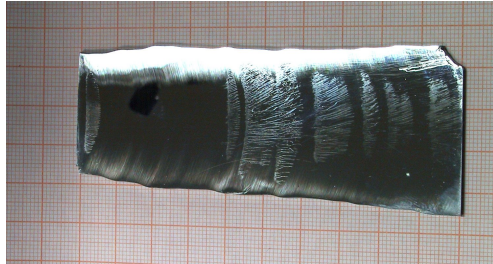


**Figure 1.3:** Cross-section of the GeSi crystal along the rotation axis.

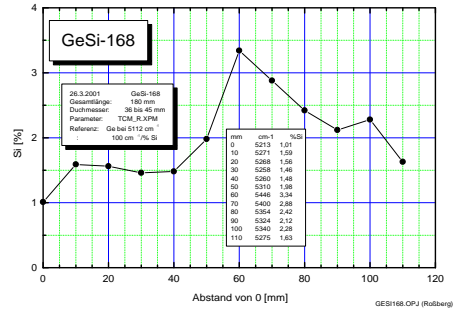


**Figure 1.4:** Concentration profile for the GeSi crystal (Fig. 1.3)

Cellular patterns on the interface appear because of constitutional supercooling near the solid-liquid interface, see D.T.J Hurle [23]; the theoretical background of this instability is summarized by Langer [36].

Initial experiments showed that the GeSi crystals without cellular structure provide a mosaicity of less than  $12''$  (low range detection limit of the hard X-ray diffractometer). Only growth of GeSi crystals with a cellular structure makes possible the achievement of mosaicity in the range from  $30''$  to  $60''$ , which is required for this application. The density of the grown-in dislocations in such crystals was in the range  $10^4 - 10^5 \text{ cm}^{-2}$ .

Figs. 1.3 and 1.4 show a cross-section of the GeSi crystal and the corresponding plot of Si distribution along the axis. Regions with a pronounced cellular structure are seen in the photo. Some correlation exists between the value of concentration and the character of perturbations. Nevertheless, the character of this correlation remains ambiguous. The photo exhibits different growth morphologies for equal values of concentrations. This effect takes place because of the complex behavior of temperature, concentration and

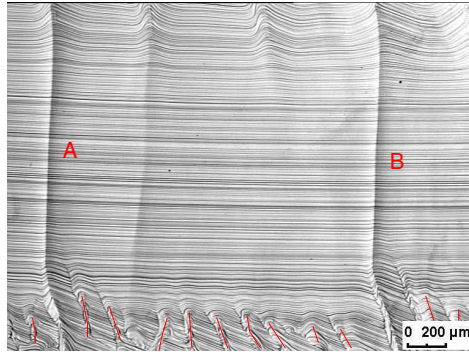


**Figure 1.5:** Cross section of the GeSi crystals with cellular structure.

flow fields near the growth surface.

Fig. 1.5 is a good example of different growth regimes. This photo shows evolution of the interface. Shapes of the crystal surface at different moments are represented by striation lines. One can observe a transition from a region with cellular growth to a cell-free one and again to one with cellular growth (from top to bottom). The top region contains some traces of cellular structure, then they disappear. Two lines, *A* and *B*, correspond to unrecoverable changes in the crystal, whose nature is currently not clear. The crystal structure seems to be distorted significantly in those places. In the bottom region cells appear again. It is clearly seen that the cell-orientation is not perpendicular to the crystal boundary, indicated by the striation lines. The traces “A” and “B” have different orientations in the three regions. This effect is probably related to tangential flow near the crystal surface. The local maxima (tips of the pyramids) migrate in opposition to the flow direction.

Almost all grown crystals have a mosaic structure. Morphology manifold of the structure leads to a yield of only 60%; the other 40% of the crystals have a mosaicity that is too large.

The following cell properties were observed in experiments:

- Morphology of the cellular structure depends on crystal anisotropy.
- Growth direction defines the stability of the crystal interface.
- Cellular structure shows dependence on the flow.
- Fluctuations in the system cause instability of the cellular structure.

## 1.2 Modeled system

The investigated GeSi crystals are grown by the Czochralski method [70, 2]. Our goal is to better understand the pattern formation phenomena. We therefore focus our attention on the processes in the vicinity of the melt-crystal surface. The computational domain is a small region near the interface. Movement of the interface and behavior of concentration and flow fields are computed in this domain. The boundary conditions for the concentration and flow fields are estimated or taken from a macroscopic simulation of the processes in the furnace [56].

The processes on the crystal surface are the focus of the modeling. Movement of the phase-boundary and concentration balance in the solid and liquid phases denotes the phase transition. A phase-field method [53, 30] is chosen for describing these processes. This method has already been applied for binary alloys by W.J. Boettinger and J.A. Warren, see [7]. This model allows us to compute growth kinetics and surface-tension effects.



### 1.3 Numerical methods

The phase-field equations accomplished by the Navier-Stokes equation need to be solved. For this purpose, we used a mix of explicit finite difference methods and lattice-kinetic methods. The recent work of I. Rasin, S. Succi and W. Miller [47] demonstrates the efficiency of such mixed algorithms. In the numerical model, the phase-field equation is solved by an explicit finite-difference (EFD) scheme and a lattice kinetic scheme is used for solving the advection-diffusion equation. Melt flow is simulated with the Lattice Bhatnagar-Gross-Krook (LBGK) method [71, 59].

Originally, the passive scalar (temperature or concentration) transport was calculated by an EFD scheme. This method allowed us to get results for the NiCu alloys, but in the case of the GeSi crystal it was inefficient because of stability restrictions on the time step. The best alternatives to the EFD scheme are LK schemes [55, 58, 48]. Series of tests were made in order to study the different properties of the new scheme, and to compare it with other methods. The question of an adaptive time step is also discussed.

### 1.4 Thesis structure

The PhD thesis consists of four main chapters: “LK methods”, “Phase-field models”, “Solidification in binary alloys” and “Cellular growth in GeSi crystals”. Each of the four chapters contains original results, as obtained during this work. In the first three chapters, tools and methods used in the GeSi numeric model are introduced and discussed.

In the first chapter, we discuss different types of LK methods. The chapter consists of two sections: the first, which contains an introduction to the classic Lattice-Boltzmann method [71, 59], used for the flow computation in the melt, and the second which describes the lattice kinetic methods for passive-scalar transport. We present the newly developed multi-relaxation lattice-kinetic method for solving the advection-diffusion equation.

In the chapter “Phase-field models”, different aspects related to the phase-field model are considered. The chapter begins with the description of the basic ideas and classic equations related to the model. The second section introduces the modified phase-field (MPF) model. The necessity of the MPF model was recognized after meso-scale simulations of GeSi alloys. These simulations showed that the classic model becomes unstable at this scale. We developed modified phase-field equations as an answer to the perceived instability. The MPF model was verified by the dendritic growth and computations of the equilibrium form of the crystal in the 2D and the 3D cases. In addition, the simulations of the dendritic growth allowed us to test coupling of the MRLK method with phase-field equations. The heat transport was implemented through the multi-relaxation lattice kinetic (MRLK) scheme with an adaptive time step.

The third chapter is dedicated to solidification in binary alloys. Different phase-field models for binary alloys are discussed. There are two main models: one from A.A. Wheeler, W.J. Boettinger and G.B. McFadden (WBM model)[69] and another from S.G. Kim, W.T. Kim and T. Suzuki (KKS model)[30]. The difference between these two models is discussed in the work. The KKS model with MPF equations was taken as the basis of this work. The obtained model

was applied for simulation of the NiCu alloy and after that for simulation of the GeSi alloy.

Numerical simulations of the GeSi crystals are considered in the fourth chapter. It begins with descriptions of experimental basics of the Czochralski growth and estimations of the crucible processes. These estimations are used later in our mesoscopic simulations. The chapter continues on to give descriptions of the numerical results. The simulations of pattern formation were first done without flow. The resulting patterns have the size predicted from the theory of cellular growth, but they are much larger than the experimentally observed patterns. Modeling with the presence of flow allowed us to explain the experimentally observed effects. The size of the obtained patterns is similar to the cell size in the experiment. Additionally, in this section, we discuss problems related to material data. Specifically, we have undertaken several simulations for two different values of the diffusion coefficients of Si in Ge melt; one of these two values was taken from experimental measurements [15], and the other from the molecular dynamic simulation [74].

# Chapter 2

## Lattice kinetic methods

Macroscopic simulations of crystallization processes are always related to modeling of mass-transport. The mass-transport processes are described by corresponding equations, which need to be solved. In our case, they are the Navier-Stokes equation and the advection-diffusion equation. In this chapter, we present the methods used later on in this thesis for solving the transport equations.

In our work, we use the Lattice Bhatnagar-Gross-Krook (LBGK) model for computation of liquid flow. The advection-diffusion equation is solved by the Lax-Wendroff [60] or by the multi-relaxation lattice kinetic method [48]. The main advantage of these methods is simplicity, meaning that it is possible to obtain an efficient and flexible numerical method and to integrate it in an external code without much programming effort. Another advantage is its high efficiency in the case of parallel computing, which is very important in the 3D case.

This chapter begins with a short description of the classic LK methods for flow simulations. The LK methods for simulation of the diffusion and advection-diffusion equations are discussed in

the second section.

## 2.1 The lattice-Boltzmann and the LBGK methods

Flow of an incompressible liquid is described by the Navier-Stokes equation:

$$\partial_t u_\alpha + u_\beta \nabla_\beta u_\alpha = -\frac{1}{n} \nabla_\alpha P + \nu \Delta u, \quad (2.1)$$

where  $\vec{u}$  is the flow velocity,  $n$ ,  $P$  and  $\nu$  are density, pressure and kinematic viscosity. Numerical solutions of this equation can be obtained by the lattice-Boltzmann method (LBM) [71, 59]. Unlike traditional numerical methods solving this equation directly, the LBM simulates a dynamic of a lattice gas.

The LBM is based on the solving of the Boltzmann equation in the discrete phase space (in lattice units  $\delta_t = \delta_x = 1$ ):

$$f_i(\vec{r} + \vec{a}_i, t + 1) - f_i(\vec{r}, t) = (\text{St } f)_i, \quad (2.2)$$

where  $f_i(r)$  is the number of quasi-particles with the velocity  $\vec{a}_i$  at  $\vec{r}$ . The  $(\text{St } f)_i$  is a collision term, which will be specified below. Thus, the problem of solving the non-linear Navier-Stokes equation is replaced by the solving of the system of coupled linear hyperbolic equations. These hyperbolic equations describe motion and interaction of quasi-particles on the regular lattice. In other words, the model simulates the kinetics of a lattice gas.

The macroscopic quantities, such as density and velocity, are obtained by moment integrations of the distribution function:

$$\rho(\vec{r}) = \sum_i f_i(\vec{r}), \quad \vec{u}(\vec{r}) = \frac{1}{\rho(\vec{r})} \sum_i \vec{a}_i f_i(\vec{r}). \quad (2.3)$$

Please note that  $\rho$  is the density of the lattice gas. The physical pressure is related to this density through the equation of state, [73]:  $P = \rho a_s^2$ , where  $a_s$  is sound speed in the lattice gas. Its collision term can be tuned in such a way that the appropriate macroscopic equations will be obtained. The macroscopic equations are derived from the LBM equation by means of a multiscale Chapman-Enskog expansion [57]. The kinetic nature of the LBM introduces a number of advantages, such as linearity of the convection operator and recovery of the Navier-Stokes equations at the nearly incompressible limit, thus avoiding the need for solving difficult Poisson equations for the pressure.

### 2.1.1 Collision term for incompressible flow

The collision term in a general case is represented in the following matrix form:

$$(\mathbf{St} f)_i = \sum_j \Omega_{ij} (f_j(\vec{r}, t) - f_j^{eq}(\vec{r}, t)), \quad (2.4)$$

where  $\Omega_{ij}$  is, the so called, relaxation matrix. The matrix representation contains both the physical and numerical parameters [4]. These parameters are explicitly seen in the spectra representation of the matrix. Each eigenvector corresponds to a physical or “ghost”, field and eigenvalues define the relaxation properties of corresponding fields. By adjustment of the eigenvalues, the necessary behavior of the physical parameters can be achieved [21, 71, 59].

The LBGK<sup>1</sup> method is the simplest realization of the previously considered scheme with the relaxation matrix,  $\Omega_{ij} = \omega \delta_{ij}$ . The cor-

---

<sup>1</sup>LBGK - Lattice Bhatnagar-Gross-Krook

responding equation for the distribution function takes the form:

$$f_i(\vec{r} + \vec{a}_i, t + 1) - f_i(\vec{r}, t) = \omega(f_i(\vec{r}, t) - f_i^{eq}(\vec{r}, t)). \quad (2.5)$$

This scheme has only one governing parameter,  $\omega$ , which is related with viscosity  $\nu$  by the following expression:

$$\omega = \frac{N_d}{2\nu^* a_s^{-2} + 1}.$$

The equilibrium distribution function is a third order expansion of the Maxwell distribution:

$$f_i^{eq} = w_i \rho \left( 1 + \frac{1}{a_s^2} u_\alpha^* a_{i\alpha} + \frac{Q_{i\alpha\beta} u_\alpha^* u_\beta^*}{2a_s^4} \right), \quad (2.6)$$

where  $w_i$  is a weight parameter and  $a_s^2 = \sum_i w_i a_{ix}^2 = \sum_i w_i a_{iy}^2 = 3/5$  is the lattice sound speed.  $Q_{i\alpha\beta} \equiv a_{i\alpha} a_{i\beta} - a_s^2 \delta_{\alpha\beta}$ . The rescaled value of flow velocity is  $u_\alpha^* \equiv u_\alpha \frac{\delta_t}{\delta_x}$ .

## 2.2 LK methods for passive scalar transport

The first appearance of diffusion simulation with a kinetic method was in the article of E.G. Flekkøy [16]. This method was modified by X. Shan and G. Doolen [55]. They took a classic LBGK method and put the flow velocity to zero. The obtained scheme reproduces pure diffusion. Later, H. W. Stockman et al. [58] studied the possibility of reducing the number of the velocity vectors, e.g. four directions were used instead of nine in the 2D case. As a result, there was a small increase in the numerical anisotropy. R.G.M. van der Sman and M.H. Ernst considered a matrix approach [64], in contrast to both other schemes which are based on the LBGK approach (single

relaxation). The matrix approach provides more freedom in manipulations with ghost fields as compared to the single relaxation method. They applied it for pure diffusion problem without advection. By tuning the matrix components, they obtained better numeric properties than the single-relaxation method as proposed by H. W. Stockman, et al. We propose an extension of the matrix method to the advection diffusion case. Our method requires less memory than the methods of E.G. Flekkøy [16] and X. Shan, G. Doolen [55], and R.G.M. van der Sman, M.H. Ernst [64], and has smaller numerical anisotropy than the technique proposed by H. W. Stockman et al. [58].

The advection-diffusion equation is:

$$\partial_t \rho + \nabla \cdot (\rho \vec{u}) = \nabla \cdot D \nabla \rho, \quad (2.7)$$

where  $\rho$  is the passive scalar, e.g.: temperature or concentration of a component,  $\vec{u}$  is the flow velocity and  $D$  is the diffusion coefficient, generally a function of coordinates  $D = D(\vec{r})$ .

The governing kinetic Boltzmann equation for  $f_i$  takes the following relaxation form:

$$f_i(\vec{r} + \vec{a}_i, t + 1) - f_i(\vec{r}, t) = \sum_j \Omega_{ij} (f_j^{eq}(\vec{r}, t) - f_j(\vec{r}, t)), \quad (2.8)$$

where  $f_i$  represents the probability of finding a particle with speed  $\vec{a}_i$  at position  $\vec{r}$  and time  $t$ .

The concentration  $\rho$  and flux  $\mathbf{J}$  values are related to  $f_i$  in the following way:

$$\rho = \sum_i f_i, \quad \mathbf{J}_\alpha = \sum_i a_{i\alpha} f_i, \quad (2.9)$$

$\alpha = 1, \dots, N_d$  is spatial index. It should be noted that the flux of quasi particles,  $\vec{\mathbf{J}}$ , is not the physical flux,  $\vec{J}_{phys} \equiv u\rho - D\nabla\rho$ , but both fluxes are related and this relation depends on the used model.



### 2.2.1 Single-relaxation LK (SRLK) model

Let us show an analysis of the method proposed in the articles [16, 55]. The classic LBGK method for the Navier-Stokes equation, introduced in Section 2.1.1, has been applied to the diffusion problem. Let us call this model a single-relaxation LK model. The relaxation matrix is taken in diagonal form:

$$\Omega_{ij} = \delta_{ij}\omega.$$

The equilibrium distribution is taken in the same way as for the flow case (2.6):

$$f_i^{eq} = w_i \rho \left( 1 + \frac{1}{a_s^2} u_\alpha^* a_{i\alpha} + \frac{Q_{i\alpha\beta} u_\alpha^* u_\beta^*}{2a_s^4} \right),$$

where  $\vec{u}$  is a velocity of an external flow.

The Taylor expansion of the equation (2.8) yields the system of two hyperbolic equations for  $\rho$  and  $\vec{J}$ :

$$\dot{\rho} + \nabla_\alpha \mathbf{J}_\alpha + \frac{1}{2} \ddot{\rho}_i + \nabla_\alpha \dot{\mathbf{J}}_\alpha + \frac{1}{2} \nabla_\alpha \nabla_\beta \mathbf{P}_{\alpha\beta} = \omega(\rho^{eq} - \rho), \quad (2.10)$$

$$\dot{\mathbf{J}}_\alpha + \nabla_\beta \mathbf{P}_{\alpha\beta} + \frac{1}{2} \ddot{\mathbf{J}}_\alpha + \nabla_\beta \dot{\mathbf{P}}_{\alpha\beta} + \frac{1}{2} \nabla_\beta \nabla_\gamma \mathbf{M}_{\alpha\beta\gamma} = \omega(\mathbf{J}_\alpha^{eq} - \mathbf{J}_\alpha), \quad (2.11)$$

where  $\mathbf{P}_{\alpha\beta} \equiv \sum_i a_{i\alpha} a_{i\beta} f_i$ ,  $\mathbf{M}_{\alpha\beta\gamma} \equiv \sum_i a_{i\alpha} a_{i\beta} a_{i\gamma} f_i$  are higher order moments.

Let us further suppose that  $\mathbf{P}$  and  $\mathbf{M}$  are near their equilibrium values:

$$\mathbf{P}_{\alpha\beta} \approx \mathbf{P}_{\alpha\beta}^{eq} = \rho \sum_i w_i a_{i\alpha} a_{i\beta} \left( 1 + \frac{Q_{i\gamma\delta} u_\gamma^* u_\delta^*}{2a_s^4} \right) \quad (2.12)$$

$$= \rho \left( a_s^2 \delta_{\alpha\beta} + \frac{u^{*2} \delta_{\alpha\beta}}{2a_s^2} \left( \frac{1}{3} - a_s^2 \right) + \frac{1}{3} \frac{u_\alpha^* u_\beta^*}{a_s^2} \right), \quad (2.13)$$

$$\mathbf{M}_{\alpha\beta\gamma} \approx \mathbf{M}_{\alpha\beta\gamma}^{eq} = \rho a_s^2 u_\delta^* \delta_{\alpha\beta\gamma\delta}.$$

The previous expressions were obtained only with the assumption that the expression  $\sum_i w_i a_{i\alpha} a_{i\beta} a_{i\gamma} a_{i\delta}$  does not contain the anisotropic term, see Eqs. (D.2) and (D.4). This assumption fixes  $w_\times$ :

$$2D : w_+ = 4w_\times, \quad 3D : w_+ = 2w_\times.$$

Let us note that for the case with  $a_s^2 = \frac{1}{3}$  (it corresponds to the case with rest particles)  $\mathbf{P}_{\alpha\beta}^{eq} = \rho (a_s^2 \delta_{\alpha\beta} + u_\alpha u_\beta)$ . Such a value of the  $a_s$  can be achieved by taking the weight parameter in the following form:

$$\begin{aligned} 2D : \quad & w_0 = \frac{4}{9}, \quad w_+ = \frac{1}{9}, \quad w_\times = \frac{1}{36}, \\ 3D : \quad & w_0 = \frac{1}{3}, \quad w_+ = \frac{1}{18}, \quad w_\times = \frac{1}{36}. \end{aligned}$$

Since mass is conserved, and momentum is not, we make the following assumption:

$$\rho^{eq} = \rho, \quad \mathbf{J}_\alpha \neq \mathbf{J}_\alpha^{eq} = \rho u_\alpha.$$

Now, equations (2.10) and (2.11) can be transformed by assuming that  $\dot{\mathbf{J}}_\alpha \approx \dot{\mathbf{J}}_\alpha^{eq} \approx -u_\alpha u_\beta \nabla_\beta \rho$  and  $\ddot{\rho} \approx u_\alpha u_\beta \nabla_\alpha \nabla_\beta \rho$ :

$$\begin{aligned} \dot{\rho} + \nabla_\alpha u_\alpha \rho + \nabla_\alpha \mathbf{J}_\alpha^{ne} - \frac{1}{2} u_\alpha u_\beta \nabla_\alpha \nabla_\beta \rho + \frac{1}{2} (a_s^2 \delta_{\alpha\beta} + u_\alpha u_\beta) \nabla_\alpha \nabla_\beta \rho &= 0, \\ -u_\alpha u_\beta \nabla_\beta \rho + (a_s^2 \delta_{\alpha\beta} + u_\alpha u_\beta) \nabla_\beta \rho &= -\omega \mathbf{J}_\alpha^{ne}. \end{aligned}$$

Thus, it is seen, that the effect of the additional diffusion has disappeared from these equations:

$$\dot{\rho} + \nabla_\alpha u_\alpha \rho + \nabla_\alpha \mathbf{J}_\alpha^{ne} + \frac{1}{2} a_s^2 \Delta \rho = 0, \quad (2.14)$$

$$a_s^2 \nabla_\alpha \rho = -\omega \mathbf{J}_\alpha^{ne}. \quad (2.15)$$

The relation between  $D$  and  $w$  is extracted from the comparison between (2.1) and the previous equations:

$$D^* = a_s^2 \left( \frac{1}{w} - \frac{1}{2} \right).$$

The considered method has no stability restrictions on  $D^*$ , in other words the time step can be of an arbitrary length. The drawback is that 9 fields in the 2D case and 19 fields in the 3D case are needed in order to simulate the diffusion equation.

### 2.2.2 Multi-relaxation LK (MRLK) model

The main goal in constructing this model was to achieve the same features as in the classic single-relaxation LK model, but with smaller memory requirements. This can be realized by decreasing the number of components of the distribution function. Only the fields corresponding to orthogonal velocities are taken: four fields in the 2D case ( $i = 1..4$ ) and six fields in the 3D case ( $i = 1..6$ ), D2Q4 and D3Q6 spaces respectively. The number of floating-point operations per lattice node is also decreased by such modification leading to increased performance. H. W. Stockman et al. [58] tested the single relaxation model D2Q4 space. This model has increased numerical anisotropy in comparison with the previously discussed model. We introduce here a multi-relaxation LK. An additional advantage of the MRLK is its easy expansion in a case with anisotropic diffusion [48, 47].

The Taylor expansion of the equation (2.8) yields the system of two hyperbolic equations for  $\rho$  and  $\vec{J}$ :

$$\dot{\rho} + \nabla_\alpha \mathbf{J}_\alpha + \frac{1}{2} \ddot{\rho}_i + \nabla_\alpha \dot{\mathbf{J}}_\alpha + \frac{1}{2} \nabla_\alpha \nabla_\beta \mathbf{P}_{\alpha\beta} = \sum_{ij} \Omega_{ij} (f_j^{eq} - f_j), \quad (2.16)$$

$$\dot{\mathbf{J}}_\alpha + \nabla_\beta \mathbf{P}_{\alpha\beta} + \frac{1}{2} \ddot{\mathbf{J}}_\alpha + \nabla_\beta \dot{\mathbf{P}}_{\alpha\beta} + \frac{1}{2} \nabla_\beta \nabla_\gamma \mathbf{M}_{\alpha\beta\gamma} = \sum_{ij} a_{i\alpha} \Omega_{ij} (f_j^{eq} - f_j). \quad (2.17)$$

Furthermore, it is posited that density is conserved, and the current density on a tensorial inverse time scale is  $\Lambda_{\alpha\beta}$ . In other

**Table 2.1:** Weight coefficients and sound speeds in the 2D and 3D cases.

	2D	3D
$w_i$	$1/4, i = 1..4$	$1/6, i = 1..6$
$a_s^2$	$1/2$	$1/3$

words, collisions realize the following relaxation dynamics  $\frac{\delta \rho}{\delta t} = 0$  and  $\frac{\delta J_\alpha}{\delta t} = -\Lambda_{\alpha\beta}(J_\beta - J_\beta^{eq})$ . This implies the following algebraic constraints:

$$\sum_i \Omega_{ij} = 0, \quad \sum_i a_{i\alpha} \Omega_{ij} = \sum_\beta \Lambda_{\alpha\beta} a_{j\beta},$$

where  $\Lambda_{\alpha\beta}$  are free parameters to be fine-tuned to obtain the desired macroscopic equations.

Using these properties, we obtain:

$$\dot{\rho} + \nabla_\alpha \mathbf{J}_\alpha + \frac{1}{2} \ddot{\rho}_i + \nabla_\alpha \dot{\mathbf{J}}_\alpha + \frac{1}{2} \nabla_\alpha \nabla_\beta \mathbf{P}_{\alpha\beta} = 0, \quad (2.18)$$

$$\dot{\mathbf{J}}_\alpha + \nabla_\beta \mathbf{P}_{\alpha\beta} + \frac{1}{2} \ddot{\mathbf{J}}_\alpha + \nabla_\beta \dot{\mathbf{P}}_{\alpha\beta} + \frac{1}{2} \nabla_\beta \nabla_\gamma \mathbf{M}_{\alpha\beta\gamma} = \Lambda_{\alpha\beta} (\mathbf{J}_\beta^{eq} - \mathbf{J}_\beta). \quad (2.19)$$

Since mass is conserved, and momentum is not, we make the following assumption:

$$\rho^{eq} = \rho, \quad \mathbf{J}_\alpha \neq \mathbf{J}_\alpha^{eq} = \rho u_\alpha.$$

This choice delivers the following expression for  $f_i^{eq}$ :

$$f_i^{eq} = w_i \rho \left( 1 + \frac{1}{a_s^2} u_\alpha^* a_{i\alpha} \right),$$

where  $w_i$  are written in Table.2.1.

Next, we assume that  $\mathbf{P}$  and  $\mathbf{M}$  are near their equilibrium values:

$$\mathbf{P}_{\alpha\beta} \approx \mathbf{P}_{\alpha\beta}^{eq} = \rho a_s^2 \delta_{\alpha\beta}, \quad \mathbf{M}_{\alpha\beta\gamma} \approx \mathbf{M}_{\alpha\beta\gamma}^{eq} = \rho a_s^2 u_\delta \delta_{\alpha\beta\gamma\delta}. \quad (2.20)$$

Thus, in the continuum limit and within the near-equilibrium approximation, the discrete equation (2.8) goes towards the non-isotropic advection-diffusion equation in the conservative form:

$$\dot{\rho} + \nabla \cdot (\rho \vec{u}) = \nabla_\alpha (D_{\alpha\beta} \nabla_\beta \rho), \quad (2.21)$$

with the tensor diffusivity defined by the following expression:

$$D_{\alpha\beta} \equiv \left( \frac{1}{2} \delta_{\alpha\gamma} - u_\alpha u_\gamma \right) \left( (\Lambda^{-1})_{\gamma\beta} - \frac{1}{2} \delta_{\gamma\beta} \right). \quad (2.22)$$

Note that due to the conservative form of the equation (2.21) this tensor diffusivity may exhibit an explicit spatial dependence. The relation (2.22) fixes the relaxation matrix  $\Lambda_{\alpha\beta}$  in terms of the prescribed diffusion tensor  $D_{\alpha\beta}$ . It is important to remark that the flow-dependent correction  $u_\alpha u_\gamma$  in the above equation stems from the *diabatic* term  $\partial_{tt}\rho$ , which is implicitly contained in the equations (2.19). This flow-dependent (non-isotropic) effect can be re-absorbed into an isotropic diffusivity by appropriate tuning of the scattering matrix  $\Lambda$ . From equation (2.22), it is clear that unless one moves to higher-order connectivity lattices (see Appendix), such a recovery can only be obtained within a matrix LK formulation. For the case of isotropic diffusion,  $D_{\alpha\beta} = D\delta_{\alpha\beta}$ , the matrix  $\Lambda$  is:

$$\Lambda_{\alpha\beta} = \frac{2}{\lambda_1} \delta_{\alpha\beta} + \frac{2b}{\lambda_1 \lambda_2} \frac{u_\alpha u_\beta}{a_s^2}, \quad b \equiv -\frac{2D^*}{a_s^2}, \quad (2.23)$$

where  $\lambda_1 \equiv 1 + b$ ,  $\lambda_2 \equiv 1 + b - \frac{u^{*2}}{a_s^2}$ . It is worth emphasizing that even for the case of isotropic diffusion, this matrix cannot be diagonal unless the fluid is locally one-dimensional, that is  $u_x u_y = 0$ . The collision matrix can then be built according to a (generalised) spectral decomposition [64, 8]:

$$2D : \Omega_{ij} = \sum_{k=1}^2 V_i^{(k)} \sum_{l=1}^2 \Lambda_{kl} V_j^{(l)} + \lambda_3 V_i^{(3)} V_j^{(3)},$$

$$3D : \Omega_{ij} = \sum_{k=1}^3 V_i^{(k)} \sum_{l=1}^2 \Lambda_{kl} V_j^{(l)} + \lambda_3 V_i^{(3)} V_j^{(3)} + \lambda_4 V_i^{(4)} V_j^{(4)},$$

where  $V_i^{(k)}$  are orthonormal eigenvectors:

$$\begin{aligned} 2D : \quad V^{(0)} &= \frac{1}{4} (1, 1, 1, 1), \\ V^{(1)} &= \frac{a_{xi}}{2}, \quad V^{(2)} = \frac{a_{yi}}{2}, \\ V^{(3)} &= \frac{1}{2} a_{xi}^2 - 2V^{(0)}, \\ 3D : \quad V^{(0)} &= \frac{1}{6} (1, 1, 1, 1, 1, 1), \\ V^{(1)} &= \frac{a_{xi}}{2}, \quad V^{(2)} = \frac{a_{yi}}{2}, \quad V^{(3)} = \frac{a_{zi}}{2}, \\ V^{(4)} &= \frac{1}{\sqrt{12}} (3a_{xi}^2 - 6V^{(0)}), \quad V^{(5)} = \frac{1}{2} a_{xi}^2 + a_{yi}^2 - 3V^{(0)}. \end{aligned}$$

The vectors  $V^{(4)}$  and  $V^{(5)}$  are chosen to be orthogonal to other vectors but they have no explicit physical sense and can certainly be replaced by their arbitrary linear combination. Note that the collision matrix projects zero on the first eigenvector  $\lambda_0 = 0$  because of mass conservation.

The explicit form of the collision matrix in the 2D case is:

$$\Omega = \frac{1}{2} \begin{bmatrix} \Lambda & -\Lambda \\ -\Lambda & \Lambda \end{bmatrix} + \lambda_3 \begin{bmatrix} P_3 & P_3 \\ P_3 & P_3 \end{bmatrix}, \quad (2.24)$$

where  $\Lambda$  denotes the  $2 \times 2$  block  $\Lambda_{\alpha\beta}$  and  $P_3 = \frac{1}{4} \begin{bmatrix} 1 & -1 \\ -1 & 1 \end{bmatrix}$  is the projector associated with the third eigenvector. The corresponding form in the 3D case is:

$$\Omega = \frac{1}{2} \begin{bmatrix} \Lambda & -\Lambda \\ -\Lambda & \Lambda \end{bmatrix} + \lambda_4 \begin{bmatrix} P_4 & P_4 \\ P_4 & P_4 \end{bmatrix} + \lambda_5 \begin{bmatrix} P_5 & P_5 \\ P_5 & P_5 \end{bmatrix}, \quad (2.25)$$

where  $\Lambda$  denotes the  $3 \times 3$  block  $\Lambda_{\alpha\beta}$  and

$$P_4 = \frac{1}{12} \begin{bmatrix} 4 & -2 & -2 \\ -2 & 1 & 1 \\ -2 & 1 & 1 \end{bmatrix}, \quad P_5 = \frac{1}{4} \begin{bmatrix} 0 & 0 & 0 \\ 0 & 1 & -1 \\ 0 & -1 & 1 \end{bmatrix},$$

are the projectors associated with the fourth and fifth eigenvectors.

The eigenvalues of the matrix  $\Omega$  are:

$$\lambda_0 = 0, \quad \lambda_1 = \frac{2}{1 + 4D^*}, \quad \lambda_2 = \frac{2(1 - 2u^{*2})}{1 + 4D^* - 2u^{*2}}, \quad \lambda_3,$$

which corresponds to the following kinetic eigenvectors:

$$V_i^{(0)} = 1, \quad W_i^{(1)} = (a_{ix} \cos \theta - a_{iy} \sin \theta),$$

$$W_i^{(2)} = (a_{ix} \sin \theta + a_{iy} \cos \theta), \quad V_i^{(3)} = a_{ix}^2 - a_{iy}^2.$$

The eigenvectors  $W^{(1)}$  and  $W^{(2)}$  are obtained by rotating  $a_{ix}$  and  $a_{iy}$  by the angle  $\theta$  defined by the local flow velocity,  $u_x = u \cos \theta$ ,  $u_y = u \sin \theta$ . When the flow is at rest ( $u = 0$ ), this transformation degenerates and goes back to the standard eigenvectors  $V_i^{(k)}$ .

The numerical scheme is stable for all values of  $D^*$  and  $u^*$  so that the eigenvalues of  $\Omega_{ij}$  lie within the interval  $0 < \lambda_k < 2$  that is:

$$0 < \frac{2(1 - 2u^{*2})}{1 + 4D^* - 2u^{*2}} < 2, \quad 0 < \lambda_3 < 2.$$

These limitations imply  $u^{*2} < 1/2$ , namely Mach number  $Ma^2 = u^{*2}/a_s^2 < 1$ , regardless of the value of  $D^* > 0$ . On the other hand, due to the near-equilibrium approximation, it is clear that for very small values of  $D^*$ , such as  $\lambda_1$  and  $\lambda_2$  approaching the upper bound 2, the scheme exhibits long-lasting oscillations, which may hamper the numerical efficiency of the method.

The Eqs. (2.18) and (2.19) are accomplished with the third equation for  $P_{\alpha\beta}$ , which is written for different components separately:

$$\begin{aligned}\dot{\mathbf{P}}_{xx} &= \lambda_3 \left( \mathbf{P}_{xx}^{eq} - \mathbf{P}_{xx} - \frac{1}{2}(\rho^{eq} - \rho) \right), \\ \dot{\mathbf{P}}_{yy} &= \lambda_3 \left( \frac{1}{2}(\rho^{eq} - \rho) - (\mathbf{P}_{yy}^{eq} - \mathbf{P}_{yy}) \right).\end{aligned}$$

The condition (2.20) follows from this equation by assuming that the left-hand side is small in comparison with the right-hand side. In other words,  $\lambda_3$  should be as large as possible, normally  $\lambda_3 = 2$ . It should be mentioned that  $\lambda_3 = 0$  causes strong grid anisotropy.

We do not provide here the same analysis for the 3D case because of its similarity to that of the 2D case. The eigenvalues  $\lambda_4$  and  $\lambda_5$  have similar influences on the scheme to  $\lambda_3$  in the 2D case and they are taken, therefore, as  $\lambda_4 = \lambda_5 = 2$ . The Eq. (2.25) can be rewritten for the case  $\lambda_4 = \lambda_5 = \lambda_I$

$$\Omega = \frac{1}{2} \begin{bmatrix} \Lambda & -\Lambda \\ -\Lambda & \Lambda \end{bmatrix} + \lambda_i \begin{bmatrix} P_I & P_I \\ P_I & P_I \end{bmatrix}, \quad P_I \equiv \frac{1}{6} \begin{pmatrix} 2 & -1 & -1 \\ -1 & 2 & -1 \\ -1 & -1 & 2 \end{pmatrix}. \quad (2.26)$$

### 2.2.3 Adaptive time step

Since it was indicated that the LK methods have no stability restriction on the time step, an adaptive time stepping procedure can be introduced. The time step is defined by an error estimator, which is introduced in this section.

An adiabatic approximation was made through the analysis of numerical methods discussed in the previous section. This approximation contains two assumptions: the first, that the second and third order moments are near their equilibrium values, the second,



that  $\frac{\partial}{\partial t} J^{ne} \ll w J^{ne}$ . By using this criteria, the so called, *diabatic* parameter  $\epsilon$  is introduced:

$$\epsilon \equiv \frac{(\partial \mathbf{J}^{eq} / \partial t)}{\lambda_J \mathbf{J}^{eq}}, \quad \epsilon \ll 1. \quad (2.27)$$

The maximal value of  $\epsilon$  characterizes the numerical error of the method. This statement will be tested in Section 2.2.4. If  $\max \epsilon < \epsilon_{min}$ , the time step can be increased and, vice versa, if  $\max \epsilon > \epsilon_{min}$ , the time step should be decreased.

The changing of the time step requires renormalization in the distribution function. It follows from the changing of the velocities  $\vec{a}_i$ :

$$\vec{a}_i^+ = \alpha_{dt} \vec{a}_i, \quad \alpha_{dt} \equiv \delta_t^+ / \delta_t, \quad (2.28)$$

where  $\vec{a}_i$  and  $\vec{a}_i^+$  are grid velocity vectors before and after the changing of the time step, respectively. This transformation is equivalent to the cooling of the lattice gas, in the sense that sonic speed  $a_s$ , plays the role of the temperature, and the distribution function of quasi-particles is renormalized according to this cooling. The requirements for concentration and flux are:

$$\rho^+ = \rho, \quad \vec{J}^+ = \alpha_{dt} \vec{J}. \quad (2.29)$$

Here  $\vec{J}$  is the physical flux,  $\vec{J} = -D \vec{\nabla} \rho$ , not to be confused with  $\vec{\mathbf{J}}$ , the flux of the lattice gas. In other words, these physical parameters should be invariant under the ‘‘cooling’’ transformation. In order to satisfy the invariance of  $\rho$ , the following invariance of equilibrium distribution functions is necessary:

$$f_i^{eq+} = f_i^{eq}. \quad (2.30)$$

The invariance of the flux is rewritten as:

$$\vec{\nabla} \rho = \vec{\nabla} \rho^+ \implies \vec{J}^{ne+} = \alpha_J J^{ne}, \quad \alpha_J \equiv \lambda_J / \lambda_J^+. \quad (2.31)$$

**Table 2.2:** Comparison of the LB and MLW methods for the case of pure diffusion.  $D = 1$ ,  $\lambda_3 = 1$ 

$\delta_t$	MRLK $L_2$	MLW $L_2$	MRLK $L_\infty$	MLW $L_\infty$
2.5	$2.78 \times 10^{-2}$	-	$1.56 \times 10^{-2}$	-
1	$3.26 \times 10^{-3}$	-	$1.83 \times 10^{-3}$	-
0.5	$7.02 \times 10^{-4}$	-	$4.12 \times 10^{-4}$	-
0.25	$2.27 \times 10^{-5}$	$2.27 \times 10^{-5}$	$2.94 \times 10^{-4}$	$2.94 \times 10^{-4}$
0.1	$3.10 \times 10^{-5}$	$6.8 \times 10^{-6}$	$3.47 \times 10^{-4}$	$5.76 \times 10^{-5}$
0.01	$3.84 \times 10^{-5}$	$2.18 \times 10^{-5}$	$4.28 \times 10^{-4}$	$2.80 \times 10^{-4}$

The set of equations (2.30) and (2.31) permits many solutions. We renormalise the distribution functions by the following :

$$f_i^+ = f_i^{eq} + \alpha_J f_i^{ne}. \quad (2.32)$$

### 2.2.4 Numerical tests

In the following section we present some test simulations to validate the kinetic scheme. The finite-difference Modified Lax-Wendroff (MLW) scheme is chosen as a reference method.

#### Isotropic diffusion

We consider the time evolution of a Gaussian density profile under the effect of constant diffusion and without flow, i.e. zero cell-Peclet number ( $Pe_c = \frac{U\delta_x}{D}$ ).

The initial distribution is given by Eq. (B.2): The results of the simulation for the case  $\sigma_0 = 14.1$ ,  $\rho_0 = 10^3$  on a  $250 \times 250$  grid, are summarized in Table 2.2. This table reports deviations from the exact solution for both LB and MLW schemes at time  $t = 100$  (physical

**Table 2.3:** Numerical error for MRLK method in the 3D case,  $\lambda_3 = 1$ ,  $200 \times 200 \times 200$ ,  $\sigma_0 = 14.1$ ,  $D = 1$ ,  $t = 100$ . Computations have been made on the a Pentim 4 Xeon 2.4GHz processor.

$\delta_t$	$L_2$	$L_\infty$	Computation time, s
2.5	$2.36 \times 10^{-4}$	$5.01 \times 10^{-3}$	47
1	$1.84 \times 10^{-5}$	$6.31 \times 10^{-4}$	111
0.25	$8.57 \times 10^{-7}$	$2.72 \times 10^{-5}$	430

units) in the  $L_2$  and  $L_\infty$  norm. They are defined as:

$$\|\delta\rho\|_2 = \left( \frac{1}{N} \sum_{x,y} |\rho(x,y) - \rho^{exact}(x,y)|^2 \right)^{1/2}$$

and

$$\|\delta\rho\|_\infty = \max_{(x,y)} \{|\rho(x,y) - \rho^{exact}(x,y)|\},$$

where  $N$  is the number of grid points.

In order to stress the stability limit of the kinetic scheme, the lattice diffusivity can be chosen at a value ten times higher than the one used in the modified Lax-Wendroff scheme that is  $D_{LB}^* = 2.5$  and is  $D_{MLW}^* = 0.25$  (first row of Table 2.2), so that a corresponding ten-fold larger time step can be used in the kinetic scheme, at a given value of the physical diffusion coefficient ( $D = 1$ ). It should be noted that  $D^* = 2.5$  is beyond the critical value for the MLW method, as indicated by the empty entries in the MLW columns. The numerical results show satisfactory agreement with the analytical solution, with a fast decay in the numerical error with the time step, followed by a saturation when the amplitude falls below approximately  $10^{-5}$ . Timing data indicate that the kinetic LB scheme can compute significantly faster than MLW.

It is also important to assess the non-isotropy error associated

**Table 2.4:** Isotropy error for the MLW, LB and LBGK method,  $\lambda_3 = 1$ 

$\vec{u}$	$D_{theor}^*$	$Pe$	$D^*$ - measured value			
			<i>MLW</i>	<i>MRLK</i>	<i>SRLK - 4</i>	<i>SRLK - 9</i>
(0.2, 0.2)	0.20	1.41	0.200	0.200	0.186	0.200
(0.2, 0.2)	2.00	0.141	-	2.00	1.82	2.000
(0.1, 0.1)	0.20	1.41	0.200	0.200	0.198	0.200
(0.2, 0.2)	2.00	0.141	-	2.00	1.97	2.000

with the single-time relaxation scheme, as opposed to the present matrix formulation. These are shown in Table 2.4.

Table 2.4 shows that according to the expression (2.22), the isotropy error of the 4-speed single-relaxation model scheme is of the order  $Ma^2$ . It is worth noting that by adding four populations moving along the next-nearest neighbor (diagonal) connections, plus one population of rest particles, the LBGK scheme (see column LBGK-9, which stands for LBGK with nine populations) does in fact recover isotropy. However, this recovery comes at the expense of a factor  $9/4$  in the number of variables. In addition, since the diffusivity is fixed by the single relaxation parameter,  $\omega$ , it is clear that the 9-speed LBGK scheme cannot deal with genuinely anisotropic problems.

### Advection-Diffusion

Next we test the kinetic LB scheme for the case of diffusion and advection in a prescribed flow configuration.

We have simulated the standard Taylor-Aris dispersion problem at various global Peclet numbers,  $Pe = U_c L/D$ ,  $U_c$  being the centerline speed of the parabolic flow profile, and checked against the

**Table 2.5:** Taylor-Aris dispersion. The width of the channel is 48.

$Pe_c$	$D^*$	$U_c^*$	$D_L/D - 1$	$\frac{Pe^2}{470}$	Error, %
0.1	0.25	0.025	0.0486	0.0490	0.8
0.5	0.125	0.0625	1.221	1.226	0.3
1.0	0.25	0.25	4.89	4.90	0.2
5	0.05	0.25	121.5	122.6	0.9
10	0.05	0.5	487.5	490.2	0.6

analytical expression for the longitudinal dispersion coefficient:

$$D_L = D \left( 1 + \frac{Pe^2}{470} \right).$$

The initial conditions are Gaussian, with width  $\sigma_x = 5$  and  $\sigma_y = 50$ . The time-span of the simulations ranges from 2000 to 10000 time steps depending on the Peclet number. The results, for channels of width 48 lattice units and lengths ranging from 500 to 2000, are reported in Table 2.5.

Again, satisfactory agreement with analytical results is observed up to  $Pe_c \sim 10$ , which is fairly adequate for most practical applications. In order to test isotropy issues, we consider the case of a genuinely 2D flow,  $u_x^* = 0.2$  and  $u_y^* = 0.1$ , in a free (periodic) domain of size  $350 \times 250$ . The other parameters of the simulation are,  $\sigma_0 = 7.05$ ,  $D_{LB}^* = D_{MLW}^* = 0.02$ , corresponding to a cell-Peclet  $Pe_c = 11.2$ ,

In Fig. 2.1 plots of the density are shown at time  $t = 0$  and  $t = 1100$  for both LB and MLW methods. As expected, numerical data (see white arrows) follow the exact expression  $\langle \vec{r}(t) \rangle = \vec{r}_0 + \vec{u}t$ , where the brackets stand for integration of the density distribution over the flow domain.

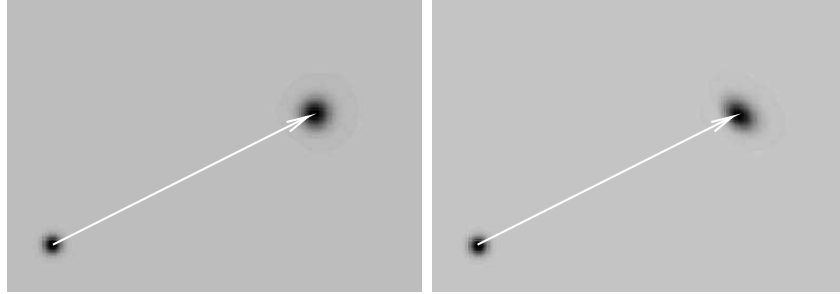


**Figure 2.1:** Plots of the density distribution at  $t = 0$  and  $t = 1100$  (arrow tail and head respectively) for the present LB (left) and MLW (right).

From Fig. 2.1 it is apparent that while the MLW results show visible deviations from isotropy, the present matrix LB method proves nearly free of spurious directional effects.

Quantitative analysis of contour lines in the form  $r = r(\theta)$  at  $\rho = \frac{1}{e}\rho_{\max}$ , delivers a non-isotropy factor  $\frac{\rho_{\max}}{\rho_{\min}} = 1.74$  for MLW and  $\frac{\rho_{\max}}{\rho_{\min}} = 1.02$  for LB (clearly, for the isotropic case  $\rho_{\max}/\rho_{\min} = 1$ ).

### Adaptive time stepping (ATS)

Some simulations of pure diffusion and advection-diffusion are provided in order to test the adaptive time stepping. In these tests, diffusion from initial distribution is considered again.

The evolution of the time step and the diabatic parameter  $\epsilon_{\min}$  with time is shown in Fig. 2.2. The change of the time step happens when the value of  $\epsilon$  approaches that of  $\epsilon_{\min}$ . It is seen that every jump in the time step is followed by a jump in  $\epsilon$ . Comparison between simulations with different  $\alpha_{dt}$  indicates that the heights of both jumps correlate. Thus, small values of  $\alpha_{dt}$  allow one to control the numerical error better, and to keep  $\epsilon$  in the range between  $\epsilon_{\max}$  and  $\epsilon_{\min}$  values. This case will be demonstrated in the next chapter.

**Table 2.6:** Diffusion tests with adaptive time stepping.  $D = 1$ .

$t_{max}$	Size	$\delta_t$	$\epsilon_{min}$	$\alpha_{dt}$	$L_2$	$L_\infty$
100	$250 \times 250$	0.25 – 1.0	0.05	2	$4.452 \cdot 10^{-4}$	$5.627 \cdot 10^{-3}$
1000	$500 \times 500$	0.25 – 2.0	0.01	2	$2.524 \cdot 10^{-5}$	$2.416 \cdot 10^{-4}$
1000	$500 \times 500$	0.25 – 4.0	0.05	2	$2.154 \cdot 10^{-4}$	$2.139 \cdot 10^{-3}$
1000	$500 \times 500$	0.25 – 4.0	0.1	2	$3.229 \cdot 10^{-4}$	$3.159 \cdot 10^{-3}$
1000	$500 \times 500$	0.25 – 2.71	0.05	1.1	$8.452 \cdot 10^{-5}$	$8.365 \cdot 10^{-4}$
1000	$500 \times 500$	0.25 – 2.85	0.05	1.5	$1.222 \cdot 10^{-4}$	$1.211 \cdot 10^{-3}$

Since in the example the flux decreases during the evolution,  $\epsilon$  decreases, as well. In other words, the time step increases with time. There are no limitations for the time step in the case without advection, see Table 2.6. Again, in the case with advection, the time step is limited by the Mach number.

A series of simulations is provided in order to test the relation between the *diabatic* parameter and numerical error. The relation between  $\epsilon_{min}$  and numerical error is shown in Table 2.6 and also can be seen in Fig. 2.3.

The same simulation is made for the three-dimensional case. In Table 2.7 some results are shown. The behavior of the adapting procedure is similar to the 2D case.

Further applications of ATS technique are discussed in Section 3.3.1.

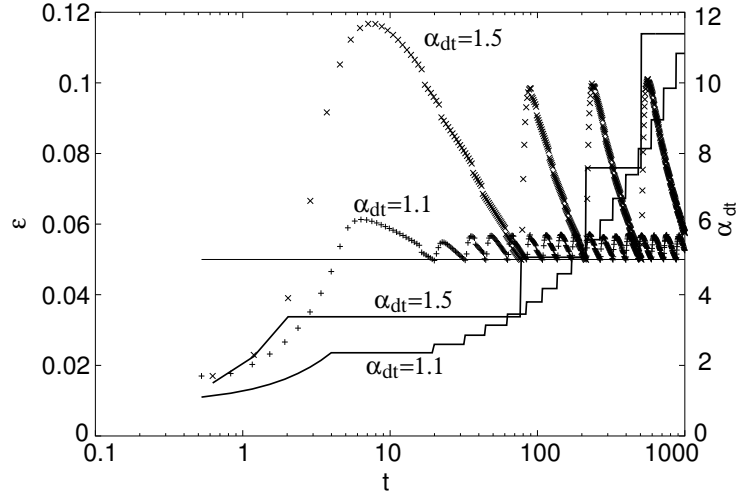


**Figure 2.2:** Evolution of time step and  $\epsilon$ . Points correspond to  $\epsilon$  and two line-plots represent the time step.  $D = 1$ ,  $t_{max} = 1000$ ,  $\lambda_3 = 1$ ,  $\epsilon_{min} = 0.05$ ,  $500 \times 500$ .

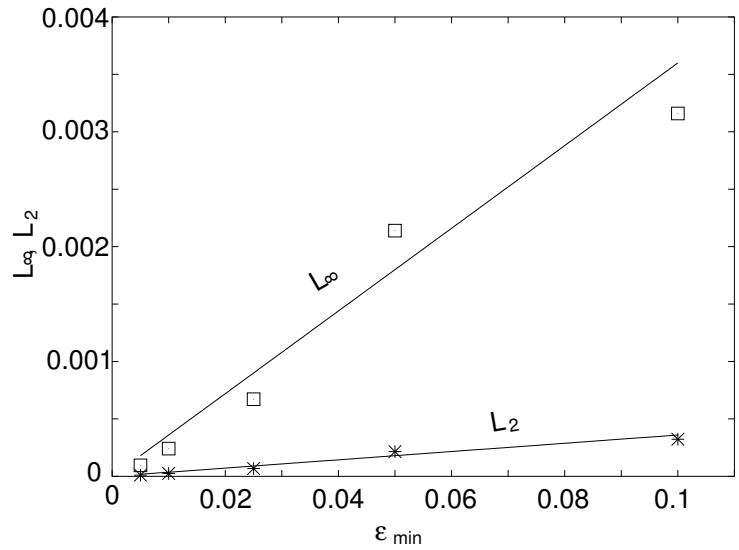


**Figure 2.3:** Dependence of the numerical error on  $\epsilon_{min}$ .  $D = 1$ ,  $t_{max} = 1000$ ,  $\lambda_3 = 1$ ,  $500 \times 500$ .



**Table 2.7:** Diffusion tests with adaptive time stepping in the 3D case.  $D = 1$ ,  $200 \times 200 \times 200$ ,  $t=100$

$t_{max}$	$\delta_t$	$\epsilon_{min}$	$\alpha_{dt}$	$L_2$	$L_\infty$
$t = 100$	0.25 – 0.589487	0.05	1.1	$3.415 \cdot 10^{-6}$	$1.221 \cdot 10^{-4}$
$t = 100$	0.25 – 0.84375	0.05	1.5	$4.608 \cdot 10^{-6}$	$1.601 \cdot 10^{-4}$
$t = 100$	0.25 – 2.0	0.05	2.0	$9.852 \cdot 10^{-6}$	$3.818 \cdot 10^{-4}$
$t = 300$	0.25 – 1.52898	0.1	1.1	$6.285 \cdot 10^{-6}$	$1.162 \cdot 10^{-4}$

# Chapter 3

## Phase-field models

Phase-field models have emerged nowadays as a widely used method to calculate the liquid-solid phase transitions on scales where Gibbs-Thompson and kinetic effects are important. Phase-field models have been successfully used for calculating the dendritic growth in the 2D and 3D cases, in the absence of liquid convection (e.g. [45, 26]). More recently, the influence of forced flow has been investigated [35, 62]. Beyond solidification in pure materials, the phase-field method has been applied to solidification in alloys, namely: the crystallization in binary[13, 69], eutectic[25], peritectic[41] and ternary alloys[32].

Phase-field models have been derived from a free energy (isothermal formulation, see e.g. [10, 38]) or an entropy functional (see e.g. [44, 52]) for the liquid-solid system. All of the listed models treat the Gibbs-Thompson and kinetic effects in similar ways. The surface tension part of the model leads to a numerical instability under certain conditions; computations with zero surface tension are impossible to realize in the frame of this model. The proposed modified phase-field model solves this problem. Its behavior

is tested in the case of solidification in pure materials.

### 3.1 The classic phase-field model

The crystallization in pure materials is described by the movement of the interface and by the temperature field. This system is modeled by the so-called Stefan problem. A system consists of two phases, *solid* and *liquid*. They are separated by a sharp interface,  $\Upsilon$ , which moves according to the local conditions. These two phases are described using different material parameters, e.g. heat capacities  $c_{ps}$ ,  $c_{pl}$  and heat conductivities  $K_s$ ,  $K_l$ , where indices  $s$  and  $l$  stand for *solid* and *liquid*, respectively. The phase-transition is defined through the melting-point temperature  $T_m$  and latent heat  $L$ . The classic sharp-interface model of solidification in a pure material may be written as:

$$c_{ps} \frac{\partial T_s}{\partial t} = \nabla[K_s \nabla T_s], \quad (3.1)$$

$$c_{pl} \frac{\partial T_l}{\partial t} = \nabla[K_l \nabla T_l], \quad (3.2)$$

$$LV = K_s \frac{\partial T_s}{\partial n} \Big|_{x \in \Upsilon} - K_l \frac{\partial T_l}{\partial n} \Big|_{x \in \Upsilon}, \quad (3.3)$$

$$T_s \Big|_{x \in \Upsilon} = T_l \Big|_{x \in \Upsilon} = T_m - V/\mu - \Gamma \kappa, \quad (3.4)$$

where  $T_s$ ,  $T_l$  are temperature fields in solid and liquid phases, respectively, and  $V$  is a local growth velocity.  $\mu$  and  $\Gamma$  are kinetic and Gibbs-Thomson coefficients, respectively.  $\kappa$  is the curvature of the interface  $\Upsilon$ .  $\vec{n}$  is a unit vector normal to  $\Upsilon$  oriented from the *solid* to the *liquid* phase. The first two equations describe heat transport in solids and liquids. Eq. 3.3 defines heat transport through the interface and the release of the latent heat during solidification. The

last equation governs the movement of the interface, taking into account the kinetic and Gibbs-Thomson effect.

In the phase-field model, no sharp interface exists between the solid and liquid phases, but the state of matter is characterized by a continuous order parameter,  $\phi$ .  $\phi$  is defined as 0 in the liquid phase (melt) and 1 in the solid phase (crystal). The standard form of phase-field equations couples a thermal field,  $T$ , to the order parameter field:

$$\tau \frac{\partial \phi}{\partial t} = \xi^2 \Delta \phi - g_\phi + \lambda p_\phi (T - T_m), \quad (3.5)$$

$$c_p \frac{\partial T}{\partial t} = K_0 \Delta T + L h_\phi \frac{\partial \phi}{\partial t}, \quad (3.6)$$

where  $\tau$ ,  $\lambda$  and  $\xi$  are phase-field parameters.

$$g_\phi \equiv \frac{\partial g(\phi)}{\partial \phi}, \quad p_\phi \equiv \frac{\partial p(\phi)}{\partial \phi}, \quad h_\phi \equiv \frac{\partial h(\phi)}{\partial \phi},$$

where  $g(\phi)$ ,  $p(\phi)$  and  $h(\phi)$  are standard functions for the phase-field model. Please note that in Eqs. (3.5) and (3.6), heat properties of both phases are supposed to be identical,  $c_{ps} = c_{pl} = c_p$ ,  $K_s = K_l = K_0$ . It is generally sufficient to require that  $g(\phi)$  has the shape of a double-well potential. It has two minima in 0 and 1, which correspond to the stable phases. This property prescribes a metastable-phase for all other values of  $\phi$ . The simplest choice for  $g(\phi)$  that has been traditionally used is

$$g(\phi) \equiv \phi^2(1 - \phi)^2. \quad (3.7)$$

The term  $p(\phi)$  is a monotone increasing function in the interval  $[0, 1]$  and takes values 0 and 1 on the left and right boundary, respectively. It is responsible for coupling between undercooling and  $\phi$ . Usually it has a polynomial form:

$$p(\phi) = 30 \left( \frac{\phi^3}{3} - \frac{\phi^4}{2} + \frac{\phi^5}{5} \right). \quad (3.8)$$

This form is chosen for stability reasons. The next phase-field function  $h(\phi)$  has the same properties as  $p(\phi)$ . There is some freedom in the choosing of this function. The comparison between different forms has been made by A. Karma and W. Rappel in [26] and by Y. Kim et al. in [31]. The conclusions of these works are that different models yield equal numerical results. This statement allows us to choose the  $h(\phi) = \phi$ .

In the phase-field model the interface between solid and liquid is defined as isoline  $\phi = 0.5$ . The phase-field equations (3.5) and (3.6) should reproduce the sharp interface equations (3.1)-(3.4). The last statement defines phase-field parameters  $\tau$ ,  $\xi$  and  $\lambda$  through the physical properties. Traditionally, these parameters are related through the sharp interface limit[11]. Recently, Karma and Rappel [26] presented a different asymptotic analysis performed in powers of the ratio of the interface width to the diffusion length. It requires domination of the two first terms in Eq.(3.5) over the undercooling term. The resulting expression is:

$$\mu^{-1} = a_1 \frac{\tau}{\lambda \xi} - a_2 \frac{\xi L}{c_p D_T}, \quad d_0 = a_1 \frac{\xi c_p}{L \lambda}, \quad (3.9)$$

where  $a_1$  and  $a_2$  depend on the functions  $p(\phi)$  and  $h(\phi)$  in Eqs.(3.6), (3.5). They are defined through the so called solvability integrals [26]:

$$a_1 = I_I / J_I, \quad a_2 = \frac{K_I + J_I F_I}{2I_I},$$

where

$$\begin{aligned} I_I &\equiv \int_{-\infty}^{\infty} (\partial \phi_0)^2 d\eta, \\ J_I &\equiv - \int_{-\infty}^{\infty} \partial \phi_0 p_\phi^0 d\eta, \\ K_I &\equiv \int_{-\infty}^{\infty} \partial \phi_0 p_\phi^0(\eta) \int_0^\eta h^0 d\eta'. \end{aligned}$$

In this case, the constants  $a_1$  and  $a_2$  take the following values:

$$a_1 = \frac{1}{3\sqrt{2}}, \quad a_2 = 0.3519.$$

The term with undercooling in Eq. (3.5) should be small in comparison with the two other terms, in other words, the system is in a quasi-stationary state. The one dimension phase-field profile can then be extracted as a zero order solution of the perturbation theory:

$$\phi = \frac{1}{2} \left( 1 + \tanh \frac{x}{\sqrt{2}\xi} \right). \quad (3.10)$$

The width of transition region,  $w_\phi$ , is introduced as the distance between points, which corresponds to  $\phi = 0.05$  and  $\phi = 0.95$ . The obtained solution gives  $w_\phi \approx \frac{6}{\sqrt{2}}\xi$ .

The phase field equations (3.5) and (3.6) can be obtained in a thermodynamically consistent way, see Appendix A. Historically, the phase-field equation (3.5) was obtained from the free-energy function [10, 11]. The model was applicable to isothermal phase-transitions. The Eq.(3.6) was artificially added (not in the frame of thermodynamics). The thermodynamically consistent derivative of the non-isothermal phase-field model was proposed later on, see [44]. The thermodynamical consistency requires  $h(\phi) = p(\phi)$ . As it was mentioned the simulation results are equal for the cases with  $h(\phi) = p(\phi)$  and  $h(\phi) = \phi$ , see [26, 31].

Additionally, we would like to rewrite the phase-field equations using slightly different notations. These notations will be called “thermodynamically-consistent”:

$$\begin{aligned} \tau_T \frac{\partial \phi}{\partial t} &= \xi_S^2 \Delta \phi - W g_\phi + \frac{L}{T_m^2} p_\phi (T - T_m), \\ \frac{\partial T}{\partial t} &= D_T \Delta T + \frac{L}{c_p} h_\phi \frac{\partial \phi}{\partial t}. \end{aligned}$$

The coefficients in this equation are related to the physical parameters as follows:

$$\mu^{-1} = a_1 \frac{\tau_T \sqrt{W} T_m^2}{L \xi_S} - a_2 \frac{\xi_S L}{c_p D_T \sqrt{W}}, \quad d_0 = a_1 \frac{T_m^2 \xi_S c_p \sqrt{W}}{L^2}. \quad (3.11)$$

The expression for the width of the transition region takes the form  $w_\phi \approx \frac{6\xi_S}{\sqrt{2W}}$ .

## 3.2 The modified phase-field model

The previous analysis has been made under the so called quasi-stationary assumption. The term with undercooling, see Eq.(3.5), is assumed to be small in comparison with the other two terms. This supposition plays a central role in the asymptotic analysis for a thin interface limit, however, this assumption is not always fulfilled. Fig. 3.1 shows the result of a 1D simulation where this assumption is shown to be incorrect. The plot clearly shows a deviation from the stationary solution. This deviation can be seen in the increase in the width of the transition region as compared to that which was expected. We propose here a method to remove this effect. The price for this solution, is some deviation from the thermodynamic roots of the phase-field method.

The following analysis is made for the 3D case and can be easily applied to the 2D case. The equation (3.5) contains the Laplacian, which is split into two parts:

$$\tau \frac{\partial \phi}{\partial t} = \xi^2 (n_\alpha n_\beta \nabla_\alpha \nabla_\beta \phi + (\Delta \phi - n_\alpha n_\beta \nabla_\alpha \nabla_\beta \phi)) - g_\phi + \lambda p_\phi (T - T_m). \quad (3.12)$$

The term  $n_\alpha n_\beta \nabla_\alpha \nabla_\beta \phi$  corresponds to the second derivative of the phase-field along the normal to an isosurface. The term  $(\Delta \phi -$

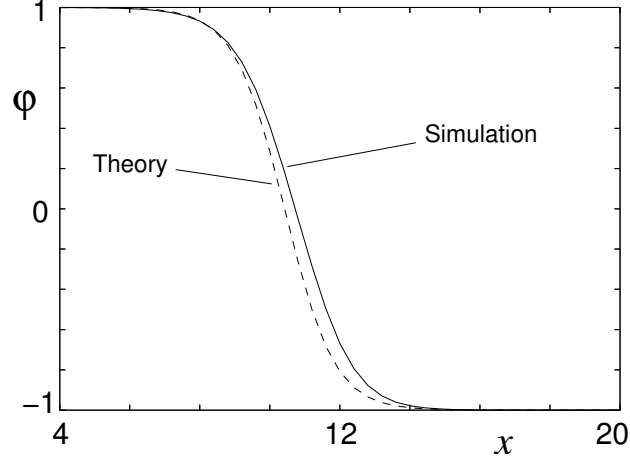


**Figure 3.1:** 1D profile of the phase-field.  $St = 0.25$ ,  $D_T = 20$  l.u.,  $t = 2000$  l.u.,  $\xi = 1$  l.u.,  $\tau = 1$  l.u.,  $L/c_p = 1$  l.u.,  $\lambda = 29.9$  l.u.

$n_\alpha n_\beta \nabla_\alpha \nabla_\beta \phi$ ) corresponds to the curvature of an isosurface which contains a current point, see Appendix C. There are two properties of the phase-field, which allow us to turn to a 1D equation, where the phase-field changes in a thin region and isolines are assumed to be parallel.<sup>1</sup> Eq.(3.12) turns to the following 1D equation:

$$\tau \frac{\partial \phi}{\partial t} = \xi^2 \phi'' + \xi^2 \kappa \phi' - g_\phi + \lambda p_\phi (T - T_m), \quad (3.13)$$

where  $\kappa$  is local curvature. Clearly,  $\xi^2$  has two functions. It is simultaneously responsible for the transition region and for the Gibbs-Thomson effect. The first role is actually the numerical parameter of the current model. As was mentioned in the previous section, the first two terms in Eq.(3.5) should be larger than the third. In this situation, when the Gibbs-Thomson effect is small in comparison with the kinetic effects, the  $\xi$  also has a small value, which sometimes leads to an instability of the transition region.

<sup>1</sup>This assumption is true if curvature radius is large in comparison with the width of the transition region.



Our idea is to divide the two functions of  $\xi$  between the two variables  $\xi_{\parallel}$  and  $\xi_{\perp}$ :

$$\tau \frac{\partial \phi}{\partial t} = \xi_{\perp}^2 \phi'' + \xi_{\parallel}^2 \kappa \phi' - g_{\phi} + \lambda p_{\phi} (T - T_m). \quad (3.14)$$

This separation permits the maintenance of high stability of the diffusive interface, despite surface tension being small, or even zero.

The described idea allows one to formulate the modified phase-field equation:

$$\tau \frac{\partial \phi}{\partial t} = \Xi_{\alpha\beta} \nabla_{\alpha} \nabla_{\beta} \phi - g_{\phi} + \lambda p_{\phi} Q(T), \quad (3.15)$$

where

$$\Xi_{\alpha\beta} \equiv \left( (\xi_{\perp}^2 - \xi_{\parallel}^2) n_{\alpha} n_{\beta} + \xi_{\parallel}^2 \delta_{\alpha\beta} \right).$$

An analysis procedure such as that in [26], gives the following relationship between modified phase-field parameters and the physical variables:

$$\mu^{-1} = a_1 \frac{\tau}{\lambda \xi_{\perp}} - a_2 \frac{\xi_{\perp} L}{c_p D_T}, \quad d_0 = a_1 \frac{\xi_{\perp} c_p}{L \lambda} \gamma_{\xi}^2, \quad w_{\phi} \approx \frac{6 \xi_{\perp}}{\sqrt{2W}} \quad (3.16)$$

where  $\gamma_{\xi} \equiv \frac{\xi_{\parallel}}{\xi_{\perp}}$ .

The discussed model plays a crucial role in our simulations of binary alloys, see Chapter 5.

### 3.3 Numerical implementation

The peculiarities of the numerical implementation of the phase-field model can be considered in the example of an isotropic case. The focus is the modelling of the heat transport by the LK scheme.

A simple explicit scheme for the phase-field and temperature equation is:

$$d\phi = \frac{\xi^2 \delta_t}{\tau} \bar{\Delta} \phi(t) - \delta_t g_\phi(t) - \delta_t \lambda p_\phi(t) \tilde{T}(t), \quad (3.17)$$

$$dT = \delta_t D_T \bar{\Delta} T + \frac{L}{c_p} h_\phi(t) d\phi, \quad (3.18)$$

where  $d\phi \equiv \phi(t+\delta_t) - \phi(t)$  and  $dT \equiv T(t+\delta_t) - T(t)$ .  $\bar{\Delta}$  is the discretized Laplacian. This scheme, due to the Laplacian, has stability restrictions. Namely the Courant conditions for both equations are:

$$\frac{\xi^2 \delta_t}{\tau \delta_x^2} < \frac{1}{4}, \quad D_T \frac{\delta_t}{\delta_x^2} < \frac{1}{4}. \quad (3.19)$$

These conditions correspond to the 5-point stencil for the Laplacian. The stability conditions make significant restrictions on the value of the time step. It can be solved by applying the proposed LK scheme for heat transport. Thus, the Eq.(2.8) is solved, instead of Eq.(3.18). The latent heat production in the MRLK method can be simulated by inserting the corresponding term in the equation (2.8):

$$f_i(\vec{r} + \delta_x \vec{a}_i, t + \delta_t) - f_i(\vec{r}, t) = \sum_j \Omega_{ij} (f_j^{eq}(\vec{r}, t) - f_j(\vec{r}, t)) + w_i \frac{L}{c_p} h_\phi(t) d\phi. \quad (3.20)$$

The latent heat term often leads to instability in a case with large time steps. This effect is a combination of serial solidification and melting processes in the transition region. These serial processes are caused by excessive latent heat production/consumption which is caused by the explicit time integration of the phase-field equation. This instability can be removed by using a semi-implicit scheme instead of (3.17):

$$d\phi = \frac{\xi^2 \delta_t}{\tau} \bar{\Delta} \phi(t) - \delta_t g_\phi(t) + \delta_t \lambda p_\phi(t) \left( \tilde{T}(t) + \frac{L}{c_p} h_\phi(t) d\phi \right).$$

This equation can be reformulated in the explicit form:

$$d\phi = \frac{\frac{\xi^2 \delta_t}{\tau} \bar{\Delta} \phi(t) - \delta_t g_\phi(t) + \delta_t \lambda p_\phi(t) \tilde{T}(t)}{1 + \lambda \frac{L}{c_p} h_\phi(t) p_\phi(t)}. \quad (3.21)$$

The adaptive time stepping procedure, discussed in Section 2.2.3, is implemented in the program. After implementation of this procedure, the developed numerical method becomes a fine tool for simulation of pattern formations processes in such systems.

Let us turn back to the phase-field equation. The MPF equation contains the second order spatial derivatives. These derivatives are discretized with the central finite-difference method. The special scheme is applied in order to reduce grid anisotropy. This scheme uses a 9-point template in the 2D case and a 19-point template for the 3D case. The expressions for corresponding derivatives are listed in Appendix D.2.

The locality of both numerical methods makes them very efficient for parallelization. The 3D model is parallelized for Beowulf-Clusters[3]. The data exchange is realized with MPI: Message Passing Interface[18]. The (rectangular) computational domain is divided into subdomains for each processor. Every processor requires the boundary values from the previous time step for computation of the next one. These boundary values come from the corresponding neighbor nodes. The nodes communicate through a common network.

### 3.3.1 Numerical tests

It is necessary to verify the proposed MPF model as well as the numerical procedure. The simulation of dendritic growth is a stan-

dard verification tool in this field.

The evolution of a small nucleus placed in an undercooled melt is simulated. The form of the nucleus changes from round to dendritic. This shape depends on conditions and anisotropy in surface tension and the kinetic coefficient. After some time the growing dendritic tip achieves its stationary state, which is determined by the growth velocity and the tip radius. Here we deal with anisotropy in surface tension,  $\gamma = \gamma_0\alpha(\vec{n})$ . The so called four-fold symmetry form is taken:

$$\alpha(\vec{n}) = 1 - 3\epsilon_4 + 4\epsilon_4 \frac{(\nabla_x\phi)^4 + (\nabla_y\phi)^4}{|\vec{\nabla}\phi|^4}, \quad (3.22)$$

or it is rewritten in terms of the orientation angle:

$$\alpha(\theta) = 1 + \epsilon_4 \cos 4\theta. \quad (3.23)$$

Here  $\theta$  is the angle between the interface and  $x$ -axis.  $\epsilon_4$  is the anisotropy parameter. The surface tension in the 3D case takes a similar form:

$$\alpha(\vec{n}) = 1 - 3\epsilon_4 + 4\epsilon_4 \frac{(\nabla_x\phi)^4 + (\nabla_y\phi)^4 + (\nabla_z\phi)^4}{|\vec{\nabla}\phi|^4}. \quad (3.24)$$

The corresponding expressions for capillary length  $d_0$  in the 2D and 3D cases are:

$$d_0(\vec{n}) = 1 - 3\epsilon_4 - 12\epsilon_4 \frac{(\nabla_x\phi)^4 + (\nabla_y\phi)^4 - 8(\nabla_x\phi)^2(\nabla_y\phi)^2}{|\vec{\nabla}\phi|^4},$$

$$d_0(\vec{n}) = 1 - 3\epsilon_4 - 12\epsilon_4 \left( \frac{(\nabla_x\phi)^4 + (\nabla_y\phi)^4 + (\nabla_z\phi)^4}{|\vec{\nabla}\phi|^4} - 4 \frac{(\nabla_x\phi)^2(\nabla_y\phi)^2 + (\nabla_x\phi)^2(\nabla_z\phi)^2 + (\nabla_y\phi)^2(\nabla_z\phi)^2}{|\vec{\nabla}\phi|^4} \right).$$

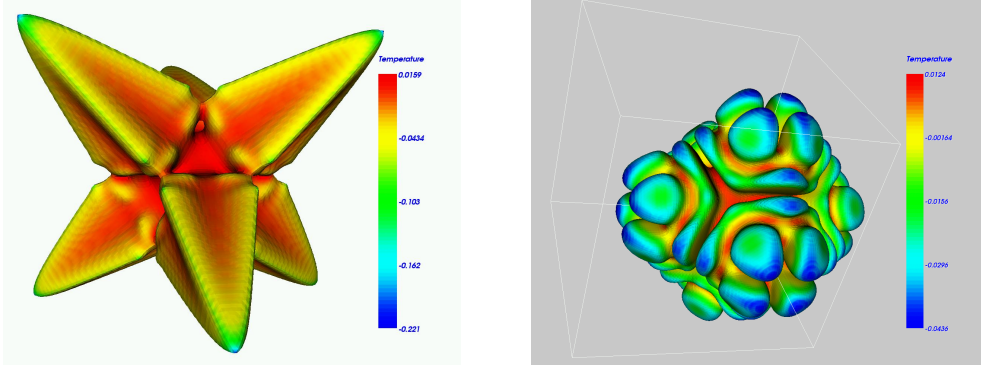


**Figure 3.2:** The 3D dendritic crystal. **Figure 3.3:** The 3D dendritic crystal.  $St = 0.45$ ,  $\delta_x = 0.8$ ,  $\epsilon_4^* = 0.05$ ,  $D = 4$ , size:  $250 \times 250 \times 250$   $St = 0.45$ ,  $\delta_x = 0.6$ ,  $\epsilon_4^* = 0.0081$ ,  $D = 12$ , size:  $250 \times 250 \times 250$

**Table 3.1:** Dendritic growth.  $\delta_x = 0.4$ ,  $\tau = 1$ ,

$St$	$\epsilon$	$\lambda$	$D$	$\frac{\sqrt{W}d_0}{\xi}$	$\tilde{v}$	$\tilde{v}$ - theory
0.55	0.05	4.70	2	0.277	0.0167	0.0170
0.55	0.05	7.05	3	0.185	0.0178	0.0170
0.45	0.05	9.40	4	0.139	0.00564	0.00545
0.30	0.05	23.5	10	0.055	0.000685	0.00068
0.55	0.02	4.70	2	0.277	0.00694	0.00685

$$\lambda = \frac{a_2 \tau D_T}{a_1 \xi_{\perp}^2 L}, \quad Ca = \frac{a_2 \xi_{\perp}^2 \gamma_{\xi}^2}{\tau D_T}. \quad (3.25)$$

An example of a 3D dendritic crystal is shown in Fig. 3.2. The color corresponds to the local temperature. The cold regions on the tips indicate the influence of the Gibbs-Thomson effect. Only one eighth part of the whole crystal was simulated.

The simulation results for 2D cases are collected in Table.3.1. The results show good agreement with the theoretical predictions [26].

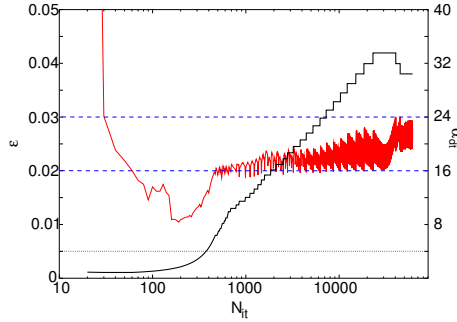


**Figure 3.4:** Value of the diabatic parameter and time step vs. time.  $St = 0.30$  see Table 3.1. Dashed lines correspond to the maximum and minimum allowed values of the *diabatic* parameter  $\epsilon$ . The ratio of the new to the old time step is fixed:  $\alpha_{dt} = 1.05$ .

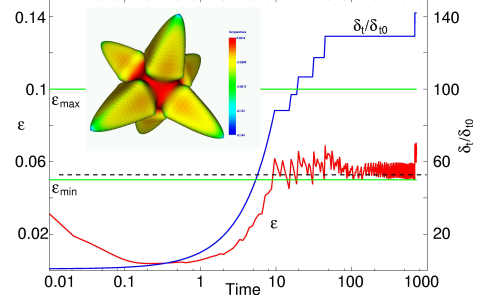


**Figure 3.5:** Time step and diabatic parameter for the 3D dendritic crystal. The dashed line corresponds to the maximal possible value of the time step for the central-forward finite difference method.  $St = 0.45$ ,  $\delta_x = 0.8$ ,  $\epsilon_4^* = 0.05$ ,  $D = 2$ , size:  $250 \times 250 \times 250$

The evolution of the time step and corresponding value of the *diabatic* parameter  $\epsilon$  are shown in Fig. 3.4. It is seen that in the initial stage the time step grows, but at some point it decreases and then stabilizes. During the period of decrease, the crystal shape changes from round to dendritic. The birth of dendrites is accompanied by an increase in the temperature gradient near the dendritic tips, which causes an increase in the local *diabatic* parameter.

The corresponding plot for the 3D case is shown in Fig. 3.5. The dashed line indicates the maximal possible value of the time step for the central-forward finite difference method. The two times larger time step may not seem like a very significant achievement, especially if we remember that it requires a six times larger memory and  $\sim 3$  time more floating point operations. However, the computation of the heat transport takes only  $\approx 15\%$  of the total

computation time, making an  $\approx 80\%$  increase in performance.

The dendritic crystal shown in Fig. 3.3 has a very small anisotropy. The exhibited morphology corresponds to the dublon type, according to the morphology diagram given by E. Brener et al. [9]. This case was computed with and without symmetry assumptions. The simulation results are equal.

### 3.3.2 Equilibrium shape

The next example is the calculation of the equilibrium shape of a crystal. Knowledge of the character of anisotropy in surface tension comes from analysis of the form of extremely slow growing crystals. A similar procedure is reproduced in the phase-field simulation. Solidification with small undercooling and slow growth kinetics is considered. Latent heat is not taken into account.

The anisotropy of the surface energy is taken again in the form of the four-fold symmetry, Eq.(3.22). The corresponding equilibrium shape can be described by the expression [54]:

$$\begin{aligned} x &= \alpha(\theta) \cos(\theta) - \alpha'(\theta) \sin(\theta), \\ y &= \alpha(\theta) \sin(\theta) + \alpha'(\theta) \cos(\theta). \end{aligned} \quad (3.26)$$

Simulations start from the round nucleus,  $r_0 = 70$  l.u. and they are made with the following physical parameters:

$$\Gamma = 0.69 \text{ l.u.}, \quad \mu = 0.090 \text{ l.u.} \quad (3.27)$$

The equilibrium form is achieved after some time, see Fig. 3.6. It is seen that the initial nucleus melts in some regions and grows in others.

A comparison of the phase-field simulation and the analytical solution is shown in Fig. 3.7. This result allows us to conclude that

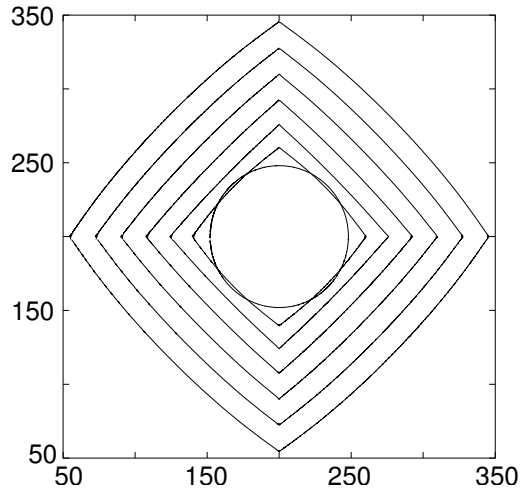


**Figure 3.6:** Evolution of a crystal with the anisotropy  $\epsilon = 0.2$ . Isolines correspond to the different time:  $t = 0, 2000, \dots, 12000$  l.u.

the proposed modification of the phase-field equation reproduces the anisotropy effects with high accuracy, even in the case of strong anisotropy.

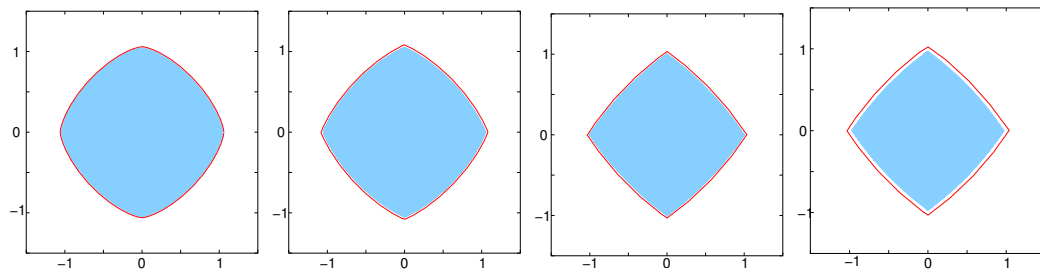


**Figure 3.7:** Equilibrium forms of crystals for different values of anisotropy:  $\epsilon = 0.05, 0.1, 0.2, 0.5$ . The analytical form is marked by a line and the phase-field simulation is plotted with a filled area.



## Chapter 4

# Phase-field models for binary alloys

The previous chapter demonstrates application of the phase-field model for simulation of the dendritic growth in a pure, undercooled melt. It has been extended to the model for solidification in binary alloys by Wheeler, Boettinger and McFadden [69], the WBM model. The WBM model that has been used widely [69, 12, 67, 34] is derived in a thermodynamically-consistent manner. In this model, any point within the interfacial region is assumed to be a mixture of a solid and a liquid, both with the same composition. The phase field parameters can be determined not only through the sharp interface limit condition, but also through the finite interface thickness condition [29]. It has been shown that the model can correctly reproduce the solute trapping phenomena at a high interface velocity [12, 29].

A careful study of the WBM model shows that there is limitation on the width of the transition region [29, 30]. The existence of this limitation pushed Kim, Kim and Suzuki to develop the so

called KKS model for binary alloys [30]. This model is derived in a thermodynamically-consistent manner, as well. The difference between the WBM and the KKS model is in the definition of the free energy density for the interfacial region.

Differential equations of the KKS model were solved by the finite difference method. The first attempts to simulate GeSi crystals demonstrated that stability restrictions of the FD method on the time step make simulation of the system impossible. Application of the MRLK scheme to the concentration equation allows one to increase the time step by 10-100 times, in comparison with the FD scheme.

This chapter has the following structure. In the first two sections, a short overview on the theory of phase transition in binary alloys is given. The two following sections contain overviews of the WBM and the KKS models and the numerical procedure for the solving of the phase-field equations is further considered. In the last section, we present an application of the developed technique to the NiCu alloy.

## **4.1 Thermodynamics and the sharp interface model**

### **4.1.1 Thermodynamics**

The considered system consists of two components,  $A$  and  $B$ , and two phases, liquid and solid, respectively. It is supposed that both components and phases have equal density, meaning that the thermodynamic potentials are only functions of temperature. Similar

to the procedure used in the phase-field model for pure material, we introduced: energy  $\mathcal{E}$  and free energy  $\mathcal{F}$  functions. The corresponding differentials are:

$$d\mathcal{E} = T_i dS, \quad d\mathcal{F} = -SdT, \quad (4.1)$$

where  $T$  and  $S$  are temperature and entropy, respectively. These equations can be divided by volume  $V$  and rewritten in terms of densities:

$$de = T_i ds, \quad df = -sdT, \quad (4.2)$$

where  $e$ ,  $f$  and  $s$  are the densities of the corresponding thermodynamic values  $\mathcal{E}$ ,  $\mathcal{F}$ ,  $S$ . The energy and the free energy density functions are related through the Legendre transformation:

$$f(T) = e - Ts(e). \quad (4.3)$$

The corresponding Legendre transformation for bulk values looks similar:

$$\mathcal{F} = \int_V e - Ts(e) dV = \mathcal{E} - TS$$

Eq. (4.3) gives the relation between  $e$  and  $f$ :

$$e = \frac{\partial(f/T)}{\partial(1/T)} \implies f = T \int_{T_m}^T e(T) d\left(\frac{1}{T}\right). \quad (4.4)$$

The energy densities of each component for different phases are defined as:

$$e_l = Tc_{pl}, \quad e_s = Tc_{ps} - L, \quad (4.5)$$

where  $c_p$  is the heat capacity of a substance and  $L$  is latent heat. The indices  $l$  and  $s$  indicate the liquid and solid phases. This is the simplest model, which takes into account latent heat production

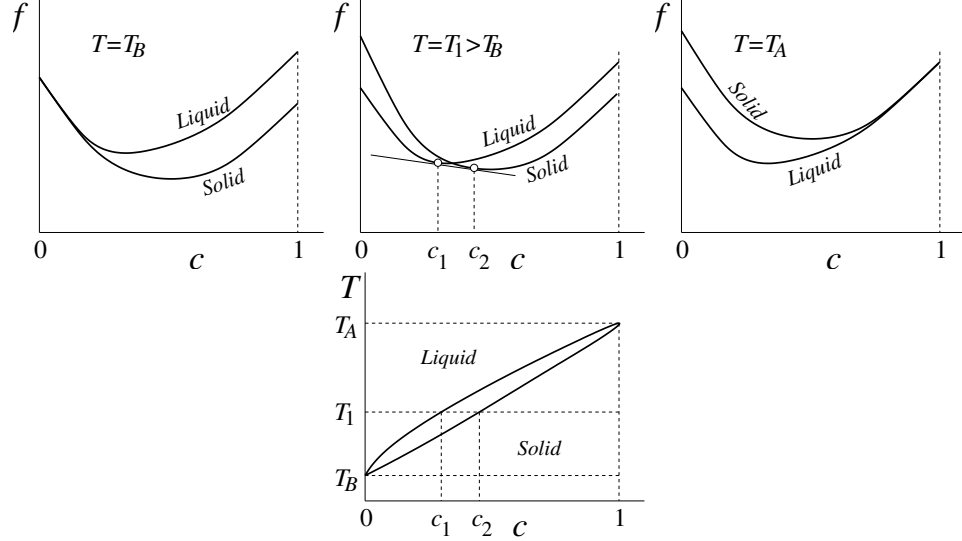


**Figure 4.1:** Illustrations for the common tangent method. Free energies of two phases are plotted vs. concentration for different values of temperature. The last plot shows the corresponding phase-diagram.

by phase transition. An expression for  $f$  is obtained as a result of substituting expressions (4.5) into Eq. (4.4):

$$f_l = c_{pl}T \ln \frac{T_m}{T}, \quad f_s = c_{ps}T \ln \frac{T_m}{T} - LTQ(T), \quad (4.6)$$

where  $Q(T) \equiv \frac{1}{T} - \frac{1}{T_m}$ . Expressions for the densities of the thermodynamic potentials can be constructed for the case of a mixture. The WBM model defines the free energy of the mixture as follows:

$$f = cf_A + \tilde{c}f_B - Ts_{mix}, \quad (4.7)$$

where  $\tilde{c} \equiv 1 - c$ ,  $s_{mix}$  is entropy of the mixture. In the case of an ideal mixture,  $s_{mix}$  takes the same form as for an ideal gas:

$$s_{mix} = RT(c \ln c + \tilde{c} \ln \tilde{c}).$$

The obtained free energy function should correspond to the phase diagram obtained in the experiment, see Fig. 5.2. The com-

mon tangent method is a standard tool used for calculation of the phase diagram from known free energy functions. This procedure is sketched in Fig. 4.1. Free energy functions for solid and liquid phases are:

$$f_l = c_p T \ln \frac{\overline{T_m}}{T} + \frac{RT}{V_m} (c \ln c + \tilde{c} \ln \tilde{c}), \quad (4.8)$$

$$f_s = c_p T \ln \frac{\overline{T_m}}{T} - T \overline{LQ(T)} + \frac{RT}{V_m} (c \ln c + \tilde{c} \ln \tilde{c}), \quad (4.9)$$

where  $\overline{(\text{expression})} \equiv c(\text{expression})_A + \tilde{c}(\text{expression})_B$ .

The conditions for the common tangent can be written in the following form:

$$\frac{\partial f_s(T, c_s^0)}{\partial c} = \frac{\partial f_l(T, c_l^0)}{\partial c}, \quad (4.10)$$

$$f_s(T, c_s^0) - \frac{\partial f_s(T, c_s^0)}{\partial c} c_s^0 = f_l(T, c_l^0) - \frac{\partial f_l(T, c_l^0)}{\partial c} c_l^0, \quad (4.11)$$

where  $c_s^0$  and  $c_l^0$  are the concentrations, which correspond to the solidus and liquidus curve, respectively. The first equation can be interpreted as equality of the chemical potentials of both phases. The second equation is equivalent to the requirement of zero undercooling. By using the definition of the chemical potential,  $\mu = \frac{\partial f}{\partial c}$ , the condition can be rewritten in the different form:

$$\mu_l(T, c_l^0) = \mu_s(T, c_s^0) = \frac{f_s(T, c_s^0) - f_l(T, c_l^0)}{c_s^0 - c_l^0}. \quad (4.12)$$

These equations are solved for the free energy functions given in Eqs.(4.8), (4.9). The solution describing solidus and liquidus curves has the form:

$$c_l^0 = \frac{\hat{k}_B - 1}{\hat{k}_B - \hat{k}_A} \quad c_s^0 = \hat{k}_A \frac{\hat{k}_B - 1}{\hat{k}_B - \hat{k}_A}, \quad (4.13)$$

where

$$\hat{k}_A \equiv e^{\frac{L_A^M Q_A(T) V_m}{R}}, \quad \hat{k}_B \equiv e^{\frac{L_B^M Q_B(T) V_m}{R}}. \quad (4.14)$$

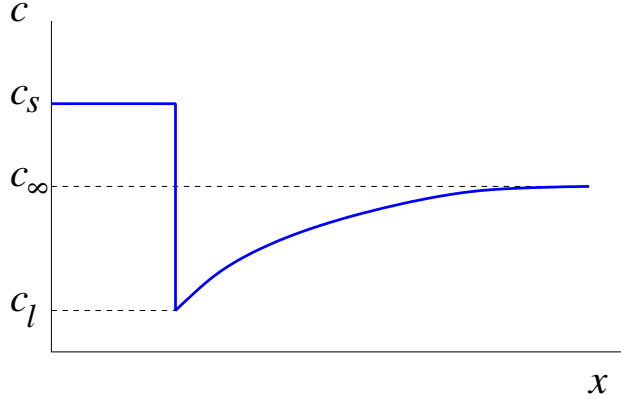


**Figure 4.2:** 1D concentration profile of a solution for a sharp interface model. Here, it is plotted for a case with flow.

$\hat{k}_A$  and  $\hat{k}_B$  are partition coefficients:

$$\hat{k}_A = \frac{c_s^0}{c_l^0}, \quad \hat{k}_B = \frac{1 - c_s^0}{1 - c_l^0}.$$

This expression takes a simpler form in a dilute alloy approximation:

$$c_l^0 = m_e (T - T_B), \quad c_s^0 = \hat{k}_A(T_B) m_e (T - T_B),$$

where  $m_e$  is the liquidus slope:

$$m_e = \frac{L_B^M Q'(T_B) V_m}{(1 - \hat{k}_A(T_B)) R}$$

### 4.1.2 Sharp interface model

The classical sharp interface model for isothermal solidification of an alloy is:

$$\frac{\partial c_s}{\partial t} = D_s \Delta c_s, \quad (4.15)$$

$$\frac{\partial c_l}{\partial t} = D_l \Delta c_l, \quad (4.16)$$

$$\mu_s = \mu_l \equiv \mu, \quad (4.17)$$

$$v = \beta^{-1} \left( (\mu^e - \mu) \frac{T(c_l^e - c_s^e)}{L} - \Gamma \kappa \right), \quad (4.18)$$

$$(c_l^i - c_s^i)V = D_s \frac{\partial c_s}{\partial n} - D_l \frac{\partial c_l}{\partial n}, \quad (4.19)$$

where  $D_s$  and  $D_l$  are the diffusivities of the solute in the solid and liquid phases, respectively,  $c_s^i$  and  $c_l^i$  are the compositions of the solid side and the liquid side at the interface,  $c_s^e$  and  $c_l^e$  are equilibrium values of compositions of the solid side and the liquid,  $\mu_e$  is the chemical potential in the thermodynamic equilibrium state.  $\mu_e = \frac{f_s(T, c_s) - f_l(T, c_l)}{c_s - c_l}$  is the equilibrium value of the chemical potential. The Eq. (4.18) introduces supersaturation:

$$\Theta \equiv (\mu^e - \mu) \frac{T(c_s^e - c_s^i)}{L}. \quad (4.20)$$

In this definition  $\Theta$  is measured in temperature units.

### 4.1.3 1D solutions

As mentioned earlier, there is a jump in the concentration value on the solidification front. This jump is described with the solute partition coefficient.

$$\hat{k} \equiv \frac{c_s}{c_l}.$$

This coefficient becomes equal to the phase diagram partition coefficient, (4.14), in the case of infinite kinetics. Typically, a 1D concentration profile has the form like that seen in Fig. 4.2. It is also possible to introduce the effective distribution coefficient  $k_\infty$ ,

$$k_\infty = \frac{c_s}{c_\infty}.$$

The value of the effective partition coefficient equals 1 in a system with pure diffusion. In the presence of flow, the effective partition

coefficient has a value different from 1. It is defined through the diffusion layer thickness,  $\delta_c$  (see pg. 15 in [61]):

$$k_\infty = \frac{\hat{k}}{\hat{k} + (1 - \hat{k}) \exp(-v_{gr}\delta_c/D)}. \quad (4.21)$$

## 4.2 Phase-field models for binary alloys

In this section thermodynamically consistent phase-field models for a system of two components, A and B, will be introduced. The model development procedure is similar to that used in the case of pure materials, see Appendix A.

### 4.2.1 Basic ideas

The system consists of two phases: solid and liquid. An order parameter,  $\phi$ , is introduced for the description of the phase transition. It defines the local state of the system. Zero value corresponds to the liquid phase (melt) and the value  $\phi = 1$ , to the solid phase (crystal). The phase-field parameter changes continuously between these two values, and in this way the interface is described. This fact should be reflected in the free energy  $\mathcal{F}$ :

$$\mathcal{F} = \int_V \left( f(\phi, c, T) + \frac{\xi_F^2}{2} |\nabla\phi|^2 \right) dV, \quad (4.22)$$

where  $f(\phi, c, T)$  is the free energy density function with the phase state  $\phi$ , and  $\xi_F$  is the coefficient responsible for surface energy. The free energy function is convenient for consideration of an isothermal model, while an entropy function is used for non-isothermal consideration. The expression for entropy is:

$$\mathcal{S} = \int_V \left( s(\phi, c, e) - \frac{\xi_S^2}{2} |\nabla\phi|^2 \right) dV, \quad (4.23)$$



where  $\xi_S^2 \equiv \xi_F^2/T$ . The expressions obtained for the thermodynamic functions allow us to construct evolution equations for the fields. The equations for  $\phi$ ,  $c$  and  $e$  are usually taken in the following form [22]:

$$\frac{\partial \phi}{\partial t} = M_\phi \frac{\delta \mathcal{S}}{\delta \phi}, \quad (4.24)$$

$$\frac{\partial e}{\partial t} = -\vec{\nabla} \cdot \left( M_e \vec{\nabla} \frac{\delta \mathcal{S}}{\delta e} \right), \quad (4.25)$$

$$\frac{\partial c}{\partial t} = -\vec{\nabla} \cdot \left( M_c \vec{\nabla} \frac{\delta \mathcal{S}}{\delta c} \right). \quad (4.26)$$

$M_\phi$ ,  $M_e, M_c$  are positive functions, which define evolution rate towards the equilibrium state. These equations uphold the energy and mass conservation laws as well as the second law of thermodynamics. These relations are reformulated in terms of the free energy density:

$$\frac{\partial \phi}{\partial t} = M_\phi \left( -\frac{1}{T} \frac{\partial f}{\partial \phi} + \xi_S^2 \Delta \phi \right), \quad (4.27)$$

$$\frac{\partial e}{\partial t} = -\vec{\nabla} \cdot \left( M_e \vec{\nabla} \frac{1}{T} \right), \quad (4.28)$$

$$\frac{\partial c}{\partial t} = \vec{\nabla} \cdot \left( M_c \vec{\nabla} \frac{1}{T} \frac{\partial f}{\partial c} \right). \quad (4.29)$$

### 4.2.2 The WBM phase-field model

Warren and Boettinger defined  $f$  as the free energy density for a two component system as follows:

$$f = cf_A + \tilde{c}f_B + f_{AB}, \quad (4.30)$$

where  $c$  and  $\tilde{c} = 1 - c$  are the concentrations of the components  $A$  and  $B$ , respectively.  $f_A$  and  $f_B$  are the free energy functions of the

pure components and  $f_{AB}$  is an additional term, which corresponds to a mixed state. In most cases the additional free energy can be expressed as:

$$f_{AB} = e_{AB} + \frac{RT}{V_m}(c \ln c + \tilde{c} \ln \tilde{c}), \quad (4.31)$$

where  $R$  is the gas constant, and  $V_m$  is the molar volume<sup>1</sup>. For ideal solutions,  $e_{AB} = 0$ . Let us write down once more the expressions for the free and internal energy density functions of a pure material  $A$ :

$$f_A = c_{pA}T \ln \frac{T_A}{T} - L_{Ap}(\phi)TQ_A(T) + TWg(\phi), \quad (4.32)$$

$$e_A = Tc_{pA} - L_{Ap}(\phi), \quad (4.33)$$

where  $T_A$ ,  $L_A$  are melting point temperature, latent heat of the component  $A$ . It is assumed that  $W$  is equal in both materials. It should be mentioned that the heat capacities of both components are independent of the phase-field<sup>2</sup>. Function  $Q$  was defined in the thermodynamically-consistent model for pure materials, Eq. (A.20). Note that it is not allowed to use the approximation because  $T \approx T_m$  does not hold.

By substituting the definition of  $f$ , Eq. (4.30), the evolution equation for concentration can be obtained:

$$\frac{\partial c}{\partial t} = \vec{\nabla} \cdot \left( M_c \vec{\nabla} \frac{f_{\Delta} + \frac{\partial f_{AB}}{\partial c}}{T} \right), \quad (4.34)$$

where  $f_{\Delta} \equiv f_A - f_B$ . The parameters  $\xi_A$  and  $\xi_B$  are assumed to be equal.

---

<sup>1</sup>In this model,  $V_m$  is assumed not to depend on concentration, temperature or phase-field.

<sup>2</sup>Thus, there is no jump of heat capacity during the phase transition in Si, and it is  $\sim 6\%$  for Ge.

### 4.2.3 Evolution equations

The free energy function can be now written in the explicit form:

$$f = c_p T \ln \frac{T_m}{T} - p(\phi) T \overline{LQ(T)} + Tg(\phi)W + \frac{RT}{V_m}(c \ln c + \tilde{c} \ln \tilde{c}). \quad (4.35)$$

The heat capacity is taken as equal for both components<sup>3</sup>. Substitution of this expression into Eq. (4.27) gives:

$$\tau \frac{\partial \phi}{\partial t} = \xi_S^2 \Delta \phi - W g_\phi + p_\phi \overline{LQ(T)}. \quad (4.36)$$

Here,  $M_\phi$  is taken as a constant,  $M_\phi = 1/\tau$ . As can be seen, this equation is linear with respect to  $c$ . The temperature and concentration equations are obtained, as well:

$$c_p \frac{\partial T}{\partial t} = \vec{\nabla} \cdot (K(\phi, c) \vec{\nabla} T) + \frac{\partial \phi}{\partial t} p_\phi \bar{L} + p(\phi) L_\Delta \frac{\partial c}{\partial t}, \quad (4.37)$$

$$\frac{\partial c}{\partial t} = \vec{\nabla} \cdot \left( M_c \vec{\nabla} \left( C \ln \frac{T_A}{T_B} - p(\phi) [LQ(T)]_\Delta + \frac{R}{V} \ln \frac{c}{\tilde{c}} \right) \right), \quad (4.38)$$

where  $[\text{expression}]_\Delta \equiv (\text{expression})_A - (\text{expression})_B$ . Comparison of the equation for the concentration with Fick's Law of diffusion gives us the expression for  $M_c$ :

$$M_c = D \frac{V_m}{R} c \tilde{c}, \quad (4.39)$$

where  $D$  is a diffusion coefficient. After substituting we have obtained:

$$\frac{\partial c}{\partial t} = \vec{\nabla} \cdot (D \vec{\nabla} c) - \frac{V_m}{R} D \vec{\nabla} \cdot (c \tilde{c} \vec{\nabla} p(\phi) [LQ(T)]_\Delta). \quad (4.40)$$

Equations (4.36) and (4.40) define the WBM phase-field model. The parameters appearing in the equations are related to the ma-

<sup>3</sup>The difference between heat capacities of Si and Ge is  $\sim 10\%$  for the temperature in the interval between the melting points of both materials.

terial parameters. The expressions for phase-field parameters, extracted from the sharp-interface limit, are written here [67]:

$$w = \frac{\xi_S}{a_1\sqrt{W}}, \quad \gamma = a_1 T_m \xi_S \sqrt{W}, \quad \mu^{-1} = a_1 \frac{\tau_T T_m^2 \sqrt{W}}{L \xi_S}, \quad (4.41)$$

where  $a_1$  was defined in Section 3.1 and  $T_m$  is the temperature on the crystal surface. The thin interface limit for this model is not known.

#### 4.2.4 Limitation of the WBM model

The WBM model has an artificial term, which can be interpreted as the surface energy term. It comes from the chemical energy in the transition region. The explicit form of this artificial part of surface the energy can be obtained from the stationary solution of the model.

The equations for the stationary case can be written in the form:

$$\xi_S^2 \Delta \phi - W g_\phi + p_\phi \overline{LQ(T)} = 0, \quad (4.42)$$

$$\nabla D \nabla c - [LQ(T)]_\Delta \frac{V_m}{R} \vec{\nabla} (Dc \tilde{c} p_\phi \vec{\nabla} \phi) = 0. \quad (4.43)$$

For an infinite 1D domain the boundary conditions are taken:

$$\nabla \phi|_{x=\pm\infty} = 0, \quad \phi|_{x=-\infty} = 0, \quad \phi|_{x=+\infty} = 1, \quad \nabla c|_{x=\pm\infty} = 0. \quad (4.44)$$

The corresponding stationary solution for  $c$  is:

$$c = \frac{K}{e^{Bp(\phi)} + K}, \quad B \equiv -\frac{V_m}{R} [LQ(T)]_\Delta, \quad (4.45)$$

where  $K$  is an integration constant. The order of the equation for  $\phi$  can be reduced:

$$\frac{\xi_S^2}{2} (\nabla \phi)^2 - W g(\phi) - P(\phi) = K_1,$$

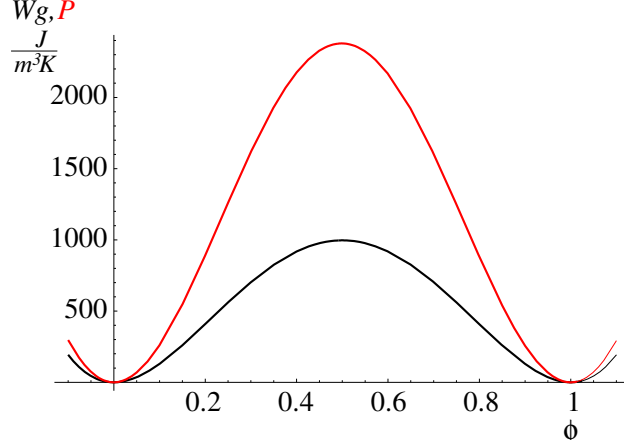


**Figure 4.3:** Both terms with double-well potential. Parameters are taken for NiCu alloy.

where

$$\begin{aligned} P(\phi) &\equiv -p(\phi)L_BQ_B - [LQ]_{\Delta} \int c(\phi)p_{\phi} d\phi \\ &= -p(\phi)L_BQ_B + \frac{RK}{V_m} \ln(e^{Bp(\phi)} + K). \end{aligned}$$

It follows from the boundary conditions (4.44) that

$$K = e^B \frac{c_s}{1 - c_s} \quad \text{and} \quad K_1 = -P(1).$$

Substituting the material parameters for NiCu in the Eq.(4.41) gives the plot for the term  $Wg(\phi)$  with double-well potential and the term  $P(\phi)$ . Both terms contain double-well potentials, see Fig.4.3. This exhibits that the WBM model has a strong non-physical effect related with wrong definition of the free energy in the transition region. This effect becomes stronger with increasing of width of the transition region. Therefore, it is impossible to apply it for simulation of GeSi cellular structure.

### 4.3 The KKS phase-field model

The isothermal variant of this model was first considered by Kim et al. [30]. In this model, the transition region is defined as a mixture of the solid and liquid phases with different concentrations but with the same chemical potentials. In the previous model, there were the same concentrations in mixed phases but different chemical potentials. The free energy function is constructed differently than in the WBM model, namely, as a mix of free energies of different phases. It takes the form:

$$f(c, \phi) = p(\phi)f_s(c_s) + \tilde{p}(\phi)f_l(c_l) + TWg(\phi), \quad (4.46)$$

where  $\tilde{p}(\phi) \equiv 1 - p(\phi)$ ,  $f_s$  and  $f_l$  are the free energy functions of the solid and liquid phases, respectively.  $c_s$  and  $c_l$  are concentrations in the solid and liquid phases. They are defined by the following equations:

$$c = p(\phi)c_s + \tilde{p}(\phi)c_l, \quad (4.47)$$

$$\frac{\partial f_s(c_s)}{\partial c_s} = \frac{\partial f_l(c_l)}{\partial c_l}. \quad (4.48)$$

The second equation is nothing more than the equality of the chemical potentials of both phases.

The evolution equations are the same as in the WBM model, (4.27) and (4.29). From the equations (4.47), (4.48) the expressions for the derivatives of  $c_s$  and  $c_l$  on  $c$  and  $\phi$  are obtained:

$$\frac{\partial c_l}{\partial c} = \frac{f_s''}{p(\phi)f_l'' + \tilde{p}(\phi)f_s''}, \quad \frac{\partial c_s}{\partial c} = \frac{f_l''}{p(\phi)f_l'' + \tilde{p}(\phi)f_s''}, \quad (4.49)$$

$$\frac{\partial c_l}{\partial \phi} = \frac{p_\phi[c_l - c_s]f_s''}{p(\phi)f_l'' + \tilde{p}(\phi)f_s''}, \quad \frac{\partial c_s}{\partial \phi} = \frac{p_\phi[c_l - c_s]f_l''}{p(\phi)f_l'' + \tilde{p}(\phi)f_s''}, \quad (4.50)$$

where prime denotes the derivative with respect to  $c$ . These expressions yield derivatives from the free energy (4.46):

$$\frac{\partial f}{\partial \phi} = TWg_\phi - \frac{L}{T}p_\phi\Theta, \quad \Theta \equiv \frac{T}{L}(f_l - f_s - (c_l - c_s)f_l'). \quad (4.51)$$

These expressions allow us to reformulate the governing equations (4.27) and (4.29):

$$\tau \frac{\partial \phi}{\partial t} = \xi_S^2 \Delta \phi - Wg_\phi + \frac{L}{T^2}p_\phi\Theta, \quad \tau \equiv 1/M_\phi, \quad (4.52)$$

$$\frac{\partial c}{\partial t} = \nabla \left( \frac{M_c}{T} f_l'' \left( \frac{\partial c_l}{\partial c} \vec{\nabla} c + \frac{\partial c_l}{\partial \phi} \vec{\nabla} \phi \right) \right). \quad (4.53)$$

Here,  $\Theta$  corresponds to a thermodynamic driving force for solidification (constitutional undercooling). By equating  $\Theta$  to zero the known equilibrium condition (4.12) is obtained. The last equation for concentration is obtained within the isothermal model. The non-isothermal model will be discussed later, see Section 4.3.1. This equation should reproduce Fick's Law. This requirement relates  $M_c$  to the diffusion coefficient:

$$M_c = DT \frac{p(\phi)f_l'' + \tilde{p}(\phi)f_s''}{f_s''f_l''}.$$

Substituting of expressions (4.49) and (4.50) in the last equation gives:

$$\frac{\partial c}{\partial t} = \nabla(D\nabla c) + \nabla(D[c_l - c_s]\nabla p(\phi)). \quad (4.54)$$

The governing equations are accomplished with Eqs. (4.47) and (4.48).

Similar to the previous model, the free energy functions for liquid and solid phases are taken in the form:

$$f_l = c_p T (\overline{\ln T_m} - \ln T) + \frac{RT}{V_m} (c \ln c + \tilde{c} \ln \tilde{c}), \quad (4.55)$$

$$f_s = c_p T (\overline{\ln T_m} - \ln T) - T \overline{LQ(T)} + \frac{RT}{V_m} (c \ln c + \tilde{c} \ln \tilde{c}). \quad (4.56)$$

These expressions give the solution of the Eqs. (4.47), (4.48), as a relation between  $(c_l, c_s)$  and  $c, \phi$ :

$$c_l = \frac{-\alpha + c + \tilde{p}(\phi) + \sqrt{D}}{2\tilde{p}(\phi)}, \quad c_s = \frac{\alpha + c - \tilde{p}(\phi) - \sqrt{D}}{2p(\phi)}, \quad (4.57)$$

$$D \equiv (\alpha + c - \tilde{p}(\phi))^2 - 4cp(\phi)\alpha,$$

where  $\alpha$  is related with the liquidus and solidus concentrations, defined in (4.14):

$$\alpha \equiv \frac{k_a}{k_a - k_b} = \frac{c_s^0(1 - c_l^0)}{c_s^0 - c_l^0}. \quad (4.58)$$

Substituting of  $f_l$  and  $f_s$  in the expression for  $\Theta$  Eq. (4.51) yields:

$$\Theta = \frac{T^2}{L} \left( L_B Q_B + \frac{R}{V} \ln \frac{1 - c_l}{1 - c_s} \right). \quad (4.59)$$

The relations between the phase-field parameters and the material parameters are the same as for the WBM model, see Eq. (4.41). The thin interface limit will be discussed later.

### 4.3.1 Non-isothermal case

The basic ideas for the construction of a non-isothermal model, are considered in Section 4.2.2. A similar procedure is applied for the KKS model.

Up to now we considered temperature an a constant field. Here we would like to write down the governing equations by taking into account the temperature field as well.

The equation for the temperature field is derived from the energy equation (4.28). The resulting equation is the same as for pure materials, (3.6):

$$\frac{\partial T}{\partial t} = D_T \Delta T + \frac{L}{c_p} \frac{p(\phi)}{\partial t}. \quad (4.60)$$



Normally, the dynamics of the concentration field are much slower than the dynamics of the temperature field. In our simulation  $Pr \equiv D_T/D_C \sim 100$ . For this reason, we do not take the governing equation for the temperature field into account; temperature is treated as a static field.

Another difference between isothermal and non-isothermal models is seen in the concentration equation. Thus, in the Eq. (4.53) a new term appears:

$$\frac{\partial c}{\partial t} = \nabla \left( \frac{M_c}{T} f_l'' \left( \frac{\partial c_l}{\partial c} \vec{\nabla} c + \frac{\partial c_l}{\partial \phi} \vec{\nabla} \phi \right) + \frac{M_c}{T} \vec{\nabla} T \left( f_l'' \frac{\partial c_l}{\partial T} + \partial_T f_l' \right) \right), \quad (4.61)$$

where the index  $T$  indicates a derivative on temperature.

From the Eqs. (4.47) and (4.48), the expressions for the derivatives of  $c_l$  and  $c_s$  of  $T$  can be obtained:

$$\frac{\partial c_l}{\partial T} = p(\phi) \frac{\partial_T f_s' - \partial_T f_l'}{p(\phi) f_l'' + \tilde{p}(\phi) f_s''}, \quad \frac{\partial c_s}{\partial T} = -\tilde{p}(\phi) \frac{\partial_T f_s' - \partial_T f_l'}{p(\phi) f_l'' + \tilde{p}(\phi) f_s''}. \quad (4.62)$$

These expressions give an additional term in Eq. (4.54):

$$\frac{\partial c}{\partial t} = \nabla(D\nabla c) + \nabla \left( (c_l - c_s) D \nabla p(\phi) + \frac{\partial_T f_s' - \partial_T f_l'}{f_s''} p(\phi) \nabla T \right). \quad (4.63)$$

Substituting the explicit expressions for  $f_l$  and  $f_s$  in the equation yields:

$$\begin{aligned} \frac{\partial c}{\partial t} = & \nabla(D\nabla c) + \nabla(D[c_l - c_s] \nabla p(\phi)) \\ & + \nabla \left( \frac{p(\phi) c_s \tilde{c}_s L_\Delta}{T^2 R / V_m} \nabla T \right). \end{aligned}$$

Simulations show that the contribution from the additional term is negligible for the modeled system. All simulations, therefore, were made in the frame of the isothermal model.

## 4.4 Numerical scheme

The governing equations of the PF model are solved numerically. Various approaches are used for such simulations. The simplest and most widely spread method is the finite difference method [69]. The finite volumes and finite elements methods were applied also for this problem. Lan and Chang used an adaptive approach based on the finite volume method [34]. Loginova and Amberg used a finite-elements method [37]. These approaches allow different resolutions inside and outside of the transition region. The disadvantage in all of these methods is their poor scalability for parallel simulations. Another drawback is the high complexity of program code. It should be mentioned that both the finite volumes and finite elements techniques were used only for the WBM model, and never for the KKS model.

The differential equation for the phase-field is solved by an explicit finite difference scheme. The operator with mixed spatial derivatives is discretized by a scheme with a 9-point template [26], see Appendix D.2.

Two different numerical models are used in this work. The first one is the special finite difference scheme, which ensures the mass conservation law. The second method is similar to the one applied for the dendritic growth in the previous section. For the entire system a mixed scheme is used: a finite difference scheme for the phase-field equation, and the MRLK method for the concentration equation. Both methods will be discussed in this section.

### 4.4.1 Finite difference approach for the concentration equation

We have the advection-reaction-diffusion equation (4.54) for  $c$ , a finite-difference numerical scheme was used for its solution. The simulation domain has a rectangular form. It can be virtually divided into three parts according to the value of  $\phi$ . In the first part, where  $\phi = 0$ , only the Navier-Stocks equation and the advection-diffusion equation for  $c$  need to be solved. In the second part, where  $0 < \phi < 1$ , the equations (4.52), (4.54) need to be solved in addition to the Navier-Stocks equation, supplemented with the solid-liquid collision term. Flow is simulated with the LBGK method, which has been discussed in the previous sections. The third part is a solidified crystal, therefore there are no processes to simulate.

In the first part, the classic Lax-Wendroff method [60] for simulation of the advection diffusion process is applied:

$$c(\vec{r}, t + 1) = c_0 + \sum_i c_i (D^* \alpha_{\Delta i} - \alpha_{\nabla i} u_{ii}), \quad (4.64)$$

where  $i$  takes the values  $0, \dots, 4$  for the 5-point template, respectively.  $D^*$  is a rescaled diffusion coefficient, which is related to the physical one via  $D^* = D \frac{\delta_t}{\delta_x^2}$ .

$$c_i \equiv c(\vec{r} + \vec{a}_i), \quad u_{ij} \equiv \vec{a}_i \vec{u}^*(\vec{r} + \vec{a}_j), \quad \vec{u}^* \equiv \vec{u} \frac{\delta_t}{\delta_x},$$

where  $\vec{a}_i$  are the lattice vectors:

$$\begin{aligned} \vec{a}_0 &= (0, 0), \\ \vec{a}_1 &= (0, 1), \quad \vec{a}_2 = (1, 0), \quad \vec{a}_3 = (0, -1), \quad \vec{a}_4 = (-1, 0). \end{aligned}$$

and  $\alpha_{\Delta i}$  and  $\alpha_{\nabla i}$  are weight coefficients:

$$\alpha_{\Delta i} = \begin{cases} -4, & i = 0 \\ 1, & i = 1..4 \end{cases}, \quad \alpha_{\nabla i} = \begin{cases} 0, & i = 0 \\ \frac{1}{2}, & i = 1..4 \end{cases}.$$

This method allows coupling with the LBGK scheme. The Courant stability conditions are:

$$D^* < \frac{1}{2d}, \quad u^* < 1. \quad (4.65)$$

Another limit is  $u^*/D^* < 10$ . The Lax-Wendroff method has a numerical diffusion of order  $u^{*2}$ , whose effect can be eliminated by rescaling  $D$ , [60, 48]:

$$D_x = D^* + u_x^{*2}, \quad D_y = D^* + u_y^{*2}.$$

The second part of the domain is the most problematic one from the numerical point of view. The phase-field governing equation (4.52) is similar to the one for pure materials (3.5). The only difference being in the definition of the undercooling term. The undercooling is computed by the expression (4.59). The equation for the concentration (4.54) is more complicated. It is very important to secure the mass conservation in a numerical scheme. The equation contains differential constructions in the form  $\nabla(A\nabla B)$ . The conservative representation is written here:

$$\overline{\nabla(A\nabla B)} = \frac{1}{2\delta_x^2} \sum_i [A(\vec{r} + \delta_x \vec{e}_i) + A(\vec{r})][B(\vec{r} + \delta_x \vec{e}_i) - B(\vec{r})].$$

This expression allows us to discretize the equation (4.54).

Like any explicit difference scheme, the discretization implies a severe Courant restriction on the time step,  $\delta_t < \alpha_e \delta_x^2$ , where  $\alpha_e$  is the coefficient defined by the discrete equation. This is in contrast to the purely advective Courant limit of the LB scheme,  $\delta_t = \delta_x/|\vec{a}_i|$ . Such differences in the Courant limits for both schemes lead us to construct the MRLK discretization for the diffusion equation.

### 4.4.2 MRLK discretization of the concentration equation

The MRLK discretization for this system is quite similar to that used for pure materials. As in the case of the finite difference method, the domain can be divided into three parts. The advection-diffusion equation is simulated with the corresponding MRLK method discussed above. In this case, the Courant conditions (4.65) are better than in the case of the FD scheme.

There are some differences between equations for solidification in pure materials and in binary alloys. The first effect is the dependence of the diffusion coefficient on the phase, i.e.  $D = D(\phi)$ . This dependence is naturally realized without any additional changes in the numerical scheme. The relaxation matrix has the form (2.24) with the only difference being that matrix  $\Lambda$  becomes specially dependent because  $D = D(\phi)$ .

The second effect is related to the additional non-linear term appearing in the second part of domain. The equation (4.54) is rewritten in the following form:

$$\frac{\partial c}{\partial t} = \nabla(D\nabla c) - \nabla \cdot \vec{J}^{add}, \quad J^{add} \equiv D[c_s - c_l]\nabla p(\phi). \quad (4.66)$$

The idea is to represent the additional term in the diffusion equation as a term in flux. The MRLK discretization for binary alloys is based on the known discrete kinetic equation (2.8):

$$f_i(\vec{r} + \vec{a}_i, t + 1) - f_i(\vec{r}, t) = \sum_j \Omega_{ij}(f^{eq}(\vec{r}, t)_j - f_j(\vec{r}, t)).$$

The lattice velocity vectors  $\vec{a}_i$  are defined in the same way as in Chapter 2. The density functions code the concentration as follows:

$$c(\vec{r}, t) = \sum_i f_i.$$

The continuum limit of this equation was considered in Chapter 2. This equation approximates the following continuum equation:

$$\frac{\partial c}{\partial t} = -\nabla \cdot \vec{J}^{eq} + \nabla(D\nabla\rho). \quad (4.67)$$

Comparison between the equations (4.66) and (4.67) gives the expression for equilibrium distribution function:

$$f_i^{eq} = \frac{1}{a_s} \vec{a}_i \cdot \vec{J}^{add}. \quad (4.68)$$

Another positive feature of this method should be mentioned: the computation procedure contains less floating point operations than the FD approach. Thus, this method has a better performance versus that of the FD approach, even in the case of equal time steps.

## 4.5 Pattern formation for NiCu alloys

NiCu is a typical test material used by many authors [69, 37, 13]. Its phase diagram is shown in Fig. 4.4. The material parameters are listed in Tables 4.1 and 4.2.

The described phase-field model is applied for simulation of directional solidification of the NiCu alloy in a rectangular computational domain. Periodic boundary conditions are taken in  $x$ -direction. The initial crystal plane is orthogonal to the  $y$ -axis. The temperature profile is set up by a constant temperature gradient,  $G_T$ , and is moved with a constant velocity  $v_{pull}$ . Thus, the local temperature can be defined by the expression:

$$T(x, y) = T_0 + G_T(v_{pull}t - y), \quad G_T < 0.$$

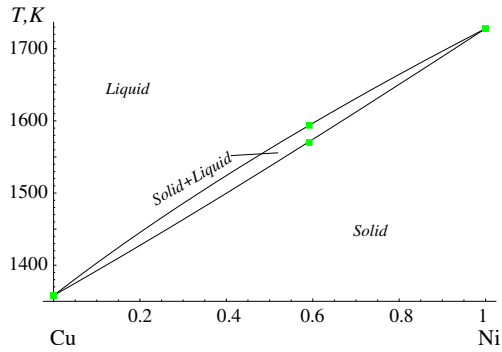


**Figure 4.4:** Phase-diagram for NiCu alloy. Points indicate measurements [43]. The lines correspond to the liquidus and solidus curve obtained from the free energy function.

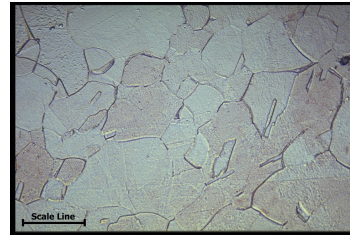


**Figure 4.5:** Copper-nickel alloy,  $\text{Ni}_{0.1}\text{Cu}_{0.9}$ . Scale Line Length 25  $\mu\text{m}$ .

**Table 4.1:** Material parameters of the Ni an Cu.

Physical value	Ni	Cu
Melting-point temperature	1728 K	1358 K
Density	$8.9 \cdot 10^3 \frac{\text{kg}}{\text{m}^3}$	$8.9 \cdot 10^3 \frac{\text{kg}}{\text{m}^3}$
Molar volume	$6.59 \cdot 10^{-6} \frac{\text{m}^3}{\text{mole}}$	$7.11 \cdot 10^{-6} \frac{\text{m}^3}{\text{mole}}$
Heat capacity	$440 \frac{\text{J}}{\text{kg K}}$	$380 \frac{\text{J}}{\text{kg K}}$
Thermal conductivity	$90.7 \frac{\text{W}}{\text{m K}}$	$401 \frac{\text{W}}{\text{m K}}$
Latent heat	$17.57 \frac{\text{kJ}}{\text{mole}}$	$13.01 \frac{\text{kJ}}{\text{mole}}$

**Table 4.2:** Material parameters of the NiCu alloy, [67].

Name	Value
Gibbs-Thomson coefficient	$2.7 \cdot 10^{-7} \text{ K m}$
Kinetic coefficient	$2 \text{ m/s K}$
Diffusion coefficient of Ni in Cu	$10^{-9} \text{ m}^2/\text{s}$

This is a typical approximation for directional solidification in binary alloys. We are able to apply this approximation because the dynamic of the temperature field is much faster than the dynamics of the concentration field.

The computational domain moves with the advancing solidification front (in y-direction) in order to keep the interface within the same region. More precisely, in every time step we measure the shift  $\Delta_{shift}y$  of the interface (maximum point of the interface) according to the previous time step. The last rows in the solid up to a height of  $\Delta_{shift}y$ , are chopped and the same number of rows are added to the liquid at the end of the domain. The concentration at the liquid end of the computational domain is fixed.

The phase-field equation is computed only in the region defined by the values of the phase-field,  $10^{-4} < \phi < 1 - 10^{-4}$ . In this region we have used a special mass-conserving scheme for the advection-diffusion equation, where we take into account that the diffusion coefficient  $D(\phi)$  changes rapidly within the transition region:

$$D(\phi) = D_0(1 - \phi).$$

The thin interface limit for the KKS model exists only in the case of dilute alloys. The simulated NiCu alloy can not be treated as a dilute one. The expressions for the parameters are therefore taken in the form of a sharp interface limit, Eq. (4.41).

### 4.5.1 1D simulations

Both numerical methods for the concentration field, discussed in Section 4.4, have been tested on a 1D model of directional crystallization. The 1D simulation corresponds to the motion of a flat



interface. The simulation domain has a length  $l_y$ , the interface between liquid and solid is placed in  $y_0 < l_y$ . The initial condition for the phase field is:

$$\phi(y, 0) = \frac{1}{2} - \frac{1}{2} \tanh\left(\frac{\sqrt{W}}{\xi_S \sqrt{2}}(y - y_0)\right).$$

This initial condition defines  $[0, y_0]$  as a solid and  $[y_0, l_y]$  as a melt.  $\phi = 0.5$  corresponds to the interface. The analytical solution, (4.21), shows that in the diffusion controlled case, i.e.  $\delta_c = \infty$ , the distribution coefficient,  $k_\infty$  is equal to 1. This gives us the concentration boundary condition for the liquid end of the domain:

$$c(l_y, t) = c_{s0}.$$

Please note that  $c_{s0}$  is the expected concentration in a solid. The initial condition for the concentration field are taken as:

$$c(y, 0) = c_{s0}\phi(y, 0) + \left(\frac{y}{y_0}(c_l^0 - c_{s0}) + c_{s0}\right)(1 - \phi(y, 0)),$$

Fig.4.6 shows a 1D simulation for a NiCu alloy. The phase-field and constitutional undercooling,  $\Theta$ , are plotted there. The undercooled region seen ahead of the interface causes the Mullin-Sekerka instability. Fig.4.6b shows the concentration profile and the profiles of  $c_s$  and  $c_l$ . Two straight lines mark the liquidus and solidus concentrations, (4.13). The undercooled (supersaturated) region is easily recognizable in this plot.

The situation in the transition region needs to be discussed in detail. There is little supersaturation inside of the transition region. This supersaturation cause an additional non-linear term in the equation which decreases the height of doublewell potential. At the moment, we can not find the source of this additional potential. The additional potential increases the width of the transition

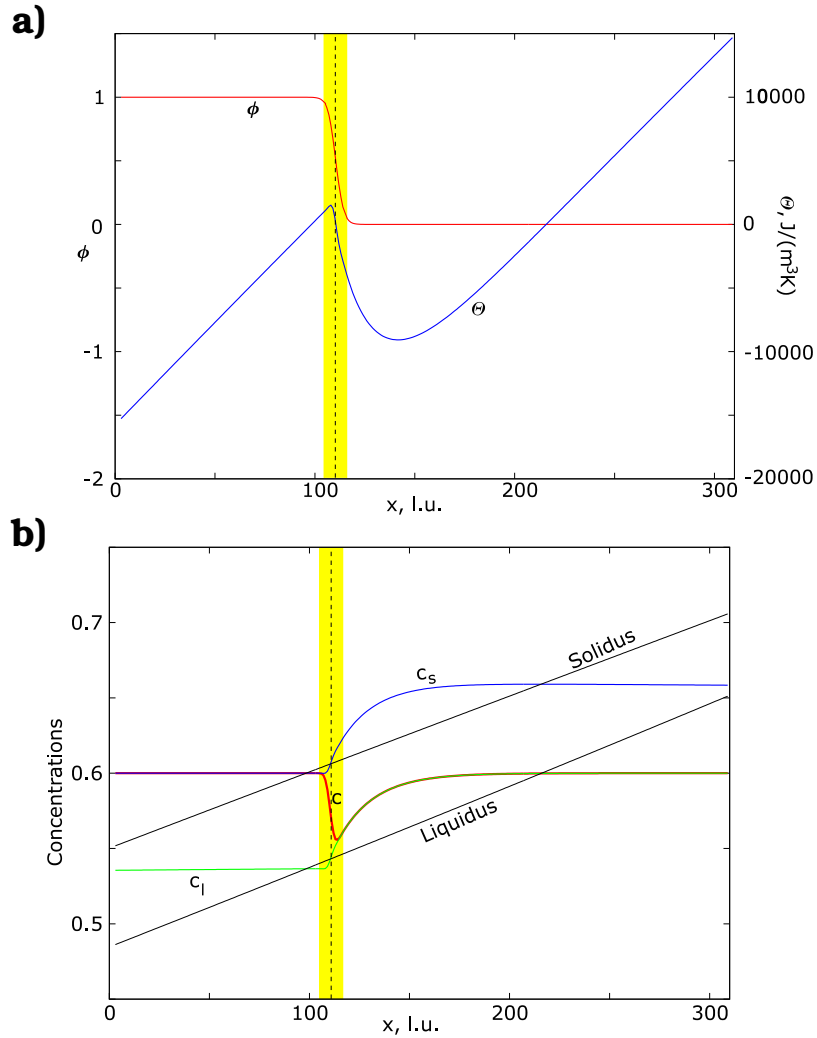


**Figure 4.6:** 1D simulation for NiCu. The vertical dashed line marks the interface position. The transition region is marked by yellow color.  $\delta_x = 8.86 \cdot 10^{-8}$  m,  $\delta_t = 2.42 \cdot 10^{-7}$  s,  $l_y = 310\delta_x$ ,  $x_0 = 200\delta_x$ ,  $v_{pull} = 6.25 \cdot 10^{-4}$  m/s,  $G_T = 2.15 \cdot 10^6 \frac{\text{K}}{\text{m}}$ . **a:** Profile of phase-field  $\phi$  and supersaturation  $\Theta$ . **b:** Concentration profiles, separation of concentration in different phases and equilibrium concentrations (liquidus, solidus).

region. In this particular case simulation gives an increase of less than 10%.

### 4.5.2 2D simulation

A typical simulation picture looks like the one in Fig. 4.9(right). The solidification interface, corresponding to  $\phi = 0.5$ , is marked with a black line. The fraction of Ni is color coded. The alloy solidifies from bottom to top and the form of the solidification front affects the local fraction of Ni in the solid phase. There are thick lamellas corresponding to the hills on the surface, as well as thin traces of liquid grooves. The liquid grooves emit liquid solute-enriched droplets. These droplets solidify later (deeper) in the crystal. The Ni poor round regions, seen in the figure, correspond to such crystallized droplets. A more detailed study of the question of stability of liquid grooves has been made by M. Conti and U.M.B. Marconi for cases with large anisotropy [14].

We compared our simulation results with those of Boettinger et al. [7] and Lan et al. [34]. Dependencies of patterns on the pulling rates and the temperature gradient have been therefore examined. It is necessary to mention some words about this comparison. Both works deal with the WBM phase-field model. This model has been discussed in Section 4.2.2. Fig. 4.3 demonstrates that there is a strong influence from the additional double-well potential. The influence of this effect is rather complex because the real value of  $W$  determines both the width of phase transition region and the surface tension. In order to compare our simulation with the results of the WBM model, we took a six times larger value of surface tension than given in Table 4.2,  $\gamma = 1.776 \cdot 10^{-6} \text{ J/m}^2$ .

**Table 4.3:** Dependence of the wavelength of the patterns on the pulling velocity. The results are compared with simulations of Lan et al. [34] and Boettinger et al. [7]

pulling velocity (m/s)	$1.25 \cdot 10^{-3}$	$2.5 \cdot 10^{-3}$	$5.0 \cdot 10^{-3}$
$\lambda$ , (m), this model	$3.8 \cdot 10^{-6}$	$3.3 \cdot 10^{-6}$	$2.4 \cdot 10^{-6}$
$\lambda$ , (m), Boettinger et al. [7]	$2.84 \cdot 10^{-6}$	$2.04 \cdot 10^{-6}$	$1.54 \cdot 10^{-6}$
$\lambda$ , (m), Lan et al. [34]	$4.61 \cdot 10^{-6}$	$3.29 \cdot 10^{-6}$	$1.92 \cdot 10^{-6}$

In Table 4.3 the computed wave lengths of the patterns are listed for different pulling velocities. The temperature gradient is fixed to the value  $G_T = 2.15 \cdot 10^6$  K/m. Ni concentration at the liquid end is  $c_l = 0.56$ . Initial interface temperature and position are taken as  $T_{i0} = 1570$  K,  $y_0 = 200 \times \delta_x$ . The simulation results are compared to those obtained by Lan et al. [34] and Boettinger et al. [7], and are seen to be in reasonable agreement. Fig. 4.7 shows the dependence of the wave length on the pulling velocity. A stable periodic structure is obtained for small velocities. For instance, a periodic structure is obtained for  $v_{pull} = 6.25 \cdot 10^{-4}$  m/s, see Fig. 4.9(left). The same simulation is repeated with a coarser grid,  $\delta_x = 1.77 \cdot 10^{-7}$  m. The difference in the measured value of  $\lambda$  is less than 10%.

Temperature gradient influences the wavelength as well, see Fig. 4.8. Theory of directional solidification, [33], predicts that this dependence has the form:

$$\lambda \sim G_T^{-0.5}.$$

The plot demonstrates strong agreement between the simulation results and the theory.

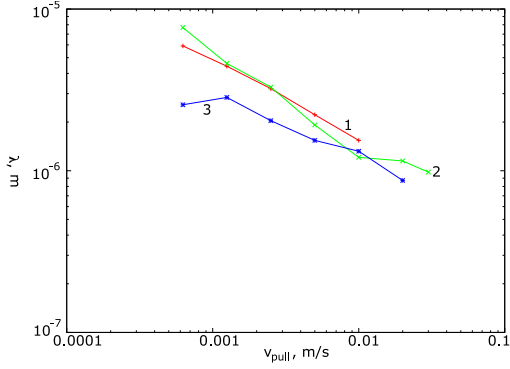


**Figure 4.7:** Dependence of the wavelength of the patterns on the pulling velocity. **line 1:** results obtained with the KKS model; **line 2:** Lan et al. [34]; **line 3:** Boettinger et al. [7]

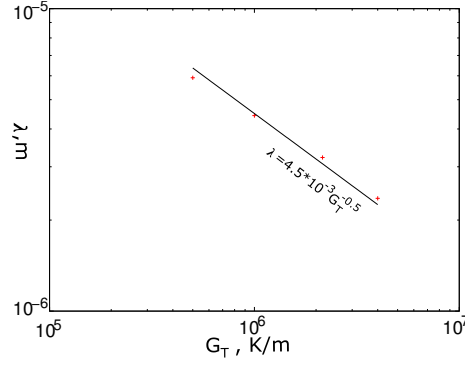


**Figure 4.8:** Dependence of the wavelength of the patterns on the temperature gradient. The straight line marks the theoretical slope of the dependence.

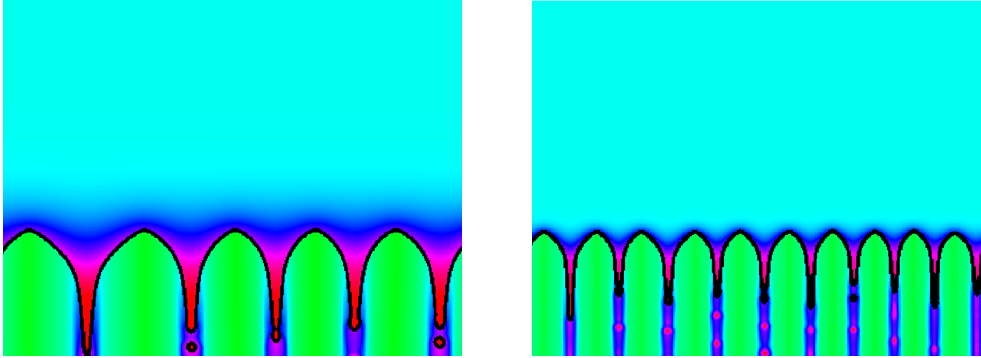


**Figure 4.9:** Concentration profile for the NiCu alloy with different pulling rates.  $\epsilon_4 = 0.05$ ,  $G_T = 2.15 \times 10^6$  K/m,  $\delta_x = 8.86 \cdot 10^{-8}$  m, domain size  $400 \times 310$  l.u.,  $\delta_t = 2.42 \cdot 10^{-7}$  s, number of time steps is 500000,  $c_{l\infty} = 0.56$ . Interface fixed at 110 l.u.. Colors code the local concentration of Ni. The thin black line corresponds to  $\phi = 0.5$ . **left:**  $v_{pull} = 6.25 \cdot 10^{-4}$  m/s; **right:**  $v_{pull} = 2.5 \cdot 10^{-3}$  m/s

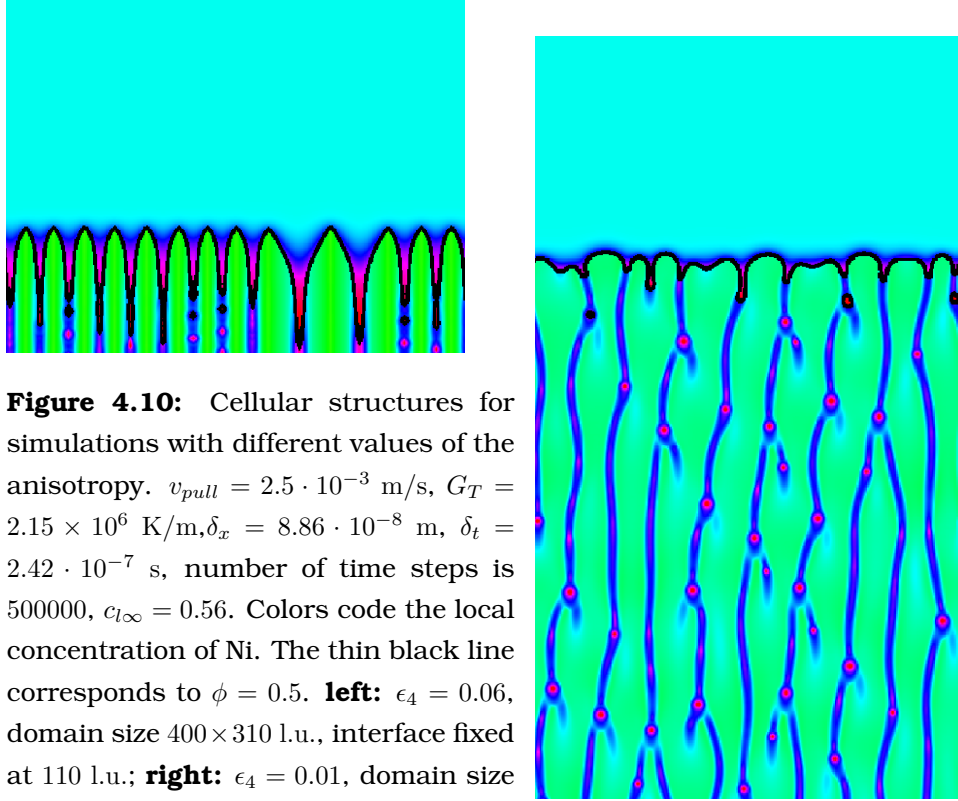


**Figure 4.10:** Cellular structures for simulations with different values of the anisotropy.  $v_{pull} = 2.5 \cdot 10^{-3}$  m/s,  $G_T = 2.15 \times 10^6$  K/m,  $\delta_x = 8.86 \cdot 10^{-8}$  m,  $\delta_t = 2.42 \cdot 10^{-7}$  s, number of time steps is 500000,  $c_{l\infty} = 0.56$ . Colors code the local concentration of Ni. The thin black line corresponds to  $\phi = 0.5$ . **left:**  $\epsilon_4 = 0.06$ , domain size  $400 \times 310$  l.u., interface fixed at 110 l.u.; **right:**  $\epsilon_4 = 0.01$ , domain size  $400 \times 710$  l.u., interface fixed at 510 l.u.;

### 4.5.3 Role of anisotropy

Here we would like to study the influence of crystallographic anisotropy on the properties of the cellular structure. Usually there is only qualitative knowledge about the anisotropy, e.g. dependence of the surface tension or kinetic coefficient on the orientation. The role of anisotropy in solidification has been investigated by Kessler and Levine for the dendritic growth, see [28]. Anisotropy stabilizes the dendritic tip, e.g. in the isotropic case the value and direction of the dendritic tip velocity changes. Our investigation gives a similar conclusion for alloys.

All simulations are made for four-fold anisotropy in surface ten-

sion, see Eq. (3.22). Different behavior is observed for different values of the anisotropy parameter. Figs. 4.9(right) and 4.10(right) show simulations with  $\epsilon_4 = 0.05$  and the with  $\epsilon_4 = 0.01$ , respectively. The relation between cellular structure parameters and  $\epsilon_4$  is rather complex. The stable cellular structure becomes irregular and transient for small  $\epsilon_4$ , see Figs. 4.9(right) and 4.10(right). The Ni distribution in the crystal shows that some cells disappear and new cells appear during the growth. This behavior is observed for simulations with  $\epsilon_4$  from the interval  $[0, 0.015]$ . An irregular structure is seen also for larger  $\epsilon_4$ , but this structure is stable. Fig. 4.10(left) shows this phenomenon, the value of anisotropy is rather large in this simulation,  $\epsilon = 0.06$ . Different patterns seem to be stable under these conditions. Once appearing this structure does not undergo any changes during more than 20000 time steps.

The drop-like inclusions, see Fig. 4.9(right), in the solid phase appears for  $\epsilon_4 > 0.03$ . The inclusions disappear with the decreasing of anisotropy and appear again with an irregular structure.

#### 4.5.4 Influence of shear flow

Flow is another factor with strong impact on the patterns. An induced flow changes the concentration and temperature conditions near the interface thereby influencing the growing structure. The flow can be induced by macroscopic processes in the system, for instance the temperature-gradient or the concentration-gradient induced by solidification.

The flow effect is clearly seen from comparison between Figs.4.9(right) and 4.11(left). The flow in the last simulation is directed from left to right. The fingers are tilted towards the flow. The

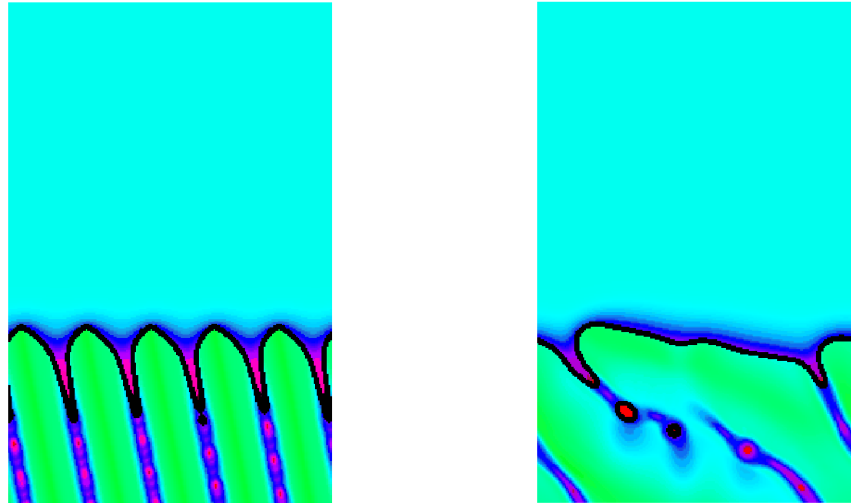


**Figure 4.11:** Cellular growth of NiCu in presence of flow.  $v_{pull} = 2.5 \cdot 10^{-3}$  m/s,  $G_T = 2.15 \times 10^6$  K/m. There is a flow in  $x$ -direction,  $u_t = 0.05$  m/s. **left:** with anisotropy,  $\epsilon_4 = 0.05$ ; **right:** without anisotropy,  $\epsilon_4 = 0.00$

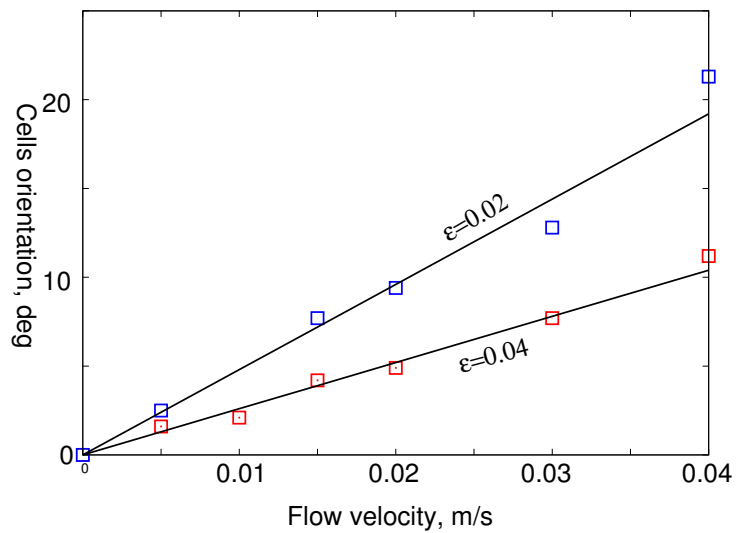


**Figure 4.12:** Cells orientation angle vs. flow velocity for two different values of anisotropy.  $v_{pull} = 2.5 \cdot 10^{-3}$  m/s,  $G_T = 2.15 \times 10^6$  K/m. There is a flow in  $y$ -direction  
**Top line:**  $\epsilon = 0.02$ , **Bottom line:**  $\epsilon = 0.04$ .



orientation angle depends on flow velocity and on the partition coefficient. E.g., the fingers are oriented against the flow for  $k < 1$  and towards the flow in a case with  $k > 1$ . The dependence of the angle on the flow velocity is plotted in Fig. 4.12. Two lines correspond to the different values of anisotropy.

Fig. 4.11(right) shows an example of the influence of the flow on the crystal without anisotropy in surface tension. There is no regular structure contrary to the growth with anisotropy. Some “heads” move along the interface in opposition to flow direction. A similar effect is observed with anisotropy and with strong flow. It means that the flow is able to destroy the cellular structure of the interface.

# Chapter 5

## Cellular growth in GeSi crystals

The goal of the thesis is to study pattern formation in GeSi crystals. The crystals are grown using the Czochralski method. A sketch of the Czochralski furnace is shown in Fig. 5.1. Furnace sizes are very large in comparison to the size of the studied microstructure, e.g. the crucible radius is 60 mm and the wavelength of the surface patterns is  $\sim 0.1$  mm.

Material data is a problem which frequently arises in the modelling of crystal growth. Some parameters required in the simulation are not known or have different values in different sources. In the case of GeSi crystals, the problematic material parameter is the diffusion coefficient of Si in a Ge melt. The diffusion coefficient was measured in the sixties of the previous century [49], with a value of  $2 \cdot 10^{-8}$  m<sup>2</sup>/s. More recent records containing measurements have not been found. Recent results for the molecular dynamics simulation [74] for diffusion processes show a value of  $D$  for Si in Ge of  $2.3 \cdot 10^{-9}$  m<sup>2</sup>/s. Independently, D. Stock made molecular dynamic

simulations for the diffusion coefficient, and obtained the value,  $6 \cdot 10^{-9} \text{ m}^2/\text{s}$ . The possible source of the difference between experiment and simulation is convection effects, which are hard to account for in the analysis of the results, see [24]. As one can see, it is hard to judge the real value of the diffusion coefficient. We therefore made simulations for both values of  $D$ :  $D_{MD} = 6 \cdot 10^{-9} \text{ m}^2/\text{s}$  and  $D_{ex} = 3 \cdot 10^{-8} \text{ m}^2/\text{s}$ .

To summarize, in spite of the existing uncertainty in the simulation and material parameters, we will try to obtain results, which are useful for further GeSi investigations.

Investigations of pattern formation in crystal growth raise questions about crystallographic anisotropy particularly regarding its influence on the stability and morphology of the patterns. Different anisotropy models for simulations in crystal growth appear in the literature [63, 50, 68]. The anisotropy can be incorporated into the model in the term of surface tension and/or in kinetics. Currently, knowledge regarding this dependence for various materials is rather poor, and usually only qualitative. We therefore decide not to focus on the investigation of anisotropy influence on the GeSi growth. We have already discussed the influence of anisotropy in surface tension on the pattern formation for the case of NiCu, Section 4.5.3. For the GeSi simulation, we took the same anisotropy model as used for NiCu. The value of the anisotropy factor is taken to be equal to 3%.

Now, let us say some words about the numerical realization of this model. It is important to note that the GeSi modelling is based on the KKS phase-field model with the modified surface-tension term. The KKS phase-field model has already been applied for solidification in the NiCu alloy, see Section 4.5. The properties and

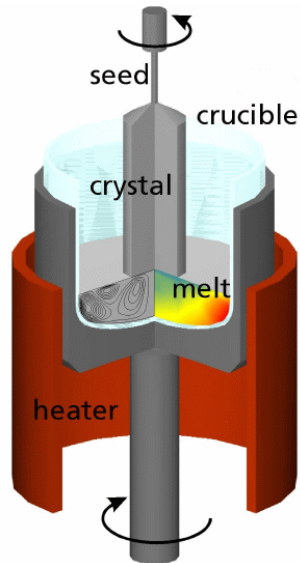


**Figure 5.1:** Schematic representation of the Czochralski furnace

processing of NiCu and GeSi are very different: NiCu is a metal, casting conditions correspond to a high solidification velocity and a pronounced cellular structure. Contrarily, GeSi is a semiconducting material which is grown with a small solidification velocity and as a mono-crystal, and its cellular structure has a small amplitude in comparison to the wavelength. As a result, the length scales of micro-structures in both materials are different, see Figs. 1.5 and 4.5.

## 5.1 The Czochralski growth

Fig. 5.1 shows a sketch of the Czochralski furnace. The crucible contains melted material solidifying on the crystal surface. The crystal is pulled out of the melt with a constant velocity. Some growth parameters are listed in Table 5.1.

**Table 5.1:** Growth parameters.

$R_{crucible}$	$R_{crystal}$	$\Omega_{crucible}$	$\Omega_{crystal}$	$c_l^\infty$	$c_s$	$v_{pull}$
60 mm	15 mm	10 rpm	-15 rpm	1%	2%	6 $\frac{\text{mm}}{\text{h}}$

Heaters keep the crucible hot to make the temperature of the liquid higher than the solidification temperature of the material. The grown crystal is cooled down, and heat is thus removed from the front of the solidification throughout the crystal. The temperature difference in the melt causes melt convection. Another source of flow is the rotation of the crucible and the crystal. The GeSi crystals were grown with counter rotation for better mixing in the system [70]. The resulting flow has a rather complex character and is usually non-axisymmetric and unstationary [39].

The level of the melt decreases during crystal growth, causing changes in melt the flow, temperature and concentration fields. These changes have a time scale of  $\sim 1$  h because of the low pulling velocity. These processes cause changes in the crystal diameter and the concentration of Si. The constant diameter is maintained by the changing of external parameters as needed, e.g. power of the heaters.

The segregation coefficient of Si is greater than 1, i.e. the Si concentration in the melt is about 1% and in the crystal about 2%. Therefore, the Si-enrichment of the crystal during growth causes Si-depletion in the melt. The classic Czochralski method has been modified by N.V. Abrosimov et al. [2, 1] in order to keep a constant concentration of Si in the melt. Three silicon rods, responsible for maintenance of the constant concentration, are immersed slowly into the melt. Their dissolution assures the release of the necessary

amount of Si into the solute. The rods destroy the axial symmetry of the system and produce additional complexity.

Traces of these processes are seen in the obtained crystals. An analysis of the crystal allows one to determine the time scales of the different processes. There are high frequency fluctuations in temperature and concentration fields. These fluctuations induce striations in the crystal, see Fig. 1.5. Unfortunately, the analysis of the crystal does not permit one to make any separate conclusions regarding fluctuations of temperature or concentration. The distance between striations indicates the time scale of the fluctuations,  $\sim 5$  s. The frequency of these fluctuations is equal to the rotation frequency of the crystal. Thus, we are able to conclude that the oscillation originates from the disturbances in axial symmetry. Other processes in the system have a larger time scale. The crystal cross-section seen in Fig. 1.3, has regions with different types of microstructure. The changes in microstructure are caused by changes in conditions near the growing surface. The time scale of these changes is  $\sim 1$  h.

Using a numerical simulation it is possible to obtain some information about the conditions near the crystal surface. O.V. Smirnova et al. [56] made a macroscopic axial symmetric modelling of the furnace. The value of the temperature gradient near the interface,  $G_T$ , has been obtained through this simulation. The temperature gradient changes along the crystal surface from the value  $0.9 \frac{\text{K}}{\text{mm}}$  in the center to  $1.2 \frac{\text{K}}{\text{mm}}$  on the crystal boundary.

In our modelling we would like to simulate the processes taking place in the vicinity of the interface. The size of the simulation domain is of the order of 1 mm.

**Table 5.2:** Dimensionless parameters characterizing processes in crucible for GeSi growth.

$Re_{crucible}$	$Re_{crystal}$	$Gr$	$Ra$	$Sc$
$4 \cdot 10^3$	$2 \cdot 10^2$	$6 \cdot 10^6$	$7 \cdot 10^4$	17

## 5.2 Analytical estimations

A great amount of work regarding the Czochralski growth method was done during the last century [70]. The experience collected in this field has allowed us to make an estimation of certain values that are of particular interest for mesoscopic simulations. In our simulation, we try to reproduce the processes near the crystal surface. Information about the flow and the concentration field near the interface is therefore important. There are two sources of such information: a global simulation [56] and analysis of the furnace and the obtained crystal. Regarding the estimations made from the analysis, a crucial physical value for our modelling is the thickness of the boundary layers for flow,  $\delta_m$ , and for concentration  $\delta_c$ . Both boundary layers are related via the following equation, (see pg. 25 in [61]):

$$\delta_c = \delta_m Sc^{-1/3},$$

where  $Sc$  is the Schmidt number,  $Sc \equiv \nu/D$ . For the GeSi alloy  $Sc$  is about 17.

The estimation of  $\delta_c$  requires the analysis of the grown crystal. The grown GeSi crystals contain 2% Si. Experiments have shown that the concentration in liquid is approximately 1% [1, 2]. This allows us to conclude that  $k_\infty \approx 2$ . The boundary layer thickness  $\delta_c$

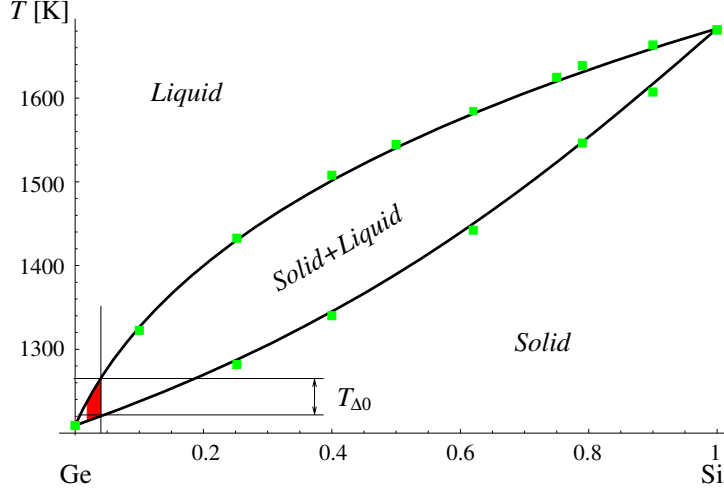


**Figure 5.2:** Phase-diagram for GeSi. Green points show measured values [43, 15] and the black line corresponds to the phase-field approximation. The concentration region in which the analyzed crystals have been grown is marked by the red color. The free energy function was modified in order to fit the experimental data:  $L = L_0(1 + \alpha T)$ ,  $\alpha_{Si} = 2 \cdot 10^{-4} \text{K}^{-1}$ ,  $\alpha_{Ge} = 9 \cdot 10^{-5} \text{K}^{-1}$ .

can now be computed using Eq. (4.21):

$$\delta_c = \frac{D}{v_{pull}} \ln \frac{k_\infty(1 - \hat{k})}{\hat{k}(1 - k_\infty)}.$$

The value of  $\hat{k}$  is known from the phase diagram (see Fig. 5.2) and it equals 5.33. For  $D = 3 \cdot 10^{-8} \text{ m}^2/\text{s}$ , the obtained width of the diffusion boundary layer is  $\delta_c = 8 \text{ mm}$ .

## 5.3 1D simulations

Different phase-field models have been discussed in the previous chapters. Most articles deal with metallic alloys [13, 34, 37, 67]; usually the WBM model is used for simulations, and publications with the KKS model are rather rare. We made some 1D simulations



in order to test the behavior of the model in the case of GeSi growth parameters.

The simulation domain is defined similarly to that of the simulations of NiCu. It has the length  $l_y$ , and the crystal surface is placed in  $y_0 < l_y$ . The initial condition for the phase field is:

$$\phi(y, 0) = \frac{1}{2} - \frac{1}{2} \tanh\left(\frac{\sqrt{W}}{\xi_S \sqrt{2}}(y - y_0)\right).$$

The initial condition for the concentration field is expressed with the following formula:

$$c(y, 0) = c_{s0}\phi(y, 0) + \left(\frac{y}{y_0}(c_l^0 - c_{l0}) + c_{l0}\right)(1 - \phi(y, 0)),$$

where  $c_{l0}$  is the initial concentration on the right boundary. Note, in contrast to the NiCu case, concentration on the liquid boundary is not equal to  $c_{s0}$ .

The temperature is taken as an external field, as well:

$$T(y, t) = T_0 + G_T(y + v_{pull}t).$$

The interface is kept near the position  $y_0$ . The domain-moving procedure is similar to that for NiCu.

Let us turn now to the question of the boundary conditions. The concentration boundary conditions used for the NiCu solidification are not applicable in the simulated system. It is based on the assumption that the domain with the length  $l$  can be considered as an infinite domain, in other words,  $c_{l0}$  is assumed to be equal to  $c_\infty$ . This statement requires, domain length of  $\sim 10$  mm in the GeSi case. This size exceeds the estimated value of the diffusion boundary layer, see Section 5.2. We formulated, therefore, special boundary conditions. The basic idea is that the Si flux in

the melt towards the growing crystal is equal to the absorption flux on the crystal surface. Two facts should be taken into account:

- a difference between the solid and liquid concentrations destroys the balance in the liquid,
- the domain is constantly moving with the interface, which causes constant flux in the system.

These two facts allow the formula for flux on the liquid side of the domain to be written:

$$J(l_y, t) = (c(l_y, t) - c_{s0})v_{pull}, \quad (5.1)$$

where  $c_{s0}$  is the expected concentration in the solid. Indeed, this expression defines the flux value, which covers adsorption (desorption) on the interface with regard to the moving domain. These boundary conditions are simplified to condition  $c(l_y, t) = c_{s0}$  for a large domain.

Figs.5.3 shows 1D simulation results. The differences between the NiCu simulation, Fig. 4.6, and this one are evident. First of all, the values of  $c_{l0}$  and  $c_{s0}$  are different. The concentration boundary conditions used, therefore, are very important for the GeSi case. Fig. 5.3b shows explicitly that the used boundary conditions result in the right fraction of Si in the solid. Another detail, which attracts attention, is the large oscillation in  $\Theta$  in the transition region. There are corresponding oscillations on the  $c_l$  and  $c_s$  lines. This effect appeared in the NiCu results in the form of superheating in the transition region, Figs.4.6. This small effect becomes significant in the case of GeSi.

Let us discuss the influence of this effect on the model. The anti-double well potential, induced by this effect, exceeds the double-well potential. The result is the destruction of the transition region.

The only possible antidote is an increase in the amplitude of the double well potential. The Eq. (4.41) requires that we both increase the value of  $\xi_S$ , and leave  $\delta$  unchanged. Such an increase results in an increase in the surface tension. Thus, there is a stability restriction on the surface tension in the classic phase-field model. In this simulation, the surface energy  $\gamma = 210 \text{ J/m}^2$  is 1000 times larger than that in, Table 5.3. The increase in surface energy has no influence in the 1D simulation, since there is no Gibbs-Thomson effect in the 1D case. But in a 2D simulation, such an increase becomes problematic. The dual role of surface tension in the classic phase-field model has been discussed in Section 3.2. The modified phase-field model makes possible stable simulations with a realistic value for the surface tension. In the modified phase-field model, the stability restriction is only on the values of  $W$  and  $\xi_{\perp}$ , and there is no restriction on the value of  $\xi_{\parallel}$ , which is responsible for surface tension, see Eq. (3.16).

## 5.4 Simulation without flow

Some vagueness concerning values of material parameters has already been discussed in the beginning of this chapter. One such parameter is the diffusion coefficient of Si in Ge melt. As was mentioned earlier, two sources give different values for this parameter; we decided to make computations with the two different values. Again, as was discussed earlier, the knowledge of the process parameters in the vicinity of the interface is limited as well. Namely, there are no measurements for the temperature gradient. In our simulation, we took the value obtained in the simulation made by Smirnova et al. [56],  $G_t = 900 \text{ K/m}$ . We should say in advance

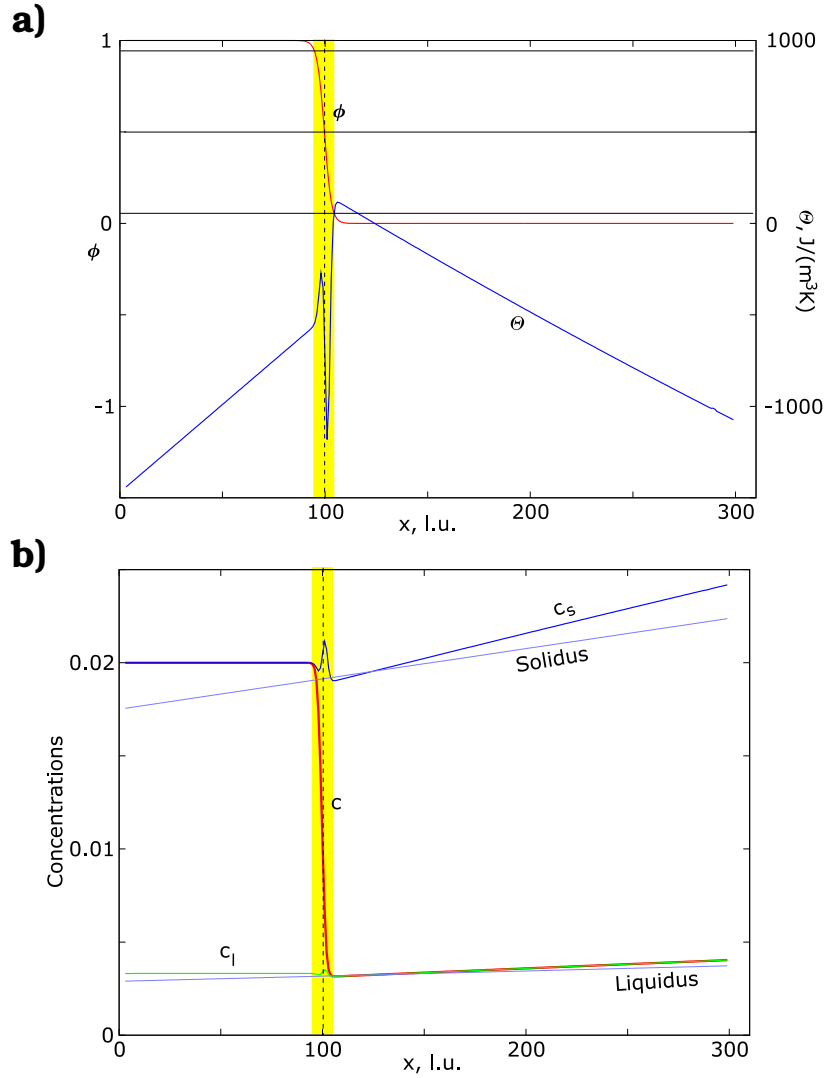


**Figure 5.3:** 1D simulation for GeSi. The vertical dashed line marks the interface position. The transition region is marked in yellow.  $\delta_x = 5 \cdot 10^{-6}$  m,  $\delta_t = 2 \cdot 10^{-2}$  s,  $l_y = 300\delta_x$ ,  $x_0 = 100\delta_x$ . **a:** Profile of phase-field  $\phi$  and supersaturation  $\Theta$ . **b:** Concentration profile  $c$ , separation of concentration in different phases and equilibrium concentrations (liquidus, solidus).

**Table 5.3:** Material parameters for Si and Ge [15]

Physical value	Si	Ge
Melting-point temperature	1693.15 K	1210.35 K
Latent heat	50.190 $\frac{\text{kJ}}{\text{mol}}$	34.02 $\pm$ 0.84 $\frac{\text{kJ}}{\text{mol}}$
Molar volume	1.2 $\cdot$ 10 <sup>-5</sup> $\frac{\text{m}^3}{\text{mol}}$	1.35 $\cdot$ 10 <sup>-5</sup> $\frac{\text{m}^3}{\text{mol}}$
Heat capacity	1300 K: 27.5 $\frac{\text{J}}{\text{mol K}}$ , 1693K: 28.5 $\frac{\text{J}}{\text{mol K}}$	25.0 $\frac{\text{J}}{\text{mol K}}$
Latent heat per unit volume	4.18 $\cdot$ 10 <sup>9</sup> $\frac{\text{J}}{\text{m}^3}$	(2.5 $\pm$ 0.06) $\cdot$ 10 <sup>9</sup> $\frac{\text{J}}{\text{m}^3}$
Heat capacity per unit volume	1300K: 2.29 $\cdot$ 10 <sup>6</sup> $\frac{\text{J}}{\text{m}^3 \text{K}}$ , 1693 K: 2.38 $\cdot$ 10 <sup>6</sup> $\frac{\text{J}}{\text{m}^3 \text{K}}$	1.85 $\cdot$ 10 <sup>6</sup> $\frac{\text{J}}{\text{m}^3 \text{K}}$
Kinetic coefficient	$\approx$ 0.63 $\frac{\text{m}}{\text{s K}}$	$\approx$ 0.32 $\frac{\text{m}}{\text{s K}}$
Gibbs-Thomson coefficient	6.72 $\cdot$ 10 <sup>-8</sup> m K	6.0 $\cdot$ 10 <sup>-8</sup> m K
Diffusion coefficient	3 $\cdot$ 10 <sup>-8</sup> $\frac{\text{m}^2}{\text{s}}$	6 $\cdot$ 10 <sup>-9</sup> $\frac{\text{m}^2}{\text{s}}$
Kinematic viscosity	2.8 $\cdot$ 10 <sup>-6</sup>	5 $\cdot$ 10 <sup>-7</sup> m <sup>2</sup> /s

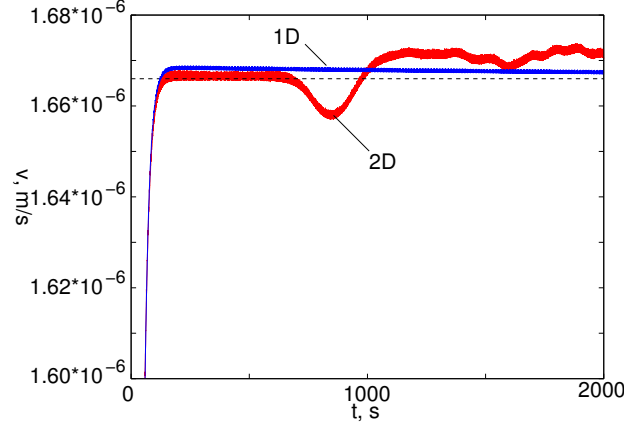


**Figure 5.4:** Time dependencies of growth velocity for 1D and 2D simulations of GeSi solidification.

that simulations with this value for the temperature gradient and with  $D = 3 \cdot 10^{-8} \text{ m}^2/\text{s}$  reproduce better experimental results than those with  $D = 6 \cdot 10^{-9} \text{ m}^2/\text{s}$ . The strong agreement of results, however does not permit the drawing of solid conclusions, due to the vagueness of other parameters. Further consideration shows computations with experimental value of  $D$  but some computations for  $D_{MD}$  are demonstrated, as well.

The simulated system is the same as that in the case of the NiCu solidification. Model parameters of GeSi require the use of the MRLK method. Contrary to the NiCu case, this method allows us to significantly speedup the GeSi simulations. For the flow-free case, the limiting factors for the numerics are  $D^*$  and  $\frac{\xi_S}{\tau} \frac{\delta_t}{\delta_x^2}$ . Their typical values for both systems are:

$$\text{NiCu : } \quad D^* = 0.03, \quad \frac{\xi_S}{\tau} \frac{\delta_t}{\delta_x^2} = 0.19 \text{ and}$$

$$\text{GeSi : } \quad D^* = 24.0, \quad \frac{\xi_S}{\tau} \frac{\delta_t}{\delta_x^2} = 0.19.$$

It is seen that  $D^*$  in the GeSi is far beyond the stability limit of the finite difference scheme. The simulation with the finite difference method therefore, requires time step,  $\delta_t$ , which is smaller than the one used with the MRLK method.

2D simulations with the parameters obtained from the global simulation, demonstrate that the shape of crystal is unstable. In Fig. 5.4 a comparison is made between the growth velocity of a flat interface (a 1D simulation) and that of a cellular interface (the velocity of a fixed point on the interface). Both velocity curves coincide at the initial stage since the 2D simulation starts from a flat interface. After some evolution, the growth velocity in the 2D simulation begins to deviate from the stationary behaviour. This occurs due to the progressive destruction of the flat interface. Appearing of a cellular structure causes an increase in growth velocity. In addition, the shape of the interface achieves a stationary state, where the growth velocity is eventually equal to the pulling one,  $v_{pull}$ . This figure demonstrates only the initial stage of the simulation.

Let us now discuss theoretical predictions for the size of patterns. The depth of the cells is related with the temperature gradient:

$$a_{cell} = \frac{T_{\Delta}}{G_T},$$

where  $T_{\Delta}$  is the temperature difference between the top and bottom parts of a cell. This temperature difference is assumed to be equal to  $T_{\Delta 0}(c_i^0)$  and, is defined through the phase-diagram as the difference between the temperatures of solidus and liquidus, see Fig. 5.2. In the GeSi simulation,  $T_{\Delta 0} = 4$  K and  $G_T = 0.9$  K/mm. The obtained value for the depth of the patterns is  $\approx 4.4$  mm. Fig. 5.5 shows a computed interface profile. The depth of the calculated structure is 4.2 mm, which has a good agreement with the theoret-

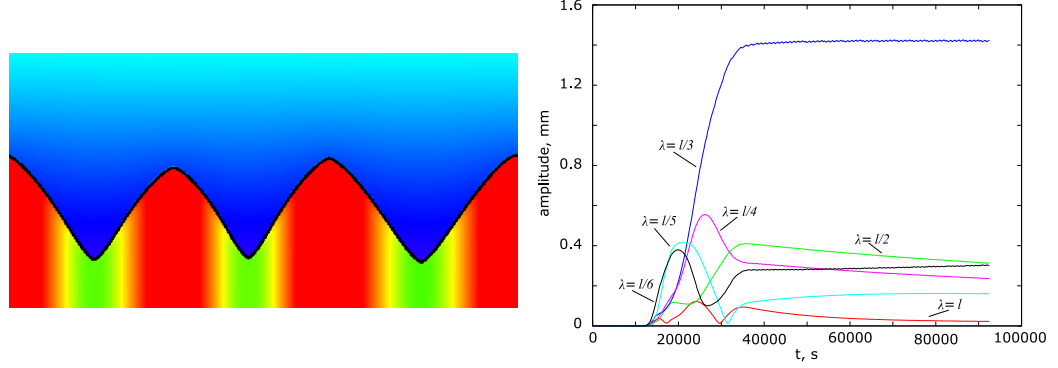


**Figure 5.5:** Modelling results of cellular structure in a GeSi crystal. Domain size  $10 \times 20$  mm,  $\delta_x = 0.02$  mm,  $\delta_t = 0.32$  s,  $\gamma_\xi^2 = 10^{-3}$ . **left:** Concentration field. Black line indicates a phase-boundary. The crystal solidifies from bottom to top. Color codes the Si concentration, the concentration in the crystal changes between 1.5% and 2.5%. **right:** Time evolution of the first six coefficients in the Fourier representation of the interface shape.

ical value. The distance between the nearest minima on the interface is defined by the shape of the patterns and tip radius. The relation between tip radius,  $R_{tip}$  and the wavelength,  $\lambda$ , is written for elliptic and parabolic shapes, respectively:

$$\lambda = 2\sqrt{\alpha_{sh} a_{cell} * R_{tip}}, \quad (5.2)$$

where  $\alpha_{sh}$  is the shape coefficient. It takes a value of 1 for the elliptic and 2 for the parabolic shape. The resulting expression for the tip radius is, (pg. 79 in [33]):

$$R_{tip} = 2\pi\sqrt{\frac{\Gamma D}{kv_{pull}T_{\Delta 0}}}. \quad (5.3)$$

The resulting expression for the wave length is:

$$\lambda = 2\sqrt{2\pi\alpha_{sh}}\sqrt[4]{\frac{T_{\Delta 0}\Gamma D}{kv_{pull}G_T^2}}, \quad (5.4)$$



In the case of a parabolic shape,  $\lambda \approx 6.3$  mm. Our simulation, Fig. 5.5, gives a value of 6.7 mm. Both, simulation and theory, result in similar sizes of the microstructure. This size is approximately 15 times larger than the experimental one. This effect can be explained by the presence of flow in the experiment (see the next section). Fig. 5.5(right) shows the spectrum of the patterns. It is seen that  $\lambda$  increases during the simulation. After a period of time, a shallow cellular structure appears. Observation of evolution processes allows one to make qualitative estimations of a time scale. It is easy to recognize the transition from high-frequency patterns at the beginning to lower ones.

In the simulation, it is seen that the cells grow parallel to the pulling velocity, however in the experiment there is some deviation from this direction. This deviation appears to be due to the existence of a tangential flow.

## 5.5 Influence of flow

The flow influence has already been described for the NiCu alloy, see Section 4.5.4. The impact of strong flow on cell orientations and on stability of patterns has been considered in Section 4.5.4. The goal is to study flow influence on the cell orientation. This effect has practical importance. It was mentioned earlier that in the experiment, the cell orientation deviates from the normal direction to the interface. This deviation indicates an existence of a flow near the interface.

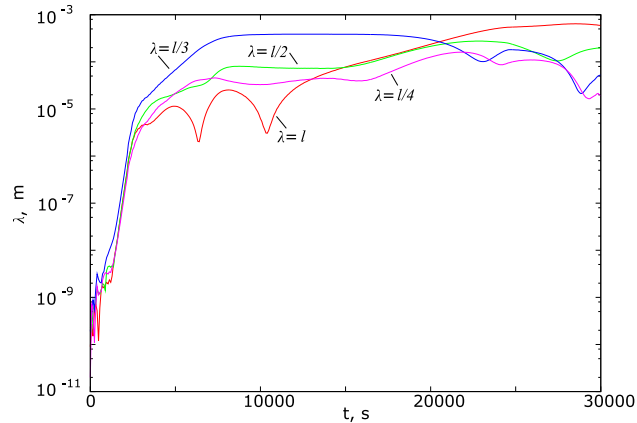


**Figure 5.6:** Time evolution of first four coefficients in the Fourier representation of the interface form. The solidification is influenced by tangential flow,  $u_t = 0.2$  mm/s,  $l = 5$  mm is width of the domain. Domain size of  $3 \times 5$  mm,  $\delta_x = 1 \cdot 10^{-5}$  m,  $\delta_t = 4 \cdot 10^{-3}$  s,  $\gamma_\xi^2 = 10^{-3}$ .

### 5.5.1 Stability of cellular structure

An interesting flow effect was observed during this investigation. In the case without flow, an increase in the value of dominant wavelengths is seen in Fig. 5.5. This situation changes in the presence of flow. Fig. 5.6 shows the Fourier representation of the growing surface. This plot is a result of modelling with tangential flow. The flow is too weak to have an impact on the cell orientation, but it makes an influence on the wavelength pattern. The plot shows that the cell size of 1.7 mm became quasi-stable in the presence of flow. This effect is a good explanation of the experimentally observed small size of the cells, see Fig. 1.5.

Other simulations were carried out with a stronger flow. Figs. 5.7 show the evolution of the interface for different values of flow velocity. It is seen that for slower flow the wave length continuously increases (on this scale), but with faster flow it becomes

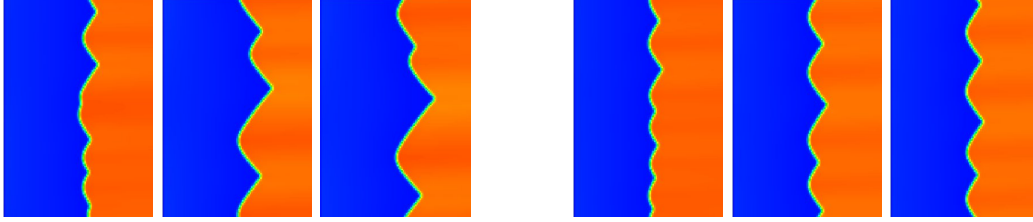


**Figure 5.7:** Concentration and phase-boundary for GeSi crystal. Crystal grows from right to left. Domain size of  $1 \text{ mm} \times 1.5 \text{ mm}$ ,  $x_0 = 1 \text{ mm}$ ,  $\delta_x = 5 \cdot 10^{-6} \text{ m}$ ,  $\delta_t = 2 \cdot 10^{-3} \text{ s}$ ,  $\gamma_\xi^2 = 10^{-3}$ ,  $D = 3 \cdot 10^{-8} \text{ m}^2/\text{s}$ . Screenshots correspond to 4000 s, 80000 s and 10000 s. **left:**  $u_t = 1 \text{ mm/s}$ ; **right:**  $u_t = 1.5 \text{ mm/s}$ .

constant after some evolution. The simulation corresponding to Fig. 5.7(right) shows that the stationary structure is achieved after approximately 2 h. During this time the crystal grows up to 12 mm. We can not give a clear answer as to whether the structure, shown in Fig. 5.7(left), is stable or quasi-stable, nevertheless, such a question is irrelevant from the experimental point of view. The crystal analysis shows fluctuations with a period of  $\sim 1 \text{ h}$ . This means that processes with a time scale larger than 1 h, can be considered stationary.

### 5.5.2 Growth orientation of cells

Let us turn back to the investigation of the influence of flow on the cell orientation. A series of interface profiles, corresponding to Fig. 5.7 right, is plotted in Fig. 5.8. The cellular structure is clearly observed, it does not change with time and may thus be considered to be in a stationary state. This state is achieved after 2.5 h. Tip traces are marked with black lines. The lines are tilted to the growth direction with an angle of  $1.7^\circ$ . The dependence of this angle on the flow velocity is plotted in Fig. 5.12. This dependence

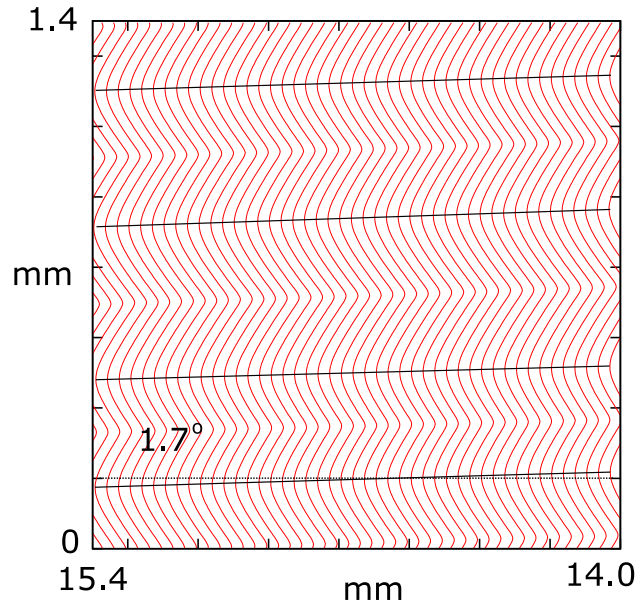


**Figure 5.8:** Evolution dynamic of the interface. The thin black lines indicate traces of the cell tips and the thick line marks the growth direction. Domain size of  $1 \text{ mm} \times 1.5 \text{ mm}$ ,  $x_0 = 1 \text{ mm}$ ,  $\delta_x = 5 \cdot 10^{-6} \text{ m}$ ,  $\delta_t = 2 \cdot 10^{-3} \text{ s}$ ,  $\gamma_{\xi}^2 = 10^{-3}$ ,  $D = 3 \cdot 10^{-8} \text{ m}^2/\text{s}$ ,  $u_t = 1.5 \text{ mm/s}$ .

is linear, similar to that obtained in the NiCu results.

Simulations show that the orientation angle depends on the cell amplitude. This effect appears because of the slow transition from one wave-length to another. Fig. 5.9 shows the simulation with  $D = 6 \cdot 10^{-9} \text{ m}^2/\text{s}$ . A series of the crystal surfaces is plotted here. Evolution of the cellular structure is clearly seen in this figure. During the growth, the orientation angle increases. The tip trace here is not a straight line, but rather a curve, contrary to the tip trace in Fig. 5.8. The time scale of the transition from one wave-length to the next is about of 5 min. This time scale is large in comparison with flow and diffusion time scales. The evolution is slow enough therefore, and we are able to observe the influence of

the flow on the different cellular structures which appear during the evolution. Differences in the influence can be explained with the help of the sketch in Fig. 5.10. It is seen that the periodic structure with a small period and amplitude interacts weaker with a flow than the structure with large period.

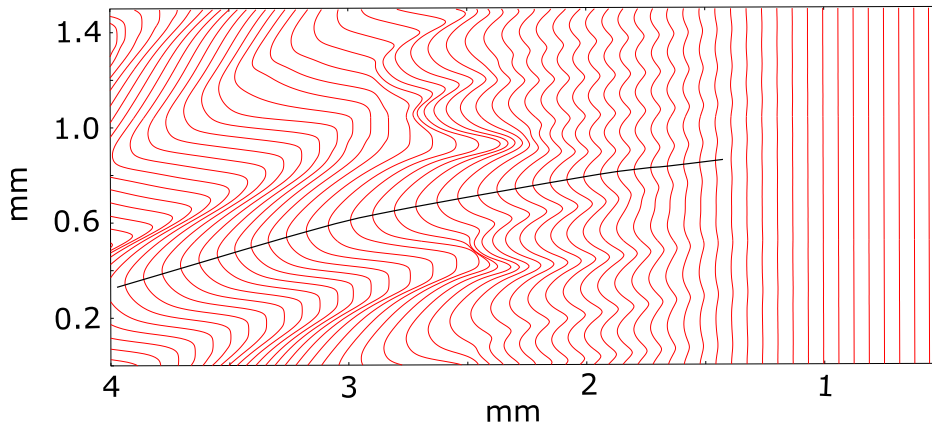


**Figure 5.9:** Evolution of the interface. The thick line marks the trace of a cell tip. The crystal grows from right to left. Melt flows from bottom to top.  $D = 6 \cdot 10^{-9} \text{ m}^2/\text{s}$ ,  $u_t = 1.1 \text{ mm/s}$ .

The flow and amplitude effects are measured for the decreased  $D$ , and the results are plotted in Fig. 5.11. Measurements have been done for two different amplitudes. The orientation angle is averaged between all the cells on the plot. The bottom line corresponds to the measurements for the patterns whose height is less than 0.1 mm. The other line corresponds to the later period of time with a value of amplitude between 0.1 mm and 0.2 mm. The dependence of cell orientation on the flow velocity seems to be linear, similarly to the NiCu case. Please note that there were no stationary patterns achieved, contrary to the simulations with the experimental value of the diffusion coefficient.

The results for  $D = 3 \cdot 10^{-8} \text{ m}^2/\text{s}$  are plotted in Fig. 5.12. It is

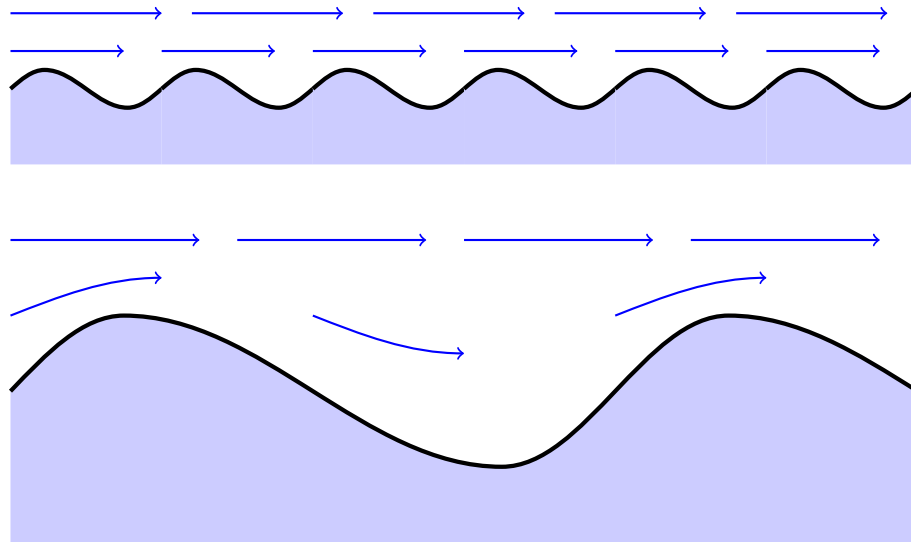


**Figure 5.10:** Schematic representation of cellular interface with flow field for different periods of the structure.

seen that the influence of the flow is significantly smaller than in the previous case. Another observation is that the appearing and development of the cellular structure are sufficiently slower in the presence of flow. For different amplitudes of cells, we measured dependence of cell orientation on the flow. The maximal amplitude is 0.083 mm, this amplitude corresponds to stationary state (all plotted simulations). The bottom line corresponds to an intermediate state with the cells amplitude of less than 0.04 mm.

Fig 5.13 shows modelling results vs. real crystal. The vertical cut from a grown crystal is shown. Striations which show advancing of the interface, exhibit cellular structure. The simulation is made for a velocity value of 2 mm/s. Interfaces in both the simulation and the experiment evaluate from the initially flat shape. The appearing cellular structures reduce their frequency during

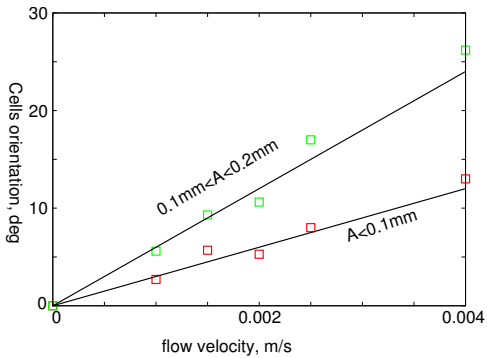


**Figure 5.11:** Dependence of cell orientation on the melt flow. The direction is measured for different amplitudes “A” of the patterns.  $D = 6 \cdot 10^{-9} \text{ m}^2/\text{s}$

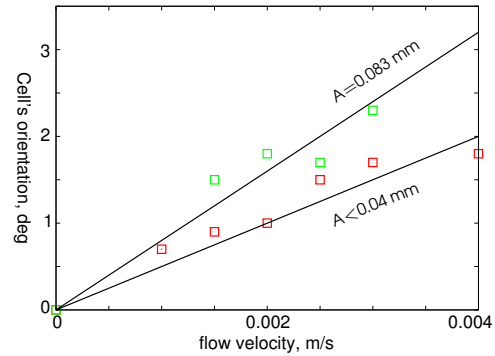


**Figure 5.12:** Dependence of cell orientation on the melt flow. The direction is measured for different amplitudes “A” of the patterns.  $D = 3 \cdot 10^{-8} \text{ m}^2/\text{s}$

the evolution. The observed wavelengths and evolution rates are in good qualitative agreement. Nevertheless the orientation of the cells is different in the experiment from that in the simulation. We assume this difference to be caused by a difference in the crystallographic anisotropy. Namely, the growth direction in the simulation is  $\langle 100 \rangle$  and that in the experiment is  $\langle 112 \rangle$ . In this work, growth in different crystallographic directions were not studied. Fig. 5.14 shows part of the crystal cross section. There are three marked cell traces. The analysis of these traces provides information about flow near the interface. Cells in the central part of the crystal grow without flow (the value of the flow velocity averaged in time equals 0). The orientation of these cells is a result of the influence of crystallographic anisotropy. Flow influence is therefore characterized by local cell orientation as compared to that of the central cells. The measured dependence of the orientation an-

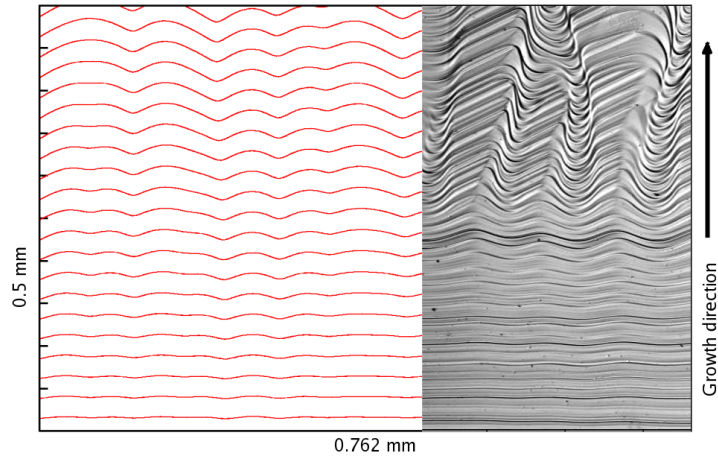


**Figure 5.13:** Comparison of the crystal shapes predicted in the simulation and those obtained in the experiment

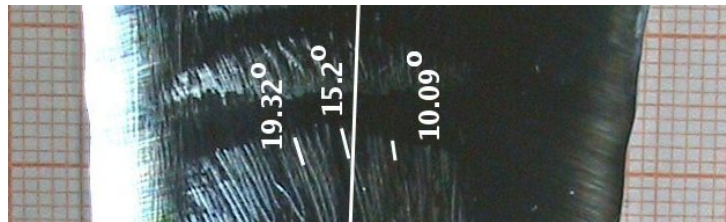


**Figure 5.14:** Cut from the cross section of a GeSi crystal. The crystal rotation axis is marked. Three cell traces are marked with white lines. Angles between the rotation axis and these traces are noted.

gle on melt flow, see Fig. 5.12, gives the value of flow velocity of  $\approx 6.3$  mm/s on the distance from the interface of 1 mm. Similar value was obtained in the macroscopic simulation of the growth furnace, see [56].



# Chapter 6

## Conclusion

The pattern formation during the Czochralski growth of GeSi crystals was studied in this work. Simulations for GeSi raised numerous problems. The model contains a large number of physical effects which should be coupled together: melt flow, diffusion in a melt, phase-transition in a binary alloy. Each physical effect has its own space and time-scale. Therefore, it is important to develop a numerical technique which is able to treat such a multi-scale model. During the work on the numerical model we made significant updates in both the phase-field method and the numerical methods. The calculations with the model were performed for simulations of solidification in NiCu and GeSi alloys. The expected instability of the growing interface was obtained in simulations. Modelling results were compared with theoretical predictions and experimental measurements. The effect of flow influence on the solidification patterns has been investigated.

For the modelling of the advection-diffusion processes we have chosen a method of the Lattice-Boltzmann type. In order to apply this type of methods to our model we have developed a matrix

kinetic scheme. The matrix kinetic scheme has numerous advantages. The time step for this method is free of diffusive Courant constraints. It can handle anisotropic diffusion, which is, by definition, out of reach for single-time relaxation kinetic schemes. It achieves all of the above without introducing any memory overhead, as compared to existing kinetic schemes. We developed the time-stepping technique for the Lattice-Boltzmann type of methods. This update increase significantly the performance of this type of methods. The new schemes were tested and verified with a pure diffusion problem.

Afterwards, the matrix kinetic scheme has been coupled with phase-field equations for the solidification of pure materials. The phase-field model for binary alloys contains a non-linear reaction-diffusion equation. In order to apply this method for the case of binary alloys we have introduced an extension of the kinetic scheme for this type of equations. The coupled schemes have been validated for a variety of growth phenomena: 2D and 3D dendritic growth from melt, and directional solidification in binary alloys.

A modified phase-field equation has been developed. The development was a result of the GeSi problem; the classic phase-field equation for binary alloys becomes unstable for large scales and this instability appeared in the GeSi case. The modification allows to treat separately the surface tension effect and the phase-transition region. This modification increases the stability of the phase-field model for cases with the small surface-tension.

Binary alloy simulations were based on the KKS phase-field model. The combination of this model with the mentioned modified phase-field equation was tested on the NiCu alloy. Our results were compared with those of other papers based on the WBM

phase-field model.

The phase-field model has been coupled with the LBGK model in order to perform simulations with flow. The influence of convection has been investigated and a flow impact on the cell orientation was observed. A linear dependence of the slope angle on the flow velocity was obtained.

The developed numerical model was applied for simulations of the GeSi case.

The influence of different physical values on the evolution of the cellular structure such as temperature gradient, growth velocity and surface tension anisotropy was studied.

The modified phase-field equation that we used allowed us to apply a coarser grid, and the use of the kinetic method removed the limitations on the time step. Therefore, simulations with realistic parameters taken from measurements or from a global simulation of the Czochralski furnace have been possible with reasonable computational efforts.

Simulations without flow were compared with the theory. The simulation with typical parameters gives the value of wavelength of 6.7 mm which is in good agreement with the theoretical value of 6.3 mm. These values are  $\approx 15$  times larger than the experimentally observed one. A strong impact of flow on the wavelength was observed in GeSi modelling. In the presence of flow, the cell size decreases. For example, the same simulation but with a flow velocity of  $1.5 \frac{\text{mm}}{\text{s}}$  gives a value of the wavelength which is equal to 0.37 mm. As in the case of NiCu a linear dependence of cell on the flow velocity was observed. This fact can be used as an indirect method of measurement of the flow velocity near the crystal interface. This method is based on the analysis of striations in the grown crys-

tal which provides information about flow velocity and direction of flow near the interface.

# Appendix A

## Thermodynamically consistent PF model

### A.1 Common equations

In the phase-field model the state of matter is characterized by a continuous order parameter,  $\phi$ .  $\phi$  is defined as 0 in the liquid phase (melt) and 1 in the solid phase (crystal). A free energy function  $\mathcal{F}$  can be introduced for a system with two phases:

$$\mathcal{F} = \int_V \left( f(\phi, T) + \frac{\xi_F^2}{2} |\vec{\nabla} \phi|^2 \right) dV, \quad (\text{A.1})$$

where  $f(\phi, T)$  is the free energy density function of a homogeneous system and  $\xi_F$  is the model parameter. The second term corresponds to the interface energy. It is also necessary to introduce an internal energy:

$$\mathcal{E} = \int_V e(\phi, T) dV, \quad (\text{A.2})$$

where  $e(\phi, T)$  is the internal energy density function. The internal energy is a conserved value in the case of a closed system:

$$\frac{\partial \mathcal{E}}{\partial t} = 0. \quad (\text{A.3})$$

The considered system corresponds to “Model C” of Halperin [22].

The thermodynamically consistent phase-field model of the non-isothermal case was constructed by O. Penrose and P.C. Fife [44] and separately by Wang et al. [66]. The free energy density is obtained from the energy density  $e$  and the entropy density via the Legendre transformation:

$$f(\phi, T) = e - Ts(\phi, e). \quad (\text{A.4})$$

By substituting this expression in (A.1) we get:

$$\mathcal{F} = \int_V \left( e - Ts(\phi, e) + \frac{\xi_F^2}{2} |\vec{\nabla} \phi|^2 \right) dV = \mathcal{E} - T\mathcal{S}, \quad (\text{A.5})$$

$$\mathcal{S} = \int_V \left( s(\phi, e) - \frac{\xi_S^2}{2} |\vec{\nabla} \phi|^2 \right) dV, \quad (\text{A.6})$$

where  $\xi_S^2 \equiv \xi_F^2/T$ .

The evolution equations for  $\phi$  and  $e$  can be taken in the following form [22]:

$$\frac{\partial \phi}{\partial t} = M_\phi \frac{\delta \mathcal{S}}{\delta \phi}, \quad (\text{A.7})$$

$$\frac{\partial e}{\partial t} = -\vec{\nabla} \cdot \left( M_e \vec{\nabla} \frac{\delta \mathcal{S}}{\delta e} \right). \quad (\text{A.8})$$

These equations uphold the law of energy conservation and the second law of thermodynamics. Substitution of the entropy expression (A.6) in these equations gives:

$$\frac{\partial \phi}{\partial t} = M_\phi \left( \frac{\partial s}{\partial \phi} + \xi_S^2 \Delta \phi \right), \quad (\text{A.9})$$

$$\frac{\partial e}{\partial t} = -\vec{\nabla} \cdot \left( M_e \vec{\nabla} \frac{\partial s}{\partial e} \right). \quad (\text{A.10})$$

## A.2 Governing equations

The following equations for the derivatives of the entropy density hold:

$$\frac{\partial s(\phi, e)}{\partial e} = \frac{1}{T}, \quad (\text{A.11})$$

$$\frac{\partial s(\phi, e)}{\partial \phi} = -\frac{1}{T} \frac{\partial f(\phi, T)}{\partial \phi}. \quad (\text{A.12})$$

With these relations, the kinetic equations (A.9) and (A.10) can be transformed:

$$\frac{\partial \phi}{\partial t} = M_\phi \left( -\frac{1}{T} \frac{\partial f}{\partial \phi} + \xi_S^2 \Delta \phi \right), \quad (\text{A.13})$$

$$\frac{\partial e}{\partial t} = -\vec{\nabla} \cdot \left( M_e \vec{\nabla} \frac{1}{T} \right). \quad (\text{A.14})$$

The standard temperature conductivity equation is derived by choosing  $M_e = K(\phi)T^2$  in (A.14):

$$\frac{\partial e}{\partial t} = \vec{\nabla} \cdot (K(T) \vec{\nabla} T). \quad (\text{A.15})$$

The internal energy density function  $e$  can be represented by the expression:

$$e = Tc_p(\phi, T) - L(T)p(\phi), \quad (\text{A.16})$$

where  $c_p(\phi, T)$  is the heat capacity,  $L(T)$  is the latent heat and  $p(\phi)$  describes the character of the latent heat production during the phase transition. It is a monotone increasing function with values 0 and 1 on the ends of the interval. The expression (A.16) for  $e$  is common. Thus, the resulting expression for  $e$  is:

$$e = Tc_p - Lp(\phi). \quad (\text{A.17})$$

The relation between  $e$  and  $f$  can be obtained from the Legendre transformation for  $f$  (A.4):

$$e = \frac{\partial f(\phi, T)/T}{\partial(1/T)}. \quad (\text{A.18})$$

The expression for the free energy density function  $f$  is obtained now from the relation (A.18):

$$f = T \int_{T_m}^T (T c_p - Lp(\phi)) d(T^{-1}) - T s_0(\phi) = c_p T \ln \frac{T_m}{T} - Lp(\phi) T Q(T) - T s_0(\phi), \quad (\text{A.19})$$

where

$$Q(T) = \frac{1}{T} - \frac{1}{T_m} \approx \frac{1}{T_m^2} (T_m - T). \quad (\text{A.20})$$

By using the equations (A.13), (A.15), (A.17) and (A.19) we factorize the corresponding kinetic equations for temperature and phase-field.

$$\frac{\partial \phi}{\partial t} = M_\phi \left( \xi_S^2 \Delta \phi + s_{0\phi} + Lp_\phi Q(T) \right), \quad (\text{A.21})$$

$$c_p \frac{\partial T}{\partial t} = \vec{\nabla} \cdot (K(T) \vec{\nabla} T) + Lp_\phi \frac{\partial \phi}{\partial t}, \quad (\text{A.22})$$

where

$$p_\phi \equiv \frac{\partial p(\phi)}{\partial \phi}, \quad s_{0\phi} \equiv \frac{\partial s_0(\phi)}{\partial \phi}.$$

Here,  $s_0(\phi)$  is an arbitrary function. Usually,  $s_0$  is taken in the form of double-well potential, with two minima in pure phases:

$$s_0 = -W g(\phi), \quad g(\phi) \equiv \phi^2 (1 - \phi)^2. \quad (\text{A.23})$$

$p(\phi)$  is chosen in a polynomial form:

$$p(\phi) = 30 \left( \frac{\phi^3}{3} - \frac{\phi^4}{2} + \frac{\phi^5}{5} \right). \quad (\text{A.24})$$

This form of  $p(\phi)$  assures the minima of free energy in points 0 and 1 for all values of the undercooling. Although it is possible to take polynomials of lower order, these forms do not possess this property and it can be a cause of instability.  $M_\phi$  is taken as a constant  $M_\phi = \frac{1}{\tau}$ . The resulting equations are:

$$\tau \frac{\partial \phi}{\partial t} = \xi_S^2 \Delta \phi - W g_\phi + Lp_\phi Q(T), \quad (\text{A.25})$$

$$c_p \frac{\partial T}{\partial t} = \vec{\nabla} \cdot (K(T) \vec{\nabla} T) + Lp_\phi \frac{\partial \phi}{\partial t}. \quad (\text{A.26})$$



The Eq.(A.25) can be rewritten for the case with small undercooling,  $Q(T) \approx \frac{T-T_m}{T_m^2}$ , and the constant temperature conductivity is  $K(T) = K_0$ :

$$\tau \frac{\partial \phi}{\partial t} = \xi_S^2 \Delta \phi - W g_\phi + \frac{L}{T_m^2} p_\phi (T - T_m), \quad (\text{A.27})$$

$$c_p \frac{\partial T}{\partial t} = K_0 \Delta T + L p_\phi \frac{\partial \phi}{\partial t}. \quad (\text{A.28})$$

## Appendix B

# Solution of the diffusion equation for special problem

In order to verify the proposed numerical method, we tested it on a pure-diffusion problem. The diffusion equation looks like:

$$\frac{\partial c}{\partial t} = D\Delta c. \quad (\text{B.1})$$

The simplest test is to start with a Gauss distribution:

$$c = \rho_0 \left( \frac{N_d}{2\pi\sigma_0^2} \right)^{N_d/2} e^{-\frac{|\vec{r}|^2 N_d}{2\sigma_0^2}}, \quad (\text{B.2})$$

where  $\rho_0$  is initial mass and  $\sigma_0$  is initial dispersion. This problem has an analytical solution:

$$c = \rho_0 \left( \frac{N_d}{2\pi\sigma^2} \right)^{N_d/2} e^{-\frac{|\vec{r}|^2 N_d}{2\sigma^2}}, \quad \sigma = \sqrt{\sigma_0^2 + 2N_d D t}.$$

# Appendix C

## Local curvature

In this Appendix, a question about curvature of surface is discussed. The surface is defined by this equation:

$$F(x, y, z) = \text{Const.}$$

The curvature of a surface is defined by its first and second fundamental forms. The expressions for the first fundamental forms are:

$$E = (\partial_u x)^2 + (\partial_u y)^2 + (\partial_u z)^2, \quad (\text{C.1})$$

$$F = (\partial_u x)(\partial_v x) + (\partial_u y)(\partial_v y) + (\partial_u z)(\partial_v z), \quad (\text{C.2})$$

$$G = (\partial_v x)^2 + (\partial_v y)^2 + (\partial_v z)^2, \quad (\text{C.3})$$

where  $u$  and  $v$  are surface parameters. The expressions of the second fundamental forms are:

$$L = \frac{1}{\sqrt{EG - F^2}} \begin{vmatrix} \partial_{uu}x & \partial_{uu}y & \partial_{uu}z \\ \partial_u x & \partial_u y & \partial_u z \\ \partial_v x & \partial_v y & \partial_v z \end{vmatrix}, \quad (\text{C.4})$$

$$M = \frac{1}{\sqrt{EG - F^2}} \begin{vmatrix} \partial_{uv}x & \partial_{uv}y & \partial_{uv}z \\ \partial_u x & \partial_u y & \partial_u z \\ \partial_v x & \partial_v y & \partial_v z \end{vmatrix}, \quad (\text{C.5})$$

$$N = \frac{1}{\sqrt{EG - F^2}} \begin{vmatrix} \partial_{vv}x & \partial_{vv}y & \partial_{vv}z \\ \partial_u x & \partial_u y & \partial_u z \\ \partial_v x & \partial_v y & \partial_v z \end{vmatrix}. \quad (\text{C.6})$$

The curvature  $\kappa$  is related to the differential forms through the following formula:

$$\kappa = \frac{EN - 2FM + GL}{EG - F^2}. \quad (\text{C.7})$$

In order to simplify the calculations,  $x$  and  $y$  are taken to parametrise a surface,  $u = x$ ,  $v = y$ . This choice gives the following expressions for the coordinate derivatives:

$$\partial_u x = 1, \quad \partial_u y = 0, \quad \partial_u z = -\frac{\partial_x F}{\partial_z F}, \quad (\text{C.8})$$

$$\partial_v x = 0, \quad \partial_v y = 1, \quad \partial_v z = -\frac{\partial_y F}{\partial_z F}. \quad (\text{C.9})$$

the second derivatives of  $z$  with respect to  $x$  and  $y$  are:

$$\begin{aligned} \partial_{uu}z &= -\frac{\partial_{xx}F(\partial_z F)^2 - 2\partial_{xz}F\partial_x F\partial_z F + \partial_{zz}F(\partial_x F)^2}{(\partial_z F)^3}, \\ \partial_{uv}z &= -\frac{\partial_{xy}F(\partial_z F)^2 - \partial_{xz}F\partial_y F\partial_z F - \partial_{yz}F\partial_x F\partial_z F + \partial_{zz}F\partial_x F\partial_y F}{(\partial_z F)^3}, \\ \partial_{vv}z &= -\frac{\partial_{yy}F(\partial_z F)^2 - 2\partial_{yz}F\partial_y F\partial_z F + \partial_{zz}F(\partial_y F)^2}{(\partial_z F)^3}. \end{aligned}$$

Now we are able to write expressions for the fundamental forms in terms of the new variables:

$$\begin{aligned} E &= 1 + \frac{(\partial_x F)^2}{(\partial_z F)^2}, \\ F &= \frac{\partial_x F \partial_y F}{(\partial_z F)^2}, \end{aligned}$$

$$\begin{aligned}
G &= 1 + \frac{(\partial_y F)^2}{(\partial_z F)^2}, \\
L &= -\frac{\partial_{xx} F (\partial_z F)^2 - 2\partial_{xz} F \partial_x F \partial_z F + \partial_{zz} F (\partial_x F)^2}{(\partial_z F)^2 |\vec{\nabla} F|}, \\
M &= -\frac{\partial_{xy} F (\partial_z F)^2 - \partial_{xz} F \partial_y F \partial_z F - \partial_{yz} F \partial_x F \partial_z F + \partial_{zz} F \partial_x F \partial_y F}{(\partial_z F)^2 |\vec{\nabla} F|}, \\
N &= -\frac{\partial_{yy} F (\partial_z F)^2 - 2\partial_{yz} F \partial_z F \partial_y F + \partial_{zz} F (\partial_y F)^2}{(\partial_z F)^2 |\vec{\nabla} F|}.
\end{aligned}$$

These expressions and the Eq.(C.7) lead to the following formula for the curvature of an isosurface:

$$\kappa = \frac{\Delta F - n_\alpha n_\beta \nabla_\alpha \nabla_\beta F}{|\vec{\nabla} F|}, \quad (\text{C.10})$$

where  $n_\alpha \equiv \frac{\nabla_\alpha F}{|\vec{\nabla} F|}$ .

# Appendix D

## Finite difference schemes

### D.1 Properties of the lattice vectors

#### D.1.1 The 2D case

All computations are made on a rectangular grid. The lattice vectors for the 2D case are:

$$\begin{aligned}\vec{a}_0 &= (0, 0), \\ \vec{a}_1 &= (1, 0), \quad \vec{a}_2 = (0, 1), \quad \vec{a}_3 = (-1, 0), \quad \vec{a}_4 = (0, -1), \\ \vec{a}_5 &= (1, 1), \quad \vec{a}_6 = (-1, 1), \quad \vec{a}_7 = (-1, -1), \quad \vec{a}_8 = (1, -1).\end{aligned}\tag{D.1}$$

For further consideration of differential operators it is useful to list some properties of these vectors:

$$\begin{aligned}\sum_{i=0}^8 w_i a_{i\alpha} &= 0, \\ \sum_{i=0}^8 w_i a_{i\alpha} a_{i\beta} &= 2(w_+ + 2w_\times) \delta_{\alpha\beta}, \\ \sum_{i=0}^8 w_i a_{i\alpha} a_{i\beta} a_{i\gamma} &= 0, \\ \sum_{i=0}^8 w_i a_{i\alpha} a_{i\beta} a_{i\gamma} a_{i\delta} &= 4w_\times (\delta_{\alpha\beta} \delta_{\gamma\delta} + \delta_{\alpha\gamma} \delta_{\delta\beta} + \delta_{\alpha\delta} \delta_{\gamma\beta}) \\ &\quad + 2(w_+ - 4w_\times) \delta_{\alpha\beta\gamma\delta},\end{aligned}\tag{D.2}$$

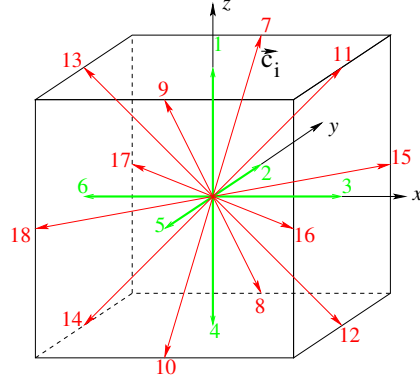


**Figure D.1:** Lattice vectors for the 3D case.

where  $w_i$  are the weight coefficients. The coefficients taken for orthogonal and diagonal directions are different:

$$w_i = \begin{cases} w_+, & i = 1..4 \\ w_\times, & i = 5..8 \end{cases}$$

### D.1.2 The 3D case

Lattice vectors for the 3D case are plotted in Fig.D.1. Their coordinates are:

$$\begin{aligned}
 \vec{a}_0 &= (0, 0, 0), \\
 \vec{a}_1 &= (0, 0, 1), & \vec{a}_2 &= (0, 1, 0), & \vec{a}_3 &= (1, 0, 0), \\
 \vec{a}_4 &= (0, 0, -1), & \vec{a}_5 &= (0, -1, 0), & \vec{a}_6 &= (-1, 0, 0), \\
 \vec{a}_7 &= (0, 1, 1), & \vec{a}_8 &= (0, 1, -1), & \vec{a}_9 &= (0, -1, 1), \\
 \vec{a}_{10} &= (0, -1, -1), & \vec{a}_{11} &= (1, 0, 1), & \vec{a}_{12} &= (1, 0, -1), \\
 \vec{a}_{13} &= (-1, 0, 1), & \vec{a}_{14} &= (-1, 0, -1), & \vec{a}_{15} &= (1, 1, 0), \\
 \vec{a}_{16} &= (1, -1, 0), & \vec{a}_{17} &= (-1, 1, 0), & \vec{a}_{18} &= (-1, -1, 0),
 \end{aligned} \tag{D.3}$$

The list of vector properties is similar to that of the 2D lattice:

$$\begin{aligned}
\sum_{i=0}^{18} w_i a_{i\alpha} &= 0, \\
\sum_{i=0}^{18} w_i a_{i\alpha} a_{i\beta} &= 2(w_+ + 4w_\times) \delta_{\alpha\beta}, \\
\sum_{i=0}^{18} w_i a_{i\alpha} a_{i\beta} a_{i\gamma} &= 0, \\
\sum_{i=0}^{18} w_i a_{i\alpha} a_{i\beta} a_{i\gamma} a_{i\delta} &= 4w_\times (\delta_{\alpha\beta} \delta_{\gamma\delta} + \delta_{\alpha\gamma} \delta_{\delta\beta} + \delta_{\alpha\delta} \delta_{\gamma\beta}) + \\
&\quad 2(w_+ - 2w_\times) \delta_{\alpha\beta\gamma\delta}.
\end{aligned} \tag{D.4}$$

## D.2 Differential operators

Some expressions of discretized differential operators are listed in this section.

### D.2.1 The 2D case

The five- and nine-point templates are taken for the 2D case. Reduction of an additional numerical anisotropy was mainly considered in the case of a nine-point template, [26]. Discretization of the Laplace operator is:

$$\Delta\phi = \sum_i \alpha_{\Delta i} \phi_i. \tag{D.5}$$

The Taylor expansion of the right side of the previous expression with the second order accuracy is:

$$\begin{aligned}
\sum_i \alpha_{\Delta i} \phi_i &= \phi \sum_i \alpha_{\Delta i} + \frac{1}{2} \nabla_\alpha \nabla_\beta \phi \sum_i \alpha_{\Delta i} a_{\alpha i} a_{\beta i} \\
&\quad + \frac{1}{4!} \nabla_\alpha \nabla_\beta \nabla_\gamma \nabla_\delta \phi \sum_i \alpha_{\Delta i} a_{\alpha i} a_{\beta i} a_{\gamma i} a_{\delta i} + \dots
\end{aligned}$$

The properties of the lattice vectors provide both the expression of the coefficients and the ratio of the coefficients for orthogonal and diagonal directions.



**Table D.1:** Weight coefficients for different templates, the 2D case

	5-point	9-point
$\alpha_{\Delta i}$	$-4, i = 0; 1, i = 1..4$	$-\frac{10}{3}, i = 0; \frac{2}{3}, i = 1..4; \frac{1}{6}, i = 5..8$
$\alpha_{\nabla i}$	$0, i = 0; \frac{1}{2}, i = 1..4$	$0, i = 0; \frac{1}{3}, i = 1..4; \frac{1}{12}, i = 5..8$
$\alpha_{Mi}$	-	$0, i = 0; 1, i = 1..4; \frac{1}{8}, i = 5..8$

The expression for the operator  $\nabla_\alpha$ , is obtained by the same procedure.

$$\nabla_\alpha \phi = \sum_i \alpha_{\nabla i} a_{i\alpha} \phi_i, \quad (\text{D.6})$$

There is a nine-point difference scheme for the operator  $\nabla_\alpha \nabla_\beta$ . The coefficients were taken in order to reduce numerical anisotropy:

$$\nabla_\alpha \nabla_\beta \phi = \begin{cases} \sum_i \alpha_{Mi} a_{i\alpha} a_{i\beta} \phi_i - \frac{5}{2} \phi - \frac{1}{4} \Delta \phi, & \alpha = \beta \\ 2 \sum_i \alpha_{Mi} a_{i\alpha} a_{i\beta} \phi_i, & \alpha \neq \beta \end{cases} \quad (\text{D.7})$$

The following operator takes place in the diffusion equation with an inhomogeneous diffusion coefficient.

$$\nabla(A\nabla B) = \sum_i \alpha_{\nabla i} (A_i + A)(B_i - B), \quad (\text{D.8})$$

where  $\alpha_{\Delta i}$  and  $\alpha_{\nabla i}$  are weight coefficients, see Table D.1.

### D.2.2 The 3D case

The expressions of the differential operators for the 3D case are listed here.

Discretisation of the Laplace operator, gradient and  $\nabla(A\nabla B)$  are the same as in the 2D case, with the only difference being in the coefficients, which are listed in Table D.2.

**Table D.2:** Weight coefficients for different templates, the 3D case

	7-point	19-point
$\alpha_{\Delta i}$	$-4, i = 0; 1, i = 1..6$	$-4, i = 0; \frac{1}{3}, i = 1..6; \frac{1}{6}, i = 7..18$
$\alpha_{\nabla i}$	$0, i = 0; \frac{1}{2}, i = 1..6$	$0, i = 0; \frac{1}{6}, i = 1..6; \frac{1}{12}, i = 7..18$
$\alpha_{Mi}$	-	$0, i = 0; \frac{2}{3}, i = 1..6; \frac{1}{6}, i = 7..18$

# Bibliography

- [1] ABROSIMOV, N., LÜDGE, A., RIEMANN, H., KURLOV, V., BORISSOVA, D., KLEMM, V., HALLOIN, H., VON BALLMOOS, P., BASTIE, P., HAMELIN, B., AND SMITHER, R. Growth and properties of  $\text{Ge}_{1-x}\text{Si}_x$  mosaic single crystals for gamma ray lens application. *J. Crystal Growth* 275, 1-2 (2005), e495–e500.
- [2] ABROSIMOV, N., ROSSOLENKO, S., THIEME, W., GERHARDT, A., AND SCHRÖDER, W. Czochralski growth of Si- and Ge-rich single crystals. *J. Crystal Growth* 174 (1997), 182–186.
- [3] BECKER, D., STERLING, T., SAVARESE, D., DORBAND, J., RANAWAKE, U., AND PACKER, C. Beowulf: A parallel workstation for scientific computation. In *Proceedings of ICPP* (1995).
- [4] BENZI, R., SUCCI, S., AND VERGASSOLA, M. The lattice Boltzmann equation: theory and applications. *Phys. Reports* 222, 3 (1992), 145–197.
- [5] BILLIA, B., AND TRIVERDI, R. Pattern formation in crystal growth. In *Handbook of crystal growth*, D. Hurlé, Ed., vol. 1b Transport and stability. Elsevier, 1993, pp. 899–1073.

- [6] BISANG, U., AND BILGRAM, J. H. Shape of the tip and the formation of sidebranches of xenon dendrites. *Phys. Rev. E* 54 (1996), 5309–5326.
- [7] BOETTINGER, W. J., AND WARREN, J. A. Simulation of the cell to plane front transition during directional solidification at high velocity. *J. Crystal Growth* 200 (1999), 583–591.
- [8] BOUZIDI, M., D'HUMIÈRES, D., LALLEMAND, P., AND LUO, L.-S. Lattice Boltzmann equation on a two-dimensional rectangular grid. *J. Comput. Phys.* 172, 2 (2001), 704–717.
- [9] BRENER, E., MÜLLER-KRUMBHAAR, H., TEMKINS, D., AND ABEL, T. Morphology diagram of possible structures in diffusional growth. *Physica A* 249, 1-4 (1998), 73–81.
- [10] CAGINALP, G. In *Applications of field theory to statistical mechanics*, L. Garrido, Ed., vol. 216 of *Lecture notes in physics*. Springer-Verlag, Berlin, 1985, pp. 216–226.
- [11] CAGINALP, G., AND FIFE, P. Phase-field method for interfacial boundaries. *Phys. Rev. B* 33, 11 (1986), 7792–7794.
- [12] CONTI, M. Interface dynamics, instabilities, and solute bands in rapid directional solidification. *Phys. Rev. E* 58, 2 (1998), 2071–2078.
- [13] CONTI, M. Phase and fields across the solid-liquid interface of a binary alloys. *Phys. Rev. E* 60, 2 (1999), 1913–1920.
- [14] CONTI, M., AND MARCONI, U. M. B. Groove instability in cellular solidification. *Phys. Rev. E* 63, 1 (2001), 011502.

- [15] DISMUKES, J. P., AND YIM, W. M. A survey of interface stability criteria in the elemental alloy systems: Ge-Si, Bi-Sb and Se-Te. *J. Crystal Growth* 22, 4 (1974), 287–294.
- [16] FLEKKØY, E. Lattice Bhatnagar-Gross-Krook models for miscible fluids. *Phys. Rev. E* 47, 6 (1993), 4247–4257.
- [17] FOLCH, R., AND PLAPP, M. Towards a quantitative phase-field model of two-phase solidification. *Phys. Rev. E* 68, 1 (2003), 010602.
- [18] FORUM, M. Mpi: A message-passing interface standard. *Int. J. Supercomput. Appl.* 8, 3/4 (1994).
- [19] GEORGE, W. L., AND WARREN, J. A. A parallel 3D dendritic growth simulator using the phasefield method. *J. Comput. Phys.* 177, 2 (2002), 264–283.
- [20] GRÁNÁSY, L., PUSZTAI, T., AND WARREN, J. A. Modelling polycrystalline solidification using phase field theory. *J. Phys.: Condens. Matter* 16 (2004), R1205–R1235.
- [21] HIGUERA, F., SUCCI, S., AND BENZI, R. Lattice gas-dynamics with enhanced collisions. *Europhysics Letters* 9, 4 (1989), 345–349.
- [22] HOHENBERG, P., AND HALPERIN, B. Theory of dynamic critical phenomena. *Rev. Mod. Phys.* 49, 3 (1977), 435–478.
- [23] HURLE, D., AND COCKAYNE, B. Czochralski Growth. In *Handbook of crystal growth 2: Bulk Crystal Growth*, D. Hurle, Ed. Elsevier, Amsterdam, 1994, pp. 99–211.

- [24] JERSCHOW, A., AND MÜLLER, N. Suppression of convection artifacts in stimulated-echo diffusion experiments. Double-stimulated-echoexperiments. *J. Magn. Reson.* 125 (1997), 372–375.
- [25] KARMA, A. Phase-field model of eutectic growth. *Phys. Rev. E* 49 (1994), 2245–2250.
- [26] KARMA, A., AND RAPPEL, W.-J. Quantitative phase-field modeling of dendritic growth in two and three dimensions. *Phys. Rev. E* 57, 4 (1998), 4323–4349.
- [27] KESSLER, D. A., KOPLIK, J., AND LEVINE, H. Geometrical models of interface evolution. ii. numerical simulation. *Phys. Rev. A* 30 (1984), 3161–3174.
- [28] KESSLER, D. A., AND LEVINE, H. Velocity selection in dendritic growth. *Phys. Rev. B* 33 (1986), 7687–7870.
- [29] KIM, S. G., KIM, W. T., AND SUZUKI, T. Interfacial compositions of solid and liquid in a phase-field model with finite interface thickness for isothermal solidification in binary alloys. *Phys. Rev. E* 58, 3 (1999), 3316–3323.
- [30] KIM, S. G., KIM, W. T., AND SUZUKI, T. Phase-field model for binary alloys. *Phys. Rev. E* 60, 6 (1999), 7186–7197.
- [31] KIM, Y.-T., PROVATAS, N., GOLDENFELD, N., AND DANTZIG, J. Universal dynamics of phase-field models for dendritic growth. *Phys. Rev. E* 59, 3 (1999), 2546–2549.
- [32] KOBAYASHI, H., ODE, M., KIM, S. G., KIM, W. T., AND SIZIKI, T. Phase-field model for solidification of ternary alloys coupled

- with thermodynamic database. *Scripta Mater.* 48, 6 (2003), 689–694.
- [33] KURZ, W., AND FISHER, D. *Fundamentals of solidification*, 4 ed. Trans Tech Publications LTD, 1998.
- [34] LAN, C. W., AND CHANG, Y. C. Efficient adaptive phase field simulation of directional solidification of a binary alloy. *J. Crystal Growth* 250 (2003), 525–537.
- [35] LAN, C. W., HSU, C. M., LIU, C. C., AND CHANG, Y. C. Adaptive phase field simulation of dendritic growth in a forced flow at various supercoolings. *Phys. Rev. E* 65 (2002), 061601.
- [36] LANGER, J. S. Instabilities and pattern formation in crystal growth. *Rev. Mod. Phys.* 52, 1 (1980), 1–28.
- [37] LOGINOVA, I., AMBERG, G., AND ÅGREN, J. Phase-field simulation of non-isothermal binary alloys solidification. *Acta Materialia* 49, 4 (2001), 573–581.
- [38] MCFADDEN, G., WHEELER, A., BRAUN, R., CORIELL, S., AND SEKERKA, R. F. Phase-field models for anisotropic interfaces. *Phys. Rev. E* 48, 3 (1993), 2016–2024.
- [39] NAKAMURA, S., EGUCHI, M., AZAMI, T., AND HIBIYA, T. Thermal waves of a nonaxisymmetric flow in a Czochralski-type silicon melt. *J. Crystal Growth* 207, 1-2 (1999), 55–61.
- [40] NASH, G. E., AND GLICKSMAN, M. E. Capillarity-limited steady-state dendritic growth. 1. Theoretical development. *Acta Metall. et Mater.* 22, 10 (1974), 1283–1290.

- [41] NESTLER, B., AND WHEELER, A. A. A multi-phase-field model of eutectic and peritectic alloys: numerical simulation of growth structures. *Physica D* 138, 1-2 (2000), 114–133.
- [42] NESTLER, B., WHEELER, A. A., AND GARCKE, H. Modelling of microstructure formation and interface dynamics. *Comp. Mater. Sci.* 26 (2003), 111–119.
- [43] OKAMOTO, H. *Phase Diagrams for Binary Alloys*. ASM International, 2000.
- [44] PENROSE, O., AND FIFE, P. C. Thermodynamically-consistent models of phase-field type for the kinetics of phase transitions. *Physica D* 43, 1 (1990), 44–62.
- [45] PROVATAS, N., GOLDENFELD, N., AND DANTZIG, J. Adaptive mesh refinement computation of solidification microstructures using dynamic data structures. *J. Comput. Phys.* 148, 1 (1999), 265–290.
- [46] PROVATAS, N., GOLDENFELD, N., AND DANTZIG, J. Crossover Scaling in Dendritic Evolution at Low Undercooling. *Phys. Rev. Lett.* 82, 22-31 (1999), 4496–4499.
- [47] RASIN, I., MILLER, W., AND SUCCI, S. Phase-field lattice kinetic scheme for the numerical simulation of dendritic growth. *Physical Review E* 72, 6 (2005), 066705.
- [48] RASIN, I., SUCCI, S., AND MILLER, W. A multi-relaxation lattice kinetic method for passive scalar diffusion. *Journal of Computational Physics* 206, 2 (2005), 453–462.



- [49] ROMANENKO, V., AND SMIRNOV, U. Koefficienti raspredeleniya i koefficienti diffuzii komponentov v rasplave sistemi germaniy-kremniy. *Neorganicheskie materialy(RUS)* 10, VI (1970), 1733–1739.
- [50] ROOSEN, A. R., AND TAYLOR, J. E. Modeling crystal growth in a diffusion field using fully faceted interfaces. *J. Comput. Phys.* 114, 1 (1994), 113–128.
- [51] SCHNEIDER, J. R.  $\gamma$ -ray diffractometry. In *Nuclear Science Applications*, vol. 1. New York: Harwood Academic Publishers, 1981, pp. 227–276.
- [52] SEKERKA, R. F. Fundamentals of phase field theory. In *Advance in crystal growth research*, K. Sato, Y. Furukawa, and N. Nakajima, Eds. Elsevier, Amsterdam, 2001, pp. 21–41.
- [53] SEKERKA, R. F. Morphology: from sharp interface to phase field models. *J. Crystal Growth* 264, 4 (2004), 530–540.
- [54] SEKERKA, R. F. Theory of crystal growth morphology. In *Proceedings ISSCG-12* (2004).
- [55] SHAN, X., AND DOOLEN, G. Diffusion in a multicomponent lattice Boltzmann equation model. *Phys. Rev. E* 54 (1996), 3614–3620.
- [56] SMIRNOVA, O., KALAEV, V., MAKAROV, Y., ABROSIMOV, N., AND RIEMANN, H. Modeling of Si transport in the melt during CZ  $\text{Ge}_{1-x}\text{Si}_x$  growth. *J. Crystal Growth* (to be published).
- [57] STERLING, J. D., AND CHEN, S. Stability Analysis of Lattice Boltzmann Methods. *J. Comput. Phys.* 123 (1996), 196–206.

- [58] STOCKMAN, H. W., GLASS, R. J., COOPER, C., AND RAJARAM, H. Accuracy and computational efficiency in 3D dispersion via lattice-Boltzmann: Models for dispersion in rough fractures and double-diffusive fingering. *Int. J. Mod. Phys. C* 9, 8 (1998), 1545–1557.
- [59] SUCCI, S. *The Lattice Boltzmann Equation for Fluid Dynamics and Beyond*. Oxford, Clarendon Press, 2001.
- [60] SUCCI, S., CHEN, H., TEIXEIRA, C., BELLA, G., MARIO, A., AND MOLVIG, K. An integer lattice realization of a Lax scheme for transport processes in multiple component fluid flows. *J. Comput. Phys.* 152 (1999), 493–516.
- [61] TILLER, W. *The Science of Crystallization: Macroscopic Phenomena and Defect Generation*. Cambridge University Press, 1992.
- [62] TONG, X., BECKERMANN, C., KARMA, A., AND Q.LI. Phase-field simulation of dendritic crystal growth in a forced flow. *Phys. Rev. E* 63 (2001), 061601–1.
- [63] UEARA, T., AND SEKERKA, R. F. Phase field simulations of faceted growth for strong anisotropy of kinetic coefficient. *J. Crystal Growth* 254 (2003), 251–261.
- [64] VAN DER SMAN, R. G. M., AND ERNST, M. H. Diffusion lattice Boltzmann scheme on an orthorhombic lattice. *J. Stat. Phys.* 94, 1/2 (1999), 203 – 217.
- [65] VON BALLMOOS, P., HALLOIN, H., SKINNER, G., SMITHER, R., PAUL, J., ABROSIMOV, N., ALVAREZ, J., ASTIER, P., BASTIE, P., BARRET, D., BAZZANO, A., BOUTONNET, A.,

- BROUSSE, P., CORDIER, B., T.COURVOISIER, DICOCO, G., GIULIANI, A., HAMELIN, B., HERNANZ, M., JEAN, P., ISERN, J., KNÖDLSIEDER, J., LAURENT, P., LEBRUN, F., MARCOWITH, A., MARTINOT, V., NATALUCCI, L., OLIVE, J., R.PAIN, SADAT, R., SAINT, H., UBERTINI, P., AND VEDRENNE, G. MAX - a gamma-ray lens for nuclear astrophysics. *SPIE proc. (Intl. Soc. for Optical Engeneering) 5168* (2004).
- [66] WANG, S.-L., SEKERKA, R., WHEELER, A., MURRAY, B., CORIELL, S., BRAUN, R., AND MCFADDEN, G. Thermodynamically-consistent phase-field models for solidification. *Physica D* 69, 2 (1993), 189–200.
- [67] WARREN, J. A., AND BOETTINGER, W. J. Prediction of dendritic growth and microsegregation patterns in a binary alloy using the phase-field method. *Acta Metall. et Mater.* 43, 2 (1995), 689–703.
- [68] WEINSTEIN, O., AND BRANDON, S. Dynamics of partially faceted melt/crystal interfaces I: computational approach and single step-source calculations. *J. Crystal Growth* 268, 1-2 (2004), 299–319.
- [69] WHEELER, A., BOETTINGER, W., AND MCFADDEN, G. Phase-field model for isothermal phase transition in binary alloys. *Phys. Rev. A* 45, 10 (1992), 7424–7439.
- [70] WILKE, K. T., AND BOHM, J. *Kristallzüchtung*, 2 ed. Verlag Harri Deutsch, 1988.
- [71] WOLF-GLADROW, D. *Lattice-Gas Cellular Automata and Lattice Boltzmann Models*. Springer, 2000.

- [72] YOKOYAMA, E., AND KURODA, T. Pattern formation in growth of snow crystals occurring in the surface kinetic process and the diffusion process. *Phys. Rev. A* 41 (1990), 2038–2049.
- [73] YU, D., MEI, R., LUO, L.-S., AND SHYY, W. Viscous flow computations with the method of lattice Boltzmann equation. *Progress in Aerospace Sciences* 39, 5 (2003), 329–367.
- [74] YU, Q., THOMPSON, M. O., AND CLANCY, P. Solidification kinetics in SiGe alloys. *Phys. Rev. B* 53, 13 (1996), 8386–8397.